University College London

Doctoral Thesis

Motheye Smart Windows

Bio-inspired, temperature-responsive glazing for passive regulation of building temperature with the ability to self-clean.

Author:
Alaric Taylor

Advisors:
Dr. Ioannis Papakonstantinou
&
Prof. Ivan P. Parkin

2017

Work is not finished;
it is abandoned at the right time.

I, Alaric Taylor, confirm that the work presented in this thesis is my own. I confirm that it has been clearly indicated where information has been derived from other sources.

Alaric Taylor.

Acknowledgements

First and foremost, love and thanks to Amelia. She listened to me talk about windows for too many years and made coming home at the end of the harder days worth it.

To my Mum and Dad, and the families Taylor and Tuhill-Roffey: love to you all.

To my close friends. I hope you all know how much I have valued your friendship and continue to do so.

To Clemens Tummeltshammer and Mark Brown, who were with me all along the way and helped to inspire a new generation. Also, to the legends of the laboratory: Steve Hudziak, Wing Ng, Nuno Braz, Tom Gregory, Vijay Krishan, Nuruzzaman Noor, Sarwat Baig, Michael Powell, Barry Reid, Rachel Wilson, Carlos Sotelo-Vazquez, Delphine Malarde, Mark Buckwell and many more. I learnt so much from you all and enjoyed doing so.

To my mentors and those who gave me invaluable guidance, in particular: Ivan Parkin, Tony Kenyon, Raul Quesada Cabrera, Stefan Guldin, Chris Blackman, Robert Thompson and James Allsopp. I asked for a lot but you all remained consistently generous and regularly went over-and-above in your support.

To the wonderful folk who make everything happen and put up with a lot of nonsense: Lee Heagney, Scott Landers, Tim Bodley-Scott and Seb Carrington.

To the students I mentored and that taught me: Leon Garnett, Chee Bin Ler and Xinke Tang. I hope to see you all in the future and would be lucky if I could work with more young researchers like yourselves.

Finally, there are many people who deserve my sincere thanks for their support over the recent years. Of whom, I have undoubtedly forgotten to thank many by name. Therefore, I would like to take this opportunity to say how grateful I am for the things they have done (and continue to do) that add-up.

I would like to thank the Photonic Systems Development Centre for Doctoral Training for its award of a research scholarship. We would also like to thank the UK Engineering and Physical Sciences Research Council (EPSRC) for awarding a grant towards the fabrication of prototype VO_2 moth-eye smart-windows which funded many of our efforts (EP/K015354/1).

Chapter 5 on page 67 includes results derived from Chee Bin Ler's undergraduate BEng project which was supervised by myself and Ioannis Papakonstantinou. Specifically, fig. 5.3 on page 71 and fig. 5.4 on page 72 are reproductions from this work. Section 8.2 on page 104 was supported by the work of Leon Garnett during his MSc project supervised by myself. Figure 8.11 on page 107 is an AFM scan taken by himself during this time.

Notation & abbreviations

SW	Smart window
Low-e	Low-emissivity
λ	Wavelength
TE	Transverse-electric polarisation (s-polarised)
TM	Transverse-magnetic polarisation (p-polarised)
UV	Ultraviolet, $\lambda < 450\,\text{nm}$
Vis	Visible, $450 < \lambda < 650\,\text{nm}$
NIR	Near-infrared, $0.65 < \lambda < 3\,\mu\text{m}$ (solar-thermal)
MIR	Mid-infrared, $3 < \lambda < 50\,\mu\text{m}$ (domestic-temperature black body sources)

MIT	Metal-to-insulator phase transition
τ	Temperature in degrees Celsius ($^\circ$C)
τ_c	Critical temperature for metal-to-insulator phase transition
σ	Temperature dependant phase of a thermochromic material i.e. either *hot* (when $\tau \gg \tau_c$) or *cold* (when $\tau \ll \tau_c$)

T_{vis}	Photopically averaged visible transmittance
A_{vis}	Photopically averaged visible absorptance
R_{vis}	Photopically averaged visible reflectance
T_{sol}	Solar averaged solar transmittance
A_{sol}	Solar averaged solar absorptance
R_{sol}	Solar averaged solar reflectance
ΔT_{vis}	Visible transmittance modulation
ΔT_{sol}	Solar transmittance modulation

Λ	Periodicity/pitch of a regular nanostructure
h	Tip-to-base height of a nanostructure
ϕ	Nanocone base-width / nanosphere diameter

γ	Surface energy
θ_{CA}	Static three-phase contact angle
$\theta_{\mathrm{CA\text{-}A}}$	Advancing contact angle
$\theta_{\mathrm{CA\text{-}R}}$	Receeding contact angle
θ_{CAH}	Contact angle hysteresis

PMMA	Poly(methyl 2-methylpropenoate) / poly(methyl methacrylate)
PS	Poly(1-phenylethene) / polystyrene
ZEP	Positive tone Electron–Beam resist manufactured by ZEON Corporation
MIBK	Methyl isobutyl ketone
IPA	Isopropyl alcohol
HSQ	Hydrogen silsesquioxane

AACVD	Aerosol Assisted Chemical Vapour Deposition
EACVD	Electric Field Assisted Chemical Vapour Deposition
APCVD	Atmospheric Pressure Chemical Vapour Deposition
RFMS	Radio Frequency Magnetron Sputtering
DCMS	Direct Current Magnetron Sputtering
ALD	Atomic Layer Deposition
PLD	Pulsed Laser Deposition

PL	Photolightography
EBL	Electron Beam Lithography
LB	Langmuir-Blodgett
LS	Langmuir-Schaefer
CNL	Colloidal Nanosphere Lithography
BCP	Block Copolymer
RIE	Reactive Ion Etching

FDTD	Finite Difference Time Domain
PML	Perfectly Matched Layer
ME	Motheye
GRIN	Graded Refractive Index Nanostructure
AFM	Atomic Force Microscope/Microscopy
SEM	Scanning Electron Microscope/Microscopy
VASE	Variable Angle Spectroscopic Ellipsometry
XRD	X-ray diffraction (crystallography)

Contents

List of Figures

Part I

Preface

Preface

0.1 Abstract

The work presented in thesis is dedicated primarily to improving the optical properties of vanadium dioxide (a thermochromic material used for energy-saving window applications) through the incorporation of bio-mimetic sub-wavelength nanostructures at the air–glass interface. The focal points of our work have been: firstly, to identify where in the world these types of smart windows are most effective; secondly, to synthesise vanadium dioxide and characterise its optical properties; thirdly, to develop design rules for nanostructured Motheye Smart Windows; fourthly and finally, to fabricate the desired motheye nanostructures in glass.

0.2 Motivations

The need to reduce global energy consumption is urgent; there is no question that CO_2 emissions released by the combustion of fossil fuels is unsustainable and contributes toward global warming [1–3]. The International Energy Agency predicts that without decisive action CO_2 emissions will reach 15.2 gigatonnes per year in 2050 [4], double the emissions from 2007. A driving force for increased energy consumption has been continued growth of the world's population which is predicted to reach almost 10 billion by 2050 [5]; the number of households is expected to rise by 67% and commercial building spaces to double in volume [4]. Of key concern is the increased year-upon-year growth of *per capita* energy consumption [6] which serves only to exacerbate the energy crisis and climate change effects. Therefore, we must improve the efficiency of energy consumption in the human environment in order to help counteract climate change effects.

Contemporary analysis of energy usage shows that heating, cooling, ventilation and the powering of appliances within buildings accounts for approximately 30 to 40% of primary energy consumption worldwide [7, 4, 8]. As an example, in 2010 the world's second largest energy consumer, the United States, spent 41.1% of its primary energy on the building sector (accounting for 40% of energy-related carbon dioxide emissions) [9]. This accounted for 7% of global energy use that year, of which approximately 60% was employed to either heat, cool, light, or ventilate the indoor environment [8].

Looking to the future, predictions by the International Energy Agency indicate that the share of energy spent on heating and cooling buildings will only increase [10, p. 46]. Without preventative action, the built environment will consume 60% more energy in 2050 than today [4, p. 8]. Unsurprisingly, technology roadmaps designed to counteract increased energy demand place key emphasis upon building improvements [3, 2, 1]. Emissions could

be reduced by 2 gigatonnes of CO_2 per year by simply adapting domestic and industrial buildings to be more energy-efficient; saving 710 million tones oil equivalent [4, p. 7]. As an additional incentive, reducing heating and cooling energy expenditure has been highlighted as a key component in future energy security on numerous occasions [11, 3, 2, 1]. The economics of 'green buildings' are encouraging: they attract both higher rental and sales prices compared with equivalent non-green developments [12].

Justification for the large portion of energy spent upon moderating indoor climates is provided by the large share of time spent in buildings; in the developed world 90% of people's time is spent either indoors or within a vehicle [13, 14]. Furthermore, it provides motivation to improve the ambience and aesthetic experience. However, poor management of the built environment, such as the extensive use of air-conditioning systems in dense cities, is self-defeating as it can give rise to urban heat islands in which local air temperatures soar as energy is spent on moving hot air out of buildings which it inevitably re-enters [15].

In summary, pressure to improve building efficiency has increased as the environmental impacts of excessive energy consumption have become unacceptable and the economic incentives to improve efficiency become increasingly attractive. Precise control over the flux of energy in and out of the building is critical. Windows, as the principal interface between the interior and exterior environments, constitute the most vulnerable aspect of a building's energy efficiency [16].

0.3 Aim

Our research objective has been to develop a new class of vanadium dioxide-based 'intelligent', temperature-sensitive glazing that dynamically alters its transmittance with the effect of stabilising internal building temperatures. A dynamic window system would reduce the energy requirements for cooling and heating buildings by tempering, and in some environments obviating, the use of air-conditioning and central heating systems. In addition, the glazing developed within this project inherits enhanced self-cleaning properties which bring about additional economic benefits through a substantial reduction in maintenance costs. Such economic benefits are not to be underestimated as the cost of window cleaning in modern architecture can, in some cases, exceed the installation costs within the first two years.

Vanadium dioxide-based temperature-sensitive ('thermochromic') smart-windows modulate the transmission of infrared solar radiation into a building. This part of the electromagnetic spectrum is not required for vision (see Figure fig. 1 on the following page). The windows maintain their transmissive visibility at all times, thus allowing direct implementation within established architectural practice. In order to limit a greenhouse heating effect during hot weather, the window allows only the visible portion of the electromagnetic spectrum to pass into a building. However, during cool weather the entire solar spectrum is transmitted into the building in order to exploit solar heat gain. The switching process is entirely passive and intrinsic to the metal-oxide (vanadium dioxide, VO_2), the functional component within this type of smart window system. Thus, the use of these smart-windows manifest as both the heating and cooling elements without any requirement for sensing, control circuitry or compensatory electric lighting.

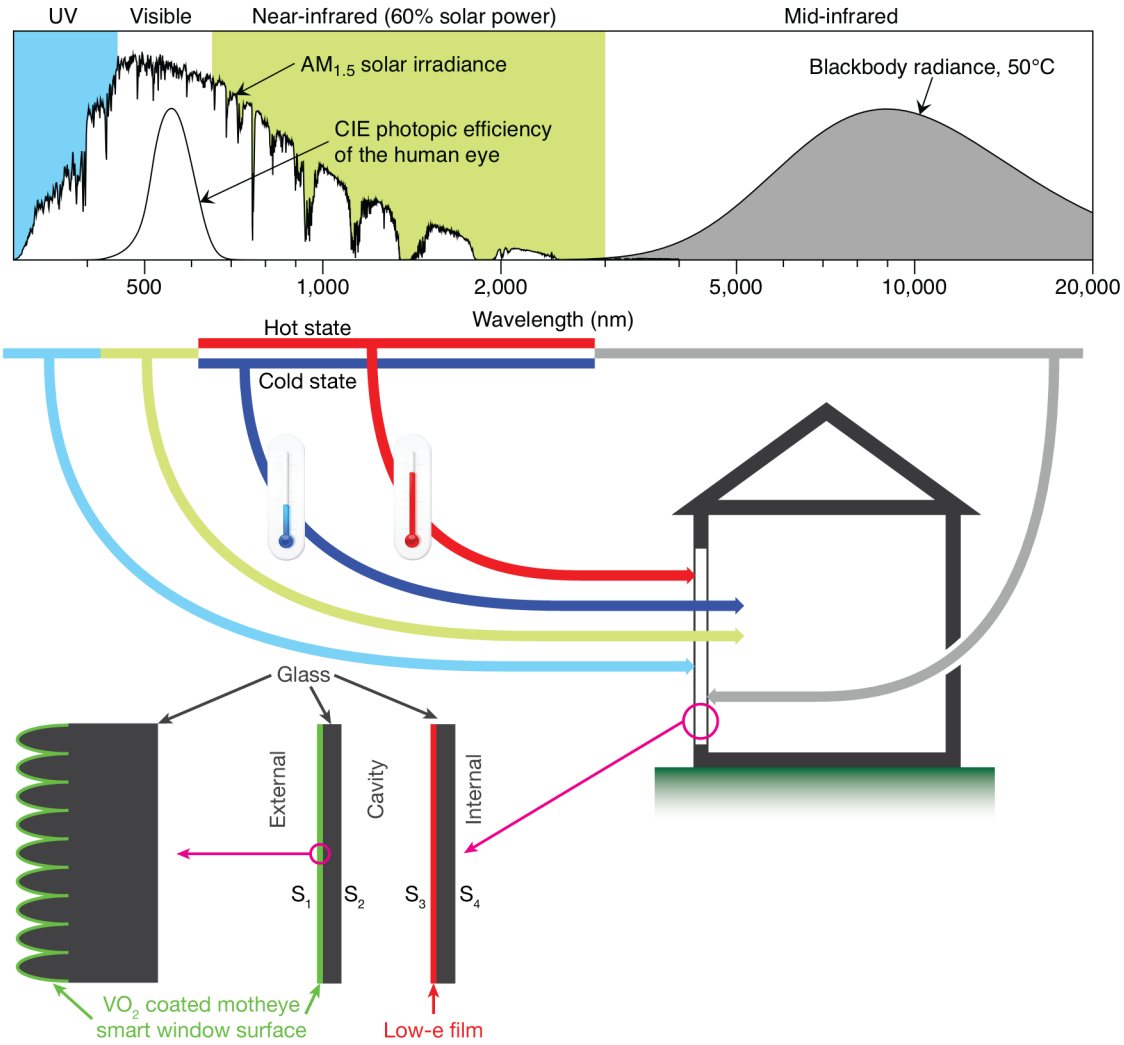

Figure 1: A smart window acting as a 'dynamic energy gate'. Near-infrared radiation (hatched in blue and red) is transmitted into the building during the 'cold' state (leading to a greenhouse heating effect) whilst being blocked in the 'hot' state (thereby preventing solar heating). Visible light is transmitted in both the 'hot' and 'cold' states but the use of a low-emissivity (low-e, seesection 4.6 on page 64) film prevents mid-infrared thermal radiation escaping during the cold state or being radiatively transmitted into the building during its hot state. UV light is blocked by several millimetres of float-glass.

Our motheye system's switching-mechanism is absorptance. In its cold state, absorptance is low; however, this increases as the window enters its hot state where high absorptance limits the transmission of thermal energy into a building. This is in contrast to conventional planar VO_2 smart-window systems where reflectance increases as the window enters its hot state. When implemented within a high density urban environment, reflection of unwanted infrared radiation will induce heat valleys, a contemporary issue facing mass-air-conditioning. Absorption within the motheye smart-window provides the potential to responsibly manage solar-energy on a system level; a feature not offered by reflective systems. Through this absorption process, it may be possible to avoid architectural mis-design in which reflection solar energy causes damage to nearby property [17].

0.3.1 Implementation

The work presented within this thesis is centred around the production of VO_2 motheye smart window surfaces *in glass*. However, the same principle could be employed to create a highly efficient thermochromic plastic film. In brief, we envisage two alternative implementations of VO_2-based motheye smart-windows systems.

Glass pane The motheye nanostructures would be patterned directly within the glass window surface. A conformal coating of vanadium dioxide is applied to the nanostructured glass using conventional metal-oxide deposition techniques. This is a potentially high-cost and high-performance embodiment of this class of smart-window and is intended for premium products at a factory production level. We foresee the large-area production of motheye surface nanofeatures as the primary challenge for this implementation.

Plastic film A flexible plastic film is imprinted with motheye surface features and subsequently either coated with a vanadium dioxide layer or embedded with vanadium dioxide nanoparticles. This is a low-cost alternative to the glass implementation with potential for good performance. It offers the opportunity to either cheaply manufacture new windows with this surface coating or retrofit existing window installations. The market for this mode of implementation is large and potentially lucrative. Roll-to-roll production of motheye plastic films has already been demonstrated [18]. In the case of an over-coated film, we foresee the primary challenge to this implementation as the deposition of monoclinic vanadium dioxide at a plastic-compatible temperature (Plasma Enhanced Atomic Layer Deposition may be the most promising approach). In the case of nanoparticle-embedded motheye films, we would expect the avoidance of scattering/haze to be the primary challenge.

0.3.2 Integrated unit

The envisaged implementation of a Motheye Smart Window is shown in fig. 1 on page 18. The nanostructured motheye interface would be cited on the external surface (S_1) of a gas-insulated window unit allowing its superhydrophobic self-cleaning properties to take affect. Conductive heat transfer into and out of the building would be impeded by the use of a gas-filled cavity between the glass panes, discussed further in section 2.2.1 on page 45.

The system would employ a low-emittance film, cited within the cavity (S_3 perhaps), in order prevent radiative heat transfer due to absorption of solar energy at the motheye interface. Low-emittance films are capable of transmitting most of the solar spectrum (up to approximately $\lambda = 3\,\mu$m) and therefore their use would not impede the cold state greenhouse heating effect. In fact, the synergy of a low-e film combined with a motheye thermochromic film in the way we have described above would benefit the smart window system by efficiently tapping heat inside the building during cold weather and blocking its passage from the external environment during hot weather. A full discussion of the use of low-emittance window coatings is provided in section 2.2.2 on page 45 and section 4.6 on page 64.

0.4 Novelty

Our approach towards engineering high-performing thermochromic smart-windows has been to employ sub-wavelength, bio-mimetic 'motheye' conical nanostructures on the glass surface. These conical nanostructures, based upon those found on the eyeballs of moths, greatly improve the optical properties of the window surface as they exhibit highly efficient broadband, polarisation-insensitive and wide-angle anti-reflection properties. Incorporation of these nanostructures into the window's surface has the effect of both enhancing visible transmission and improving solar-thermal transmission-modulation (directly related to the window's energy-saving potential).

The motheye strategy is a unique approach toward improving vanadium dioxide based smart-windows. Our initial publication was the first to predict that a thin, thermochromic film overcoating a natural anti-reflection nanostructure could produce a high-performing smart-window [19]. Since then we have shown that the bio-inspired 'motheye' class of smart-window can quadruple the solar-energy transmission-modulation and double the visible transmission.

Included within this thesis; our map-based investigations into the suitable climates for citing temperature sensitive smart windows (chapter 5 on page 67) are, to the best of our knowledge, the only of their kind. Our comprehensive characterisation of vanadium dioxide films produced via Atmospheric Pressure Chemical Vapour Deposition provide previously unavailable spatial maps of phase, thickness, topology and optical properties that result from the kinetics of the surface reaction that formed the material, see chapter 6 on page 74. We demonstrate a novel method for selecting the highest-performing smart-window interfaces, see section 4.2.1 on page 59. It facilitates both *intra*- and *inter*-class comparisons and can be extended to visualise the affect of critical system-parameters when applied to intra-class comparisons, see fig. 7.8 on page 90. This provides a powerful way in which to establish design rules for any such multi-parameter system. Finally, we have developed and report upon two methods of fabricating motheye nanostructures using both top-down and bottom-up techniques. Our nanosphere self-assembly processes for fabricating motheyes at a glass interface is cheap and can form nanostructures over a large area in a controlled manner.

0.5 An overview of this document

This thesis has been divided into a series of short chapters in order to facilitate a clear flow of narrative. It begins with a preface in which, following our abstract, the environmental and economic motivations for smart windows are discussed section 0.2 on page 16. Our approach toward combating the excessive energy consumption of buildings through the use of dynamic glazing is introduced in section 0.3 on page 17 and expanded upon in section 0.3.1 on page 19. Some key aspects of the novelty in our work are highlighted in section 0.4 on page 20.

Our review of motheye interfaces is found in chapter 1 on page 25. In this chapter we discuss the biological origin of these interfaces and technologies which seek to mimic them before moving on to their optical theory in section 1.2 on page 26. In this section we discuss the directional-dependence of the quasi-static condition and its relation to diffraction gratings; effective medium approximations of nanostructured interfaces and the mode by which reflection is suppressed over a broad range of wavelengths; and finally, some variations of motheye nanostructures. We then move on to discuss the wetting characteristics of flat and nanostructured materials in section 1.3 on page 33. The conditions under which a super-hydrophobic wetting breaks down and the surface can no longer perform self-cleaning are the subjects of sections 1.3.2 to 1.3.3 on pages 35–36. We round-up our review of motheye interfaces by discussing the many and varied methods by which they can be fabricated in section 1.4 on page 38. Our discussions include, both subtractive and additive methods and also maskless and lithographic methods before moving on to discuss top-down and bottom-up masking techniques in section 1.4.2 on page 41.

Chapter 2 on page 44 provides a broad overview of window and glass technology and how they have evolved. A historical context for modern insulated-glass-units ('multiple glazing') and low-e windows is given in section 2.1 on page 44. The next generation of window technology, the dynamic 'smart-window', is introduced in section 2.3 on page 46. This is followed by a discussion of two modes of comparison between competing classes of smart window (active/passive and consistently-transparent or not).

Chapter 3 on page 48 is dedicated to the material properties of vanadium dioxide (VO_2). We begin by discussing thermochromism and how VO_2 attracted interest as a building material in sections 3.1 to 3.2 on pages 48–49. Our discussion then focuses upon the relationship between the crystal structure (which changes as a function of temperature) and the material's band-structure in section 3.3 on page 49. Following this, we explore a variety of different doping schema that either alter the transition temperature, reduce the transition-hysteresis or widen the fundamental band-gap of the material, see section 3.4 on page 51. We conduct a review of different VO_2 synthesis techniques in section 3.5 on page 52 before discussing the implications for ultra-thin films of vanadium dioxide in section 3.6 on page 53.

Chapter 4 on page 55 constitutes our final background chapter. In it, we define the tools that enable us to makes quantified comparisons between different smart-window systems, vital for the chapters to come. These include the two principal smart-window metrics: the spectrum-weighted visible transmittance, T_{vis} (section 4.1.1 on page 55); and the solar transmittance modulation, ΔT_{sol} (section 4.1.3 on page 57). We than move on to discussing how these two metrics and their graphical representation can be used to identify

the best performing systems in section 4.2.1 on page 59. Before examining the industrial measures used to characterise a window's energy characteristics (4.4) we dedicate a short section to identifying the ideal 'transmittance switching-edge' for spectrally-selective smart windows, see section 4.3 on page 61. The chapter is concluded by a discussion regarding the emissivity of vanadium dioxide-based motheye smart windows, see section 4.6 on page 64.

Chapter 5 on page 67 begins with a discussion of building-level energy-modelling for assessing the impact of thermochromic smart windows. From that point we move on to describe our investigations into map-oriented prospecting for thermochromic smart-windows based upon world-weather data, see section 5.2 on page 68. We show how this method can be integrated with additional data-sets (in this case population-statistics) to determine the global market potential for this technology, see section 5.3 on page 71.

Our synthesis of a vanadium dioxide thin film through Atmospheric Pressure Chemical Vapour Deposition and its full-scale characterisation is the subject of chapter 6 on page 74. Following our description of the synthesis process, we present two modes of spatial phase-mapping (XRD and Raman), see section 6.2 on page 75. Having established that our synthesised material had good phase-purity, we investigate the sample's topology using Atomic Force Microscopy in order to help construct an appropriate structural model for our ellipsometric investigations in section 6.4.2 on page 77. The dispersive model used to fit our ellipsometric measurements of the most phase-pure region of the sample is also discussed in this section. The following simulation-focused chapter employs the optical properties obtained herein as the basis of our dispersive material model for vanadium dioxide.

Chapter 7 on page 81 is devoted to calculating the performance boundaries for VO_2–based planar and motheye smart-window systems and whilst doing so identifying exactly which aspects of their design improve or degrade performance. Our two principal methods for performing simulations are discussed in section 7.1 on page 81 which is followed by a description of the dispersive models we used within them. The first set of calculations we present, in section 7.2 on page 83, are focused upon planar structures (air–VO_2–glass). We show that specific resonant thicknesses can be chosen in order to provide a perceived neutral transmittance colour and following this we define the primary performance boundary for VO_2–based smart-windows in fig. 7.2 on page 84. In the following sections (sections 7.3 to 7.4 on pages 84–86) we decouple the effects of bulk absorptance and Fresnel reflectance losses. Our motheye system and its associated parameters are introduced in section 7.5 on page 88 where we the detail how we went about searching for its set of optimum geometries and the performance boundary it defines. Results from our simulations undergo analysis which allows us to identify system design rules in sections 7.5.1 to 7.5.2 on pages 89–91. Finally, we look in detail at three different geometry sets which provide an insight into the operation of VO_2–coated motheye surfaces, see section 7.5.3 on page 94.

The final chapter of results (chapter 8 on page 97) details our efforts to fabricate motheye nanostructures in glass and can be divided into two halves. The first is devoted to our top–down approaches toward fabricating these nanostructures using Electron Beam Lithography. It begins by examining the different methods we used to mitigate charging effects in order to allow us to write on a non-conductive glass substrates, see section 8.1.1 on page 97. We then move on to discussing our method for efficiently writing arrays of dots

over large areas in section 8.1.2 on page 100. Finally, we discuss our lithographic process of inverting the PMMA resist into a Chrome hard-mask and Reactive Ion Etching in order to produce motheye nanostructures, see sections 8.1.3 to 8.1.4 on pages 101–102. In the second half of this chapter (section 8.2 on page 104) we move on to discuss our use of self-assembled masks, a bottom–up approach toward fabricating motheye nanostructures over large areas. We cover two of the methods we used to deposit monolayers of nanoparticles in sections 8.2.1 to 8.2.2 on page 105. Following this we discuss the two approaches we took toward using nanosphere monolayers to define an etch mask: firstly, through lithographic inversion into a Cr hard-mask; and secondly, use of the nanospheres as a soft-mask – see sections 8.2.3 to 8.2.5 on pages 106–110. To conclude this chapter, we present our optical characterisation and wetting functionalisation study of the fabricated motheye interfaces in section 8.2.6 on page 111 and section 8.2.7 on page 113, respectively.

Part II

Background

Chapter 1

Motheyes Smart Windows

1.1 Motheye nanostructures

Taking inspiration from nature and applying it to solve human problems is the essence of 'bio-mimetic' or 'bio-inspired' engineering. Many surfaces in nature have evolved in such a way as to optimise their micro- or nano-scale surface properties for a wide variety of functions [20]. Examples of these sophisticated natural structures include the Namib desert beetle (stenocara gracilipes), whose shell harvests water from the air [21]; the lotus leaf, which self-cleans [22, 23]; and the wings of butterflies, which exhibits pigment-free iridescent colours [24].

Since theinitial studies in the early 1960s, the sub-wavelength structures found on the cornea of nocturnal moths have been know to form highly efficient anti-reflection surfaces [25, 26]. The 'corneal nipples' on the surface of a moth's eyeball act as a broadband, polarisation-insensitive and omni-directional anti-reflection coating preventing the detection of the moth from would-be predators [27, 28]. Due to their hierarchical nature, 'motheye' surface structures not only act as an anti-reflection coating but can also promote super-hydrophobic self-cleaning on the surfaces they are patterned upon [29, 20]. These combined properties make 'motheye' nanoscale-textured glass surfaces attractive for smart-window design.

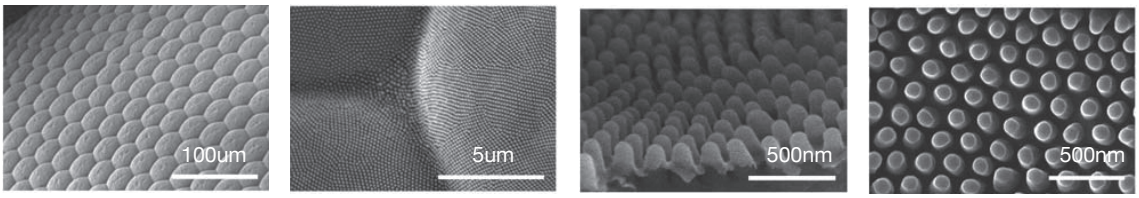

Figure 1.1: Subwavelength surface structures on the eyeballs of *attacus atlas* moths: 'motheye' nanostructures [30]. The nanostructures visible in (**c**) and (**d**) function as a broadband, omni-directional, polarisation-insensitive anti-reflection interface.

Motheye anti-reflection nanostructures have received interest for solar cell applications [31–36] and stealth technologies [37, 38]. The use of graded index nanostructures on the surface of optical glass has also been explored for a variety display applications in recent years [39]. In 2012 and 2013 Sharp launched a series of 'Ultra HD 4K' televisions that featured motheye surface coating technology for screens up to 90-inches. This is in direct competition with Philips who also released their '46PFL9706' television in 2012 that

employed motheye technology to improve the viewing experience.

In this chapter we will begin by discussing the optical properties of motheye nanostructures (section 1.2). We will then move on to discuss wettability of nanostructured surfaces (section 1.3 on page 33) before exploring methods by which they can be fabricated (section 1.4 on page 38).

1.2 Optical theory

1.2.1 The quasi-static condition and its omni-directionality

Tapered 'corneal nipples' are typically found spaced between 180 and 240 nm apart on the eyeballs of moths and some butterflies [40]. This average spacing is referred to as their 'periodicity' and denoted as Λ. Wavelengths of light, λ, within the visible range ($450 < \lambda < 650\,\text{nm}$) are unable to resolve these structures and instead interact with an 'effective-medium' [41, 27]. This is referred to as the 'quasi-static' condition and occurs when the grating equation (which defines which diffracted modes can propagate through a structured interface) is *only* satisfied by the zeroth-order, $m = 0$,

$$n_t \sin(\theta_{t,m}) + n_i \sin(\theta_i) = \frac{m\lambda}{\Lambda} \tag{1.1}$$

where Λ is the spacing between the nanocones, n_i is the refractive index of the incident material, n_t is the refractive index of the transmitting 'nipple' material, m is the diffraction order (i.e. 0, 1, 2 etc.), and θ_i and $\theta_{t,m}$ are the angle (relative to the surface-normal) for incident and diffracted light.

For a diffractive top-surface (as shown in subfigure (**a**) of fig. 1.2 on the following page), the shallowest angle of incidence, $\theta_i = \theta_{max}$, can be found by examining the case in which the first-order diffraction peak ($m = 1$) occurs at $\theta_{t,m=1} = 90°$. Since $\sin(\theta_{t,m=1} = 90°) = 1$, eq. (1.1) becomes,

$$n_t + n_i \sin(\theta_{max}) = \frac{\lambda}{\Lambda_{top}} \tag{1.2}$$

which can be re-arranged as,

$$\Lambda_{top} = \frac{\lambda}{n_t + n_i \sin(\theta_{max})} = \frac{\lambda}{n_b + n_a \sin(\theta_{max})} \tag{1.3}$$

For a diffractive bottom-surface (as shown in subfigure (**b**) of fig. 1.2 on the following page), the shallowest angle of incidence, θ_{max}, must first be corrected-for by applying the Snell-Descartes equation to find $\sin(\theta_i)$,

$$\sin(\theta_i) = \frac{n_t}{n_i} \times \sin(\theta_{max}) \tag{1.4}$$

thereafter, we once again examine the first diffracted order ($m = 1$) to be propagated along the surface ($\theta_{t,m=1} = 90°$, $\sin(\theta_{t,m=1}) = 1$) which using eq. (1.1), provides,

$$n_t + \frac{n_i \times n_t}{n_i} \sin(\theta_{max}) = \frac{\lambda}{\Lambda_{bottom}} \tag{1.5}$$

which becomes,

$$\Lambda_{bottom} = \frac{\lambda}{n_t + n_t \sin(\theta_{max})} = \frac{\lambda}{n_a + n_a \sin(\theta_{max})} \tag{1.6}$$

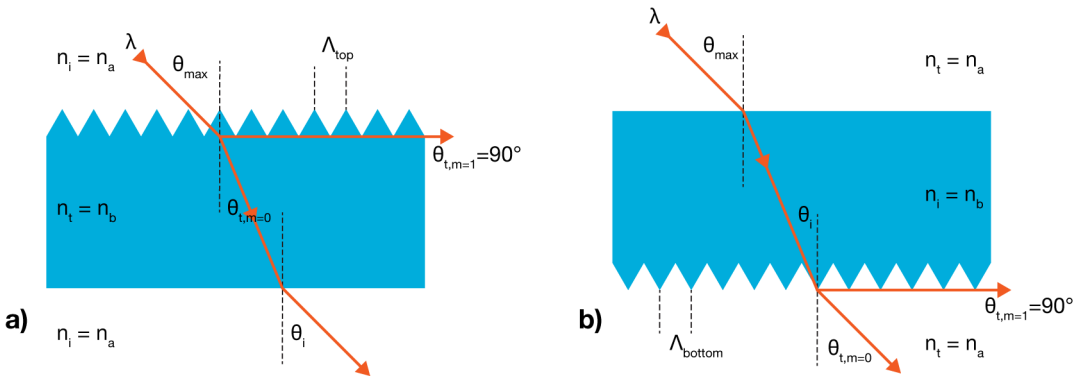

Figure 1.2: Diffraction through a nanostructured interface: the quasi-static limiting cases in which the first-order ($m = 1$) is diffracted at $\theta = 90°$ and only the zeroth-order ($m = 0$) propagates. Subfigure (**a**) shows the limiting case for a diffractive top-surface and is the subject of eq. (1.3) on page 26, whereas, subfigure (**b**) shows the limiting condition for a diffractive bottom-surface and is the subject of eq. (1.6).

Therefore, the degree to which the quasi-static condition can claim omni-directionality is found to be,

$$\Lambda_{max} = \min[\Lambda_{top}, \Lambda_{bottom}] \tag{1.7}$$

making the substitutions, $n_i = n_a$ and $n_t = n_b$ in eq. (1.3) on page 26 and $n_i = n_b$ and $n_t = n_a$ in eq. (1.6), we find,

$$\Lambda_{max} = \frac{\lambda_{min}}{\max[n_a, n_b] + n_a \sin(\theta_{max})} \tag{1.8}$$

where λ_{min} is the shortest freespace wavelength under consideration, θ_{max} is the shallowest angle of incident light, n_b is the refractive index of the nanostructured material and n_a is the refractive index of its surrounding medium.

In order to put this into context, we have used eq. (1.8) to plot periodicity as a function of angle of incidence and freespace wavelength, $\Lambda_{max}(\theta_{max}, \lambda_{min})$, for an air–glass interface ($n_{glass} = 1.5$), see fig. 1.3 on the next page.

For omnidirectional solar applications, the suggested periodicity for glass motheye nanostructures should be 170 nm in order to accept light from all angles of incidence (assuming $\lambda_{min} = 400$ nm which accounts for 95% of the solar spectrum — see fig. 4.3 on page 58). However, if only normal incidence were required a periodicity of $\Lambda = 270$ nm would be sufficient. If one were to repeat these calculations but assume the transmitting materials was a high-index material such as silicon instead of glass ($n_b = 3.44$), the allowed motheye periodicities would shrink to $\Lambda_{max} = 90$ nm (for omnidirectional operation) and $\Lambda_{max} = 115$ nm (for normal incidence). These calculations have been verified [42, 43].

1.2.2 Effective-medium approximations

As electromagnetic waves (which satisfy the quasi-static condition, above) travel through the nanocone structure they interact with an effective-medium whose refractive index gradually

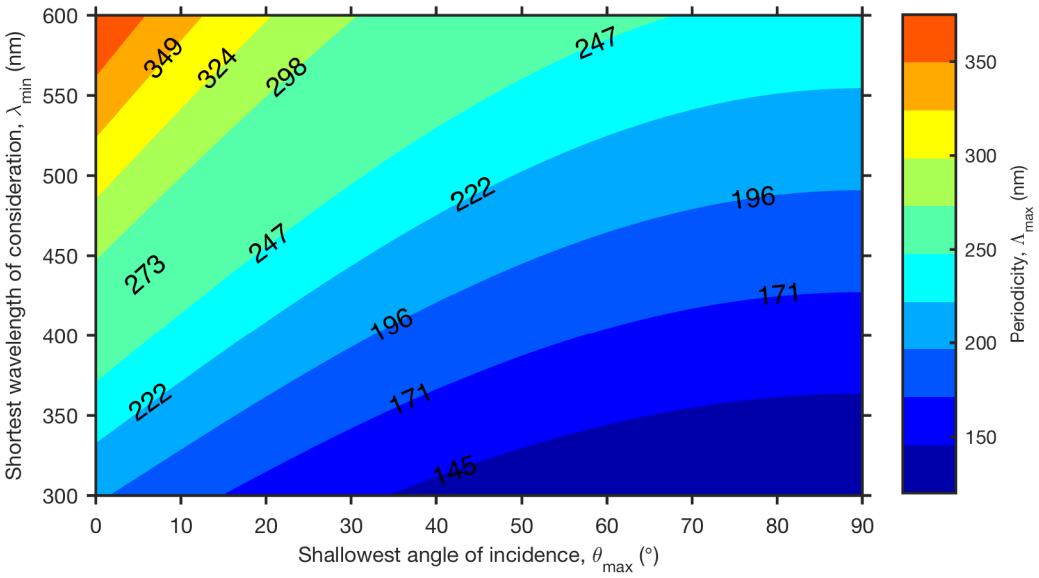

Figure 1.3: Contours representing the quasi-static condition (eq. (1.8) on page 27) for an air–glass interface ($n_{\text{glass}} = 1.5$). The maximum periodicity, Λ_{max} (coloured), of a motheye surface that supports propagation of only the zeroth-order as a function of incident angle of light, θ_{max}, and shortest wavelength for which this condition holds λ_{min}.

changes in accordance with the ratio of material-to-air. Examples of the refractive index profiles of both a flat air–glass interface and two nanostructured 'motheye' air–glass interfaces can be seen in fig. 1.4 on the next page.

In the quasi-static limit, the effective-medium of the refractive index within the nanocone region, n_{eff}, can be approximated as the sum of the volume-weighted dielectric constants of the two interface materials, $\epsilon_{substrate}$ and ϵ_{air},

$$n_{eff}(z) = \sqrt{\epsilon_{air} \cdot f_{air}(z) + \epsilon_{substrate} \cdot f_{substrate}(z)} \tag{1.9}$$

where $f_{air}(z)$ and $f_{substrate}(z)$ are the two-dimensional area-fill-ratios in the plane parallel to the surface at a height z above the bulk material [44, 45, 43].

Alternative effective-medium calculation methods exist; for example, the Bruggeman [40, 46–50] and Maxwell-Garnett methods [51, 52] — see eq. (1.10). These take the form,

$$\frac{\epsilon_{eff} - \epsilon_h}{\epsilon_{eff} + \gamma \cdot \epsilon_h} = \sum_j f_j \frac{\epsilon_j - \epsilon_h}{\epsilon_j + \gamma \cdot \epsilon_h} \tag{1.10}$$

where ϵ_{eff} is effective-medium dielectric function, ϵ_h is the dielectric function of the 'host' medium and f_j and ϵ_j are the fraction and dielectric function of an inclusion material, γ is a factor related to the screening and shape of the inclusions (for spheres $\gamma = 2$) [53]. The Bruggeman formulation of eq. (1.10) invokes $\epsilon_h = \epsilon_{eff}$, whereas the Maxwell-Garnett variation asserts that the host material (ϵ_h) must simply form the largest constituent fraction.

More sophisticated effective-medium approximations depends upon the propagation of different diffractive modes and the polarisation of incident light [42, 31, 54]. These approximations invoke a power-series expansion with terms depending upon the interface's specific geometry and are principally employed by calculation techniques such as Rigorous

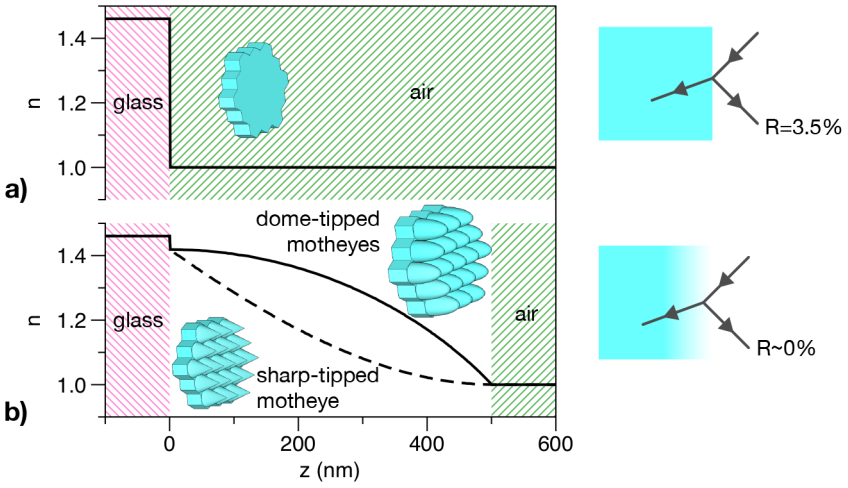

Figure 1.4: Effective-medium approximations of the refractive index profile (n(z), $\lambda = 1000\,\text{nm}$) at the air–glass interface for: (**a**) a flat glass surface; and (**b**), two motheye-nanostructured surfaces. The motheye surfaces are modelled as tapered glass-nanostructures with a height of 500 nm. They are hexagonally-packed ($\Lambda = 100\,\text{nm}$) with a circular base-width that fills 90% of the underlying flat surface which causes the small discontinuity at $z = 0$. The refractive index profiles for both 'dome-tipped' (solid line, maximum conical radius of curvature) and 'sharp-tipped' (dashed line, minimum conical radius of curvature) nanostructures were calculated using eq. (1.9) on page 28.

Coupled Wave Analysis [55].

Calculations of the effective-medium refractive index profile for our motheye interfaces using the Bruggeman and Maxwell-Garnett methods provide qualitatively identical results; only differing in the magnitude of the effective-medium refractive index, not its shape. In fact, differences in the effective medium approximation using eq. (1.9) on page 28 and eq. (1.10) on page 28 are negligible (or zero) when only non-lossy dielectric materials are considered. Numerical differences between each of the effective medium theories become pronounced when the extinction coefficient of the materials used in the calculation (imaginary part of the refractive index) is non-zero. For the remainder of this work we will use the form of eq. (1.9) on page 28 as an approximation of the effective medium refractive index for nanostructured interfaces as it facilitates adequate discussion.

1.2.3 Anti-reflection

At a *flat* interface between two materials with refractive indices n_1 and n_2, the fraction of incident power that is reflected (at normal incidence), R, is given by the Fresnel equation,

$$R = \left|\frac{n_1 - n_2}{n_1 + n_2}\right| r^2 \tag{1.11}$$

The step-discontinuity that occurs at the flat interface between air and glass in subfigure (**a**) (fig. 1.4) causes Fresnel reflection to occur. For many applications involving low index-contrast materials, reflectance is often tolerable ($R = 3.5\%$ for air-to-glass, $n_{glass} = 1.46$). However, when working with high index-contrast materials, flat-interface reflectance can be excessively high ($R = 30.2\%$ for air-to-silicon, $n_{silicon} = 3.44$).

Motheye interfaces exhibit very low reflectance (and consequently high transmittance)

due to optical impedance-matching. The interfacial effective-medium refractive index gradually increases as the planar-fraction of air-to-substrate increases (subfigure (**b**)). Small reflections do occur at each change in optical density. However, as these reflections occur continuously over the entire tapered nipple height (and crucially with different phases), the summed reflectance is very low. Empirically (and for normal incidence), the minimum height, h_{min} of the tapered cone has been shown to be,

$$h_{min} \approx 0.4 \times \lambda_{max} \tag{1.12}$$

where, λ_{max} is the longest wavelength for which the anti-reflection condition holds [27]. Unsurprisingly, the height of a moth's corneal nipples do not typically exceed $h = 230\,\text{nm}$ as the summed anti-reflection criteria is satisfied for most of the visible spectrum.

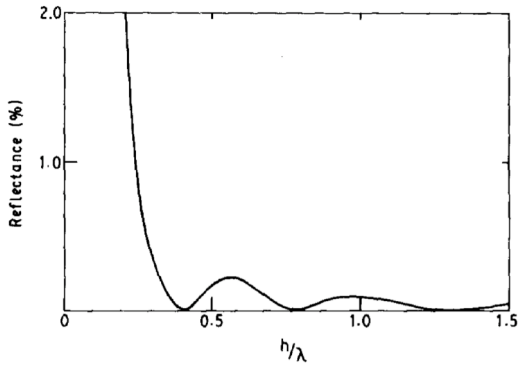

Figure 1.5: Reflectance as a function of the motheye nanostructures height and the wavelength of incident light, $R(\frac{h}{\lambda})$. The observed 'sinc-like' function gives rise to eq. (1.12). This figure is a reproduction from [27].

Together, fig. 1.3 on page 28 and eq. (1.12) provide a good indication of the pitch (Λ) and height (h) of the motheye nanostructures required for the proposed smart window application — they expose the relationship between optical bandwidth and the aspect ratio ($\frac{h}{\Lambda}$). However, the optical requirements for Motheye Smart Windows are complex and competing: firstly, to transmit visible light; secondly, to modulate solar energy transmittance (through either reflection or absorption) – it is not a simple case of targeting the highest bandwidth (largest aspect-ratio). Instead, we must turn toward numerical optimisation; an extensive study of the system-specific optimum geometry for Motheye Smart Windows is provided in chapter 7 on page 81.

1.2.4 Optimum refractive index profiles

The rate of taper along the nanocone, from tip to base, can make a significant difference to the anti-reflection performance of a motheye interface. Southwell showed that in order to suppress reflections over the broadest bandwidth a 'near-optimum' refractive index profile exists, n_{opt}, which follows a quintic form [45],

$$n_{opt}(u) = n_s - (n_s - 1) \cdot (10u^3 - 15u^4 + 6u^5) \tag{1.13}$$

where n_s is the refractive index of the nanostructured substrate material and u is the normalised optical thickness which ranges from $u = 0$ at the fully-dense plane (bulk-

substrate interface) to $u = 1$ at the air-interface plane. The function (including both its first- and second-derivatives) smoothly matches between both air and the substrate material, see fig. 1.6.

Optical thickness, u, is defined as,

$$u = \int_0^z n\delta x \tag{1.14}$$

or in a differential form,

$$\delta u = n\delta z \tag{1.15}$$

where z is the physical thickness (height above the bulk-substrate). Therefore, in order to determine the near-optimum refractive index profile, n_{opt}, with dependence upon *physical thickness*, one must first perform the integral,

$$z = \int_0^u \frac{\delta u'}{n(u')} \tag{1.16}$$

Following this, eq. (1.16) must be inverted in order to obtain u as a function of z. The resulting expression, $u(z)$, can then be substituted into eq. (1.13) on page 30 in order to obtain the optimum refractive index as a function of physical thickness, $n_{opt}(z)$. Numerical methods must be used to obtain $n_{opt}(z)$ as there exists no known closed-form solution to the integral in eq. (1.16) [45].

Two applications of the above equations for near-optimum index matching at an air-silicon interface and at an air–glass interface can be seen in subfigures (**b**) and (**c**) of fig. 1.6. For square-array nanostructures, it can be seen that a fast rate of taper (resulting in sharp-tipped cones) is required when index-matching between air and a high-index substrate. Whereas, when indexing between air and a lower-index material, a more gradual rate of taper is required.

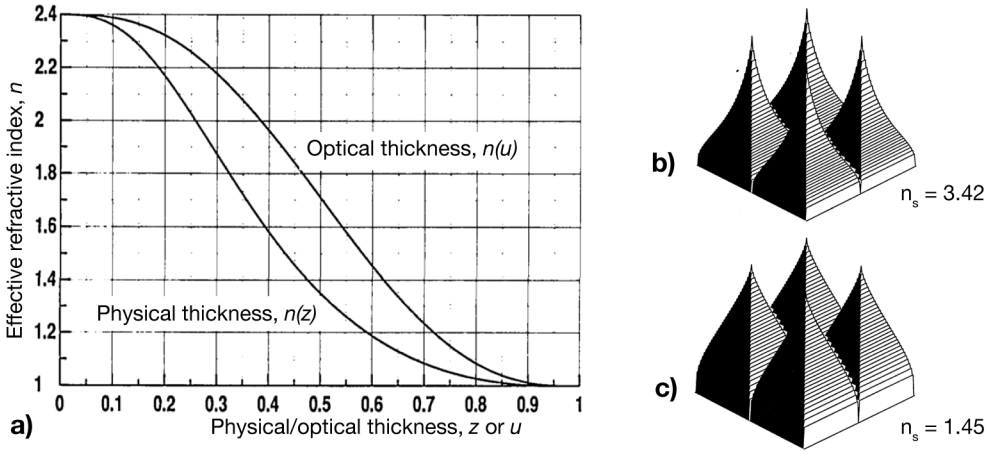

Figure 1.6: (**a**) The 'near-optimum' index matching refractive index profile for motheye nanostructures at an air-dielectric interface ($n_s = 2.4$) [45]. The equation has a quintic form (eq. (1.13) on page 30) and is smooth in both its first- and second-derivative. Two 'quintic', square-array near-optimum index matching nanostructures are shown in subfigures (**b**), for an air-silicon interface, and (**c**), for an air–glass interface.

Southwell showed that motheye interfaces which follow the quintic profile (eq. (1.13)

on page 30) exhibit height-dependent broadband reflectance values,

$$h > \lambda_0 \qquad R < 0.01\% \qquad \forall\lambda < \lambda_0 \tag{1.17}$$

$$h > \frac{\lambda_0}{2} \qquad R < 0.5\% \qquad \forall\lambda < \lambda_0 \tag{1.18}$$

where R is the power reflected at each wavelength, h is the physical thickness of the quintic matching region and λ_0 is the shortest wavelength for which each condition holds. This is in good agreement with the empirically derived relationship, eq. (1.12) on page 30.

In spite of the near-optimum performance of the quintic motheye profile, it has been noted that *naturally* occurring corneal nipples do not follow this shape. Instead, they are typically parabolic or Gaussian [40]. However, a recent study showed that a quasi-random distribution of nanostructure heights (exhibited in biological systems) could be used to engineer specific refractive index profiles [51]. Therefore, it is still possible to obtain a 'near-optimum' anti-reflectance effective-medium refractive index profile — even if the specific shape of each nanostructure is 'non-ideal'.

Motheye anti-reflection structures are generally employed to index-match between *two* materials i.e. between a bulk, substrate material and its surrounding medium (air-to-glass [56], air-to-silicon [36] or polymer-film-to-silicon [57]). It is important to acknowledge that the quintic equations described in this section *do not* represent the layered architecture proposed for Motheye Smart Windows (nanostructured glass with a conformal coating of VO_2). Our Motheye Smart Windows operate by index-matching between *three* materials using a single nanostructure: air, VO_2 and glass.

As discussed previously, the requirements for Motheye Smart Windows are complex. Anti-reflection is desirable in the visible region, however, transmittance of near-infrared solar energy must be modulated between its two temperature states. Southwell's quintic profile provides a point of reference in order to begin optimising Motheye Smart Window interfaces. However, it is not a nanostructure profile that *must* be re-created for our specific window application. Indeed, some degree of mis-matching (inducing reflection) may be desirable. We include a study into the optimisation of the best refractive index profiles for Motheye Smart Windows in chapter 7 on page 81.

1.2.5 Surface distributions

Early studies of naturally occurring motheye surfaces described the nipple distribution as 'crystalline, and hexagonally close-packed' (the densest arrangement for circular object-packing on a flat surface). It has also been common to fabricate or find analytical results for square arrays of tapered nanocones [58, 55]. Most numerical calculations regarding the optical properties of motheye nanostructured interfaces assume an infinitely-regular/crystalline square (or hexagonal) surface distribution.

A unique study, which used Fourier analysis to asses the affect of symmetry-breaking surface distributions, concluded that poly-crystalline arrangements (short-range, tiled crystal domains that mimic naturally occurring motheye distributions) help to suppress the intensity of the minus-1 diffraction order, particularly at high angles of incidence [38].

This is due to the observation that a backscattered diffraction pattern's order of symmetry is a direct function of the underlying nanostructure-distribution. Therefore, reflection from polycrystalline nanostructures with a range of orientations will 'smear' the minus-1 diffraction order — reducing its intensity at specific azimuthal angles. The authors argued that the 'tiled', polycrystalline surface distributions of naturally occurring motheyes help to avoid iridescence-effects which, under certain illumination conditions, could degrade their anti-reflection camouflaging.

1.2.6 Hierarchical motheye interfaces

There are numerous studies which depart from conventional nanocone biomimicry of motheyes by employing exotic, hierarchical nanostructures to suppress reflection over a broader range of wavelengths [48, 36, 59–61], see fig. 1.7. Hierarchical motheye interfaces, by their nature, exhibit multiple periodicities and as a result have attracted attention for their (potentially) increased anti-reflection bandwidth. For example, [59] simulated hemi-urchin spines on the cones and [59] used nipples with a pore in the centre. Inverted-paraboloids, holes and inverted cones have also been explored [61]. Simulation of bi-hybrid motheye structures with two different heights [48] reduced reflection by 50-70% when compared to uniform motheye structures with one height.

Three of the mechanisms by which reflection could be suppressed at a nanostructured interface are: index-matching into the zeroth-diffraction order of the transmitting medium (specular transmission); scattering or diffraction into higher orders of the transmitting medium (non-specular transmission); or, absorption at the interface. A combination of the former (specular transmission) and latter (absorption) is of interest for Motheye Smart Window applications. However, the primary focus for most of the studies listed above is the *suppression of reflection* and limited discussion is devoted to which of the above mechanisms is employed to achieve this effect. Therefore, further analysis of each specific geometry would be required to identify the fate of electromagnetic waves interacting with hierarchical motheye interfaces — this is outside the scope of our present work.

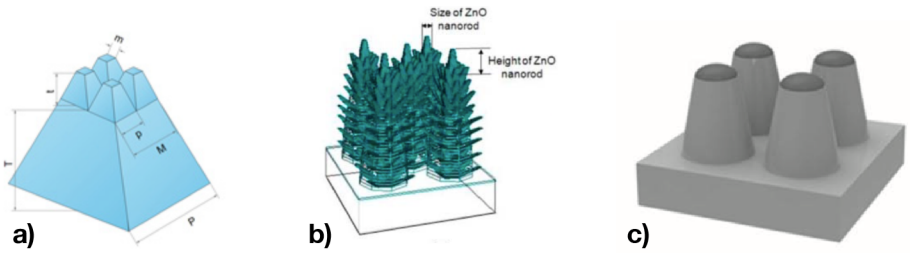

Figure 1.7: Examples of bespoke motheye anti-reflection nanostructures as featured in the work of: (**a**) Bruckner [36]; (**b**) Ko [59]; and (**c**) Park [62].

1.3 Wettability

The motheye surface structure is known to exhibit several coincidental functionalities. For example, motheye nipples provide a 'structurally anti-microbial surface' due to the ability of the nanostructure to inhibit the attachment of both bacterial and mammalian cells [63].

However, it is the ability of nanostructured motheye interfaces to enhance the wettability of a surface that has commanded the most attention as a secondary feature.

Motheye nanostructures can promote either super-hydrophobicity or super-hydrophilicity, depending upon the intrinsic wettability of the substrate/interfacial material. In the case of super-hydrophobicity, air is trapped between the high-aspect-ratio nanostructures and prevents water droplets on the surface collapsing from a Cassie–Baxter to Wenzel state [24, 20]. This can allow a nanostructured surface to become 'self-cleaning'.

Self-cleaning windows maintain optimum optical performance year -round as dust and contaminants are regularly removed by rain thereby avoiding the requirement for regular physical or chemical cleaning. This feature is not only attractive for aesthetic reasons but provides a strong economic advantage too. In particular, when the costs of cleaning conventionally inaccessible windows on large buildings come into consideration. The synergy of a self-cleaning surface allied to a dynamic greenhouse effect (the proposed thermochromic motheye smart window system) may allow maintenance savings to offset purchase and installation costs — even before taking into account heating/cooling energy-savings from the use of a dynamic system.

1.3.1 Wetting models

Quantification of a surface's wettability is principally achieved by studying the contact angle made between a droplet and the surface it sits upon. Young showed that the contact angle ($\theta_{\text{CA-Y}}$), in its most simplified form, is dictated by the interfacial energies between: a solid-liquid, γ_{SL}; a solid-vapour, γ_{SV}; and a liquid-vapour, γ_{VL},

$$\cos\left(\theta_{\text{CA-Y}}\right) = \frac{\gamma_{\text{SV}} - \gamma_{\text{SL}}}{\gamma_{\text{VL}}} \tag{1.19}$$

This equation assumes that no external forces are acting upon the droplet and that the surface it sits upon is perfectly smooth and chemically homogeneous — clearly a highly-idealised situation, see subfigure (**a**) in fig. 1.8 on the following page.

Young's equation (eq. (1.19)) was modified by Wenzel in 1936 in order to account for the effect non-smooth surfaces have upon wettability. Wenzel's model assumes that the water droplet remains in full-contact with the substrate, see subfigure (**b**) in fig. 1.8 on the following page. In order to account for the (roughness-induced) increased solid-liquid surface area and its distortion of the surface energies, Wenzel's contact angle ($\theta_{\text{CA-W}}$) is found to be

$$\cos\left(\theta_{\text{CA-W}}\right) = \frac{\text{projected surface area}}{\text{planar surface area}} \times \cos\left(\theta_{\text{CA-Y}}\right) \tag{1.20}$$

$$\cos\left(\theta_{\text{CA-W}}\right) = R \times \frac{\gamma_{\text{SV}} - \gamma_{\text{SL}}}{\gamma_{\text{VL}}} \tag{1.21}$$

where R is referred to as the 'roughness factor'.

Following Wenzel's adaption of Young's equation, a third wetting model was proposed by Cassie and Baxter in 1944. This model describes a rough surface which allows air to be trapped between itself and the droplet sitting upon it, see subfigure (**c**) in fig. 1.8 on the next page. The Cassie–Baxter contact angle ($\theta_{\text{CA-CB}}$) is characterised by the ratio of

contact area between the substrate-droplet, ϕ_s, and trapped–air-droplet, $\phi_a = 1 - \phi_s$,

$$\cos(\theta_{\text{CA-CB}}) = \phi_s \cos(\theta_{\text{CA-Y}}) - \phi_a \tag{1.22}$$

which can be re-arranged and expressed as a function of surface energies,

$$\cos(\theta_{\text{CA-CB}}) = -1 + \phi_s[\frac{\gamma_{SV} - \gamma_{SL}}{\gamma_{VL}} - 1] \tag{1.23}$$

A more complex expression of eq. (1.23) is required if partial penetration of the droplet into the nanostructure is to be considered. The form shown above assumes that the bottom-surface of the water droplet is not distorted by the nanostructure it sits upon i.e. it is 'flat-bottomed'.

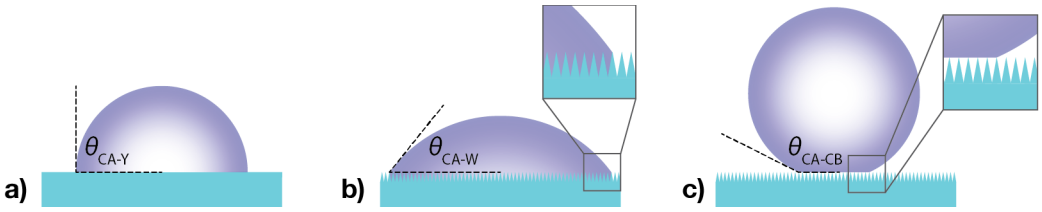

Figure 1.8: The three principal models used describe the wetting properties of a surface. Subfigure (**a**), the Young's model (eq. (1.19) on page 34); (**b**), the Wenzel's model (eq. (1.21) on page 34); (**c**), the Cassie–Baxter model (eq. (1.23)).

Young's equation (eq. (1.19) on page 34) shows that a surface's 'wettability' is a function of the chemical affinity between water the substrate material (γ_{SL}) i.e. high surface-energies exhibit low contact angles (termed 'hydrophilic') whereas, low surface-energies result in high contact angles (termed 'hydrophobic'). Wenzel's contribution (eq. (1.21) on page 34) was to show that a surface's micro/nanostructure will enhance the inherent (chemically induced) wettability of a surface. However, what Cassie and Baxter showed (eq. (1.23)) is that the effect of air-trapping is always to *increase* the droplet contact-angle (relative to a flat substrate with an identical chemical composition) as air is hydrophobic.

Super-wetting surfaces are defined as either 'super-hydrophilic' (if $\theta_{CA} \leq 10°$) or 'super-hydrophobic' (if $\theta_{CA} \geq 150°$). It was shown that the maximum achievable contact angle for a flat surface through chemical modification is $\theta_{CA} \approx 130°$ [64, 24]. Therefore, air-trapping micro/nanostructures *must* be employed (in conjunction with surface chemistry modification) in order to access super-hydrophobic functionality.

1.3.2 Transition

Transition from a Cassie–Baxter (trapped-air) to Wenzel state (full-wetting/contact)is possible when the water hammer-pressure is exceptionally high. This can occur when a droplet hits a surface at a high velocity, for example on the windshield of a fast-moving vehicle such as a plane. However, most window applications will not experience such high water impact speeds. For window applications, it would be adequate if the Cassie–Baxter state was maintained for droplets travelling up-to the terminal velocity of rain for a sky-facing windows (5 to 13 m/s [65, 66]) or significantly less than this for windows mounted on the vertical face of a buildings.

Water hammer pressure (P_{WH}) is defined as,

$$P_{\mathrm{WH}} \approx 0.2\rho c V_0 \tag{1.24}$$

where ρ is the droplet's liquid density, c speed of sound in the liquid and V_0 is the impact velocity of water [67].

It has been shown that the critical pressure required to force a millimetric droplet's liquid meniscus into a tapered hexagonal array of nanostructures (cones) is,

$$P_{\mathrm{crit}} = \frac{4\pi\gamma r \cos\left(\theta_{\text{CA-tip}} - \alpha\right)}{\sqrt{3}\Lambda^2 - 2\pi r^2} \tag{1.25}$$

where r is the radius of curvature of the three phase contact-line entering the nanostructure, γ is the surface tension of water (72 mNm^{-1}), 2α is the opening angle of the tip of the tapered cones and $\theta_{\text{CA-tip}}$ is the impinging contact angle with respect to the side-wall of the nearest nanostructure [68, 67].

By equating eq. (1.24) and eq. (1.25) we can express (as a first approximation) the droplet impact velocity, V_{crit}, that causes transition from a Cassie–Baxter to Wenzel state as,

$$V_{\mathrm{crit}} = \frac{1}{0.2\rho c} \times \frac{4\pi\gamma r}{\sqrt{3}\Lambda^2 - 2\pi r^2} \tag{1.26}$$

when $\cos\left(\theta_{\text{CA-tip}} - \alpha\right) = 1$.

Figure fig. 1.9 on the following page shows the interplay between the periodicity and radius of curvature of motheye nanostructures in defining the critical velocity that causes wetting of a droplet upon impact. Sparse nanostructures (large periodicities, Λ) require that the radius of curvature is also large in order to prevent wetting. Densely-packed nanostructures are more resistant to wetting as the critical three phase deformation required is much larger.

1.3.3 Self-cleaning

The 'lotus leaf' self-cleaning effect is observed when rain-droplets remove contaminating dust particles from the surface of a leaf. Impinging water droplets bead, pick-up contaminants and roll-off (see fig. 1.10 on the next page).

Up until this point we have been discussing 'static' contact angles i.e. when the surface a droplet sits upon is perfectly flat, $\theta_{\mathrm{tilt}} = 0°$. However, when tilted, the measured contact angles at each edge of a droplet are observed to differ. This requires us to further define the 'receding' and 'advancing' contact angles, $\theta_{\text{CA-R}}$ and $\theta_{\text{CA-A}}$ respectively (see fig. 1.11 on page 38). The critical figure of merit for self-cleaning surfaces is the contact angle hysteresis (θ_{CAH}),

$$\theta_{\mathrm{CAH}} = \theta_{\text{CA-A}} - \theta_{\text{CA-R}} \tag{1.27}$$

which in turn defines the roll-off (or 'sliding') angle, $\theta_{\text{roll-off}}$; evaluated to be approximately,

$$\theta_{\text{roll-off}} = \arcsin\left(\frac{r_{\mathrm{drop}}\gamma_{\mathrm{LV}}\cos\left(\theta_{\mathrm{CAH}}\right)}{mg}\right) \tag{1.28}$$

where g is the gravitational constant and r_{drop} is the radius of the water droplet [69].

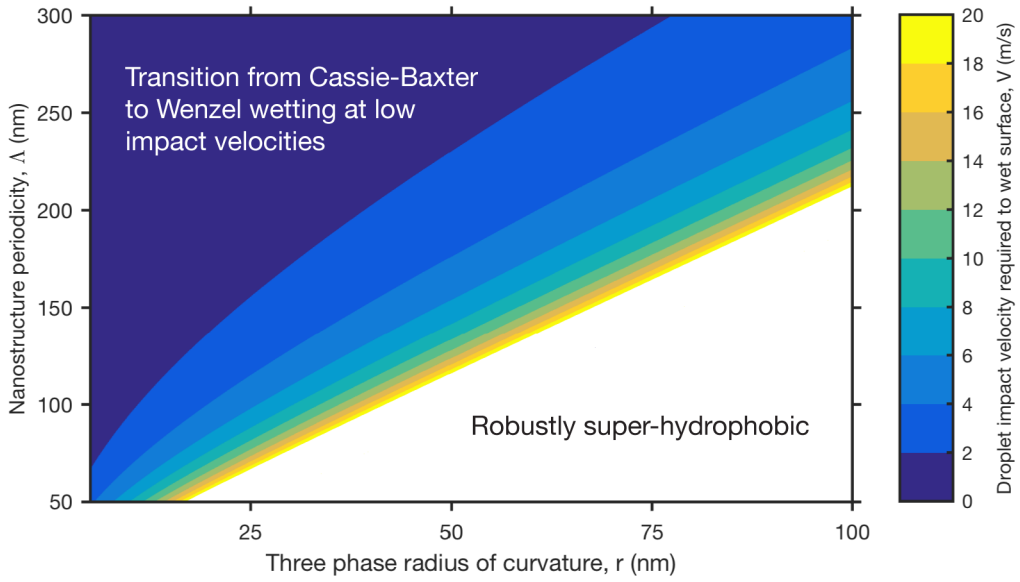

Figure 1.9: The critical droplet velocities (V_{crit}) that lead to a transition from Cassie–Baxter to Wenzel wetting using eq. (1.26) on page 36. The nanostructures are considered to be periodic (Λ) and exhibit a break-through three phase radius of curvature, r. The top-left region (sparse nanostructures) are easily wetted whilst droplets hitting the bottom-right region will remain in their Cassie–Baxter state, 'robustly superhydrophobic'.

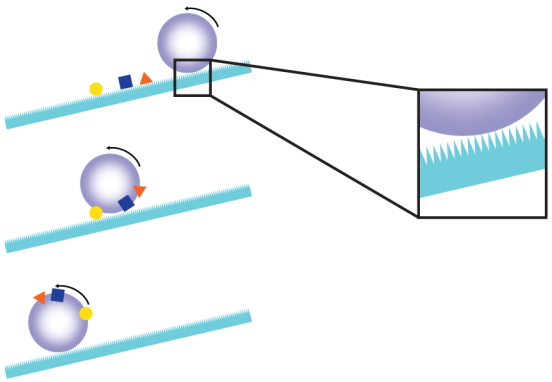

Figure 1.10: The super-hydrophobic 'lotus leaf' self-cleaning effect. Rain-droplets are able to remove contaminating dust particles from the surface of a leaf by beading, picking-up contaminants and then rolling-off.

Generally, surfaces with low contact angle hysteresis also exhibit low roll-off angles.

Not *all* Cassie–Baxter surfaces exhibit low roll off angles. If the surface has blunt nanostructures (high ϕ_s) then 'pinning' occurs. In which case, the receding contact angle becomes,

$$\cos(\theta_{\text{CA-R}}) = 2\phi_s - 1 \tag{1.29}$$

and consequently θ_{CAH} also increases [67]. This effect can also occur for non-blunt nanostructures due to water penetration at high droplet impact velocity — the droplet will remains in a Cassie–Baxter state with a high contact-angle but will have limited mobility and therefore a contact angle hysteresis close to 90°.

In order to self clean (like a lotus leaf), the droplet must be able to easily roll-off the surface. For the above reasons, the tapered/pointed nanostructures defined by motheye antireflection surfaces (very small ϕ_s) are ideal for 'lotus leaf' self cleaning; providing that they exhibit a hydrophobic surface chemistry and also have a high nanostructure surface fill-factor, with few defects if any.

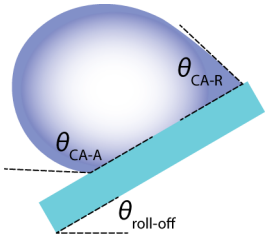

Figure 1.11: Contact angle hysteresis approaching $\theta_{\text{CAH}} \to 90°$ causing a high roll-off angle. This effect prevents self-cleaning from taking place and can be caused by 'pinning' (due to blunt nano- or micro-structure) or impalement (due to a high droplet impact velocity).

1.3.4 Hydrophobic functionalisation

Untreated glass is known to be mildly hydrophilic. Therefore, a hydrophobic surface-chemistry must be induced in order to enable this mode of self-cleaning for motheye nanostructured glass. An example of one method to do this is to locally evaporate hexamethyldisilazane which leaves (hydrophobic) silane groups on nearby surfaces and increases the contact angle of water droplets upon them [70, 71]. Commercial chemicals such as Sigmacote, which contains chlorinated organopolysiloxane, provide a similar method for increasing the hydrophobicity of a surface such as glass. Alternatively, the deposition of thin fluoropolymer layers on a surface is also known to induce hydrophobicity. Our methods to perform these functionalisations are described in section 8.2.7 on page 113.

1.4 Fabrication review

A distinction should be made between the fabrication of effective-medium graded-index nanostructures with an associated length-scale and those without. Techniques that induce nanostructures without a well-defined average-periodicity, Λ, are typically 'maskless' (or non-lithographic). An additional mode of comparison between fabrication techniques for effective-medium graded-index nanostructures is whether the method is 'additive' or 'subtractive'.

We will begin by discussing different additive and subtractive methods for creating nanostructured anti-reflection interfaces. Following this, we will move on to a discussion of lithographic and maskless techniques for their fabrication. Our final section on lithographic masking techniques makes a distinction between top-down and bottom up methods, both of which are covered in detail.

Additive formation of nanostructured interfaces

The 'additive' approach toward index-matching two materials (by adding a third, structured interfacial material) has been explored since the early 1970s. The first imitation of motheye nanostructures was created by laser interference lithography [72]. Exposure of a photoresist by two orthogonal standing wave patterns gave rise to a defined, sub-wavelength periodicity with a square surface distribution. A subsequent development step removed the un-exposed material.

The drawback of this approach is that, in most cases, adding a nanostructured interfacial material only index-matches between air and the interfacial material; not between the interfacial material and the bulk substrate. This is not a problem for 'anti-reflection' applications when the interfacial material is *absorbing*. However, for improved 'transmissivity', any difference in refractive index between the interfacial material and the substrate will lead to reflection losses. An advantage of the additive approach is that a single process can be applied to many different types of flat substrate without major modifications to the technique [73].

Intermediary-index porous films provide an anti-reflection alternative to continuously-increasing refractive index motheye nanostructures. Two examples of additive techniques for creating intermediary-index layers with a defined periodicity are provided by the 'opal' close-packing self-assembly behaviour of nanospheres deposited from a colloidal solution [74–76] deposited using the 'Colvin' capillary method [77–80] or the phase-separation within a block-copolymer [81–83]. Both techniques are capable of creating sub-wavelength porous nanostructures over large areas and at low cost. However, neither technique alone can form an interface with the smooth and continuous variation of refractive index exhibited by tapered motheye nanocones.

Subtractive nanostructured interfaces of bulk materials

Subtractive approaches toward motheye fabrication, in which the nanostructure is 'cut' ('imprinted') into a planar substrate material, offer the advantage that only a single interface between the substrate and surrounding medium exists. These techniques typically involve the deposition of a sacrificial mask (with a defined periodicity) followed by an anisotropic etching process.

Reactive Ion Etching is a favoured 'subtractive' nanofabrication processes as it exploits chemical contrasts between a mask and substrate in order to produce high aspect-ratio structures. The etching process is performed by pumping a chamber with low-pressure reactive fluorine gases and striking a plasma. Reactive ions are drawn out of the plasma by an applied DC bias and bombard the sample, giving rise to a directional etch. The choice of gases, chamber pressure and radio-frequency power must be made carefully in order to

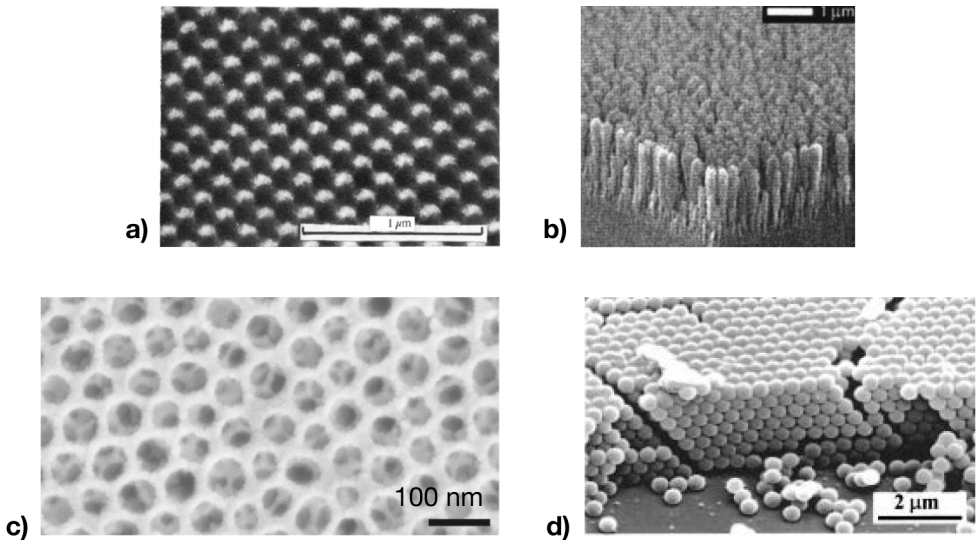

Figure 1.12: Examples of additive approaches toward fabricating motheye antireflection nanostructures. (**a**) Photoresist nanostructures formed by interference lithography by Clapham and Hutley [72]. (**b**) Nanostructures formed by Glancing Angle Deposition by Hawkeye and Brett [84]. (**c**) A nanostructured thin film formed via Block Copolymer phase seperation by Guldin et al. [81]. (**d**) Nanosphere colloidal crystal formed via the 'Colvin' method by Jiang et al. [85].

translate the mask pattern into the correct substrate features. Common gases for SiO_2 etching include SF_6 [38], CHF_3 [86, 57, 20] and CF_4 [87–89, 56].

During the etch process fluoropolymers, products of the ion-SiO_2 reaction, are deposited locally [86]. These polymers facilitates high aspect-ratio etching as they mask the sidewalls of nanofeatures. However, if their deposition is excessive the substrate etching process is severely hindered. For this reason, a secondary gas such as O_2, H_2 [56, 90, 89] or Ar [87, 88] may be simultaneously added to the chamber in order to strip back deposited polymer and allow the etch to continue correctly. A final cleaning step is sometimes required following reactive ion etching in order to remove all residual polymer, this can take the form of either piranha cleaning or O_2 plasma ashing [56].

There are some rare examples of 'self-masking' reactive ion etches in which deposited polymer from an early part of the etch process acts as a mask that seeds nanostructures created in the later part of the process [91, 92]. The two drawbacks are that: (a) control over the average periodicity and profile of each nanostructure is limited; (b) the chemical contrast of the polymer etch mask may be poor.

1.4.1 Maskless techniques

The critical drawback for maskless etching is that since the average periodicity, Λ, is not strictly controlled it cannot be guaranteed that the sub-wavelength 'quasi-static' condition is satisfied. Therefore, scattering effects can become problematic [93].

Two common examples of 'subtractive' maskless fabrication are wet chemical etching of glass with acid and phase-separation followed by calcination during a high-temperature sintering process. Other ('additive') examples include Radio Frequency Magnetron Sputtering of Al_2O_3 [93], Pulsed Laser Deposition of ZnO [73], Seedless Flame Spray Pyrolysis of SiO_2 [94] and Glancing Angle Deposition of either MgF_2, TiO_2 or SiO_2 [47, 84, 52].

These processes produce tapered nanostructures as an intermediary layer with a gradually increasing refractive index, thereby operating in a similar way to motheye tapered nanostructures. However, the principal drawback discussed above (limited control over the nanostructure periodicity) renders these techniques unappealing for our current work.

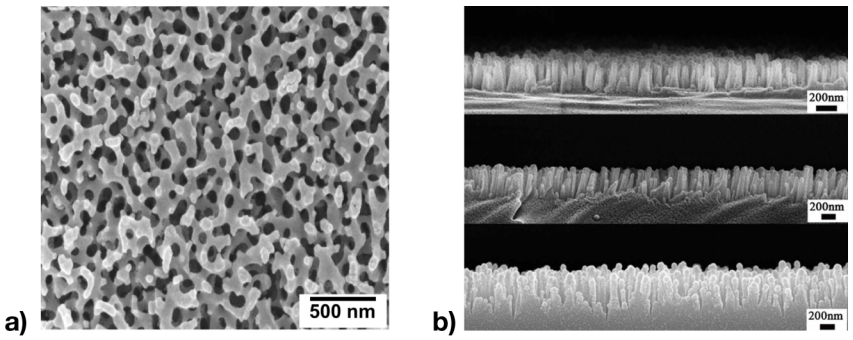

Figure 1.13: Examples of maskless fabrication methods which produce sub-wavelength nanostructures. (**a**) Phase separation of glass formed in a high-temperature process by Aytug et al. [93]. (**b**) Nanostructures formed through self-masking during Reactive Ion Etching by Ye et al. [91].

1.4.2 Sub-wavelength lithographic masking

The creation of a masking layer with an average, sub-wavelength periodicity is crucial for most subtractive motheye fabrication methods and can also be required as a 'seed' for some additive methods [47]. There are two approaches toward creating a patterned mask: 'top-down' and 'bottom-up'. Following the creation of patterned resist, samples are either etched directly (using the resist as a reactive ion etch mask) or inverted into a metallic Cr [95] or Al [38, 92] hard-mask using a lift-off process in order to increase the etch-selectivity.

'Top-down': dictated masking

'Top-down' masking covers most conventional approaches toward lithography: the pattern is explicitly defined and often highly regular. Breaking into the sub-wavelength length-scale is the major challenge for 'top-down' lithography. The requirement for the motheye features to have an average periodicity of 100–200 nm immediately rules out the use of conventional near-UV photolithography in which a pattern is written to photoresist by shadow-masking from a partially transparent 'master' [35]. However, two 'top-down' methods are capable of creating patterns on this scale: Electron Beam Lithography and Interference Lithography. Both techniques involve crosslinking regions of a resist material and then chemically developing the pattern thereby washing away either the exposed or unexposed regions ready for the next stage of fabrication.

Electron Beam Lithography involves programming an exposure pattern which is scanned onto a positive-tone resist (such as PMMA [96] or 'ZEP' [97]) or a negative-tone resist (such as 'HSQ' [98]) [38]. The exposure is explicit: the shape and position of every element in the design is known. This serves as both an advantage and disadvantage: arbitrary patterns can be written but the process has a very limited throughput due its serial nature.

For example, writing a $6 \times 6\,\text{mm}$ array of $\Lambda = 250\,\text{nm}$ circles may take approximately 14 hours to complete [95].

Exposing a region of resist involves passing an electron beam through the area; it is therefore a challenge to write patterns to non-conductive substrates as local charging deflects and defocuses the beam. For this reason Electron Beam Lithography is most popular for writing motheye patterns on non-charging substrates such as silicon [38, 36]. However, methods to overcome charging effects using either conductive polymers [95] or metalisation have been developed and Electron Beam Lithography has been demonstrated as a feasible way of writing motheye patterns on glass (albeit over small areas).

The popular alternative 'top-down' method for producing motheye patterns is Interference or Holographic Lithography which exploits fringes produced by coherent laser beams to expose regions of a resist, often hydrogen silsesquioxane [20, 57]. Although the exact position of each nanofeature is not defined, their distribution is and typically takes the form of a square array [99], however, hexagonal arrays have also been produced using multiple beams [58]. This technique has seen use in both additive [72], and more recently, subtractive fabrication processes [20]. A strong advantage for this top-down method is that it is possible to produce nanoscale features over large areas, such as 8-inch wafers [58]. However, since the patterns are produced using an electromagnetic interference effect their periodicity remains a function of the laser wavelength used to create them. Therefore reaching the $\Lambda \leq 150\,\text{nm}$ regime is a challenge. Periodicities are commonly on the order of 200–235 nm [20, 57]; adequate for a moderate range of angles in glass but unable to satisfy the quasi-static condition for higher-index materials over the full range of angles of incidence, see fig. 1.3 on page 28.

'Bottom-up': self-assembled masking

Self-assembled masks exploit the properties of fluids, nanoscale objects and emulsions to form predictable patterns. Colloidal Nanosphere Lithography and Bloch Copolymer Lithography dominate 'bottom-up' lithography, they are typically cheap to produce and can extend over large areas. This approach to masking is well suited to motheye surfaces as the average periodicity is reliably subwavelength and the long-range order of the nanostructures is not critical.

Nanosphere masks are formed by monolayers of monodisperse spheres, typically polystyrene (latex) [56, 100, 60] or SiO_2 (silica) [50, 101, 74]. Strong Coulomb interactions, due to their high surface area to volume ratio, help the nanospheres arrange into highly-dense hexagonal surface distributions with an average periodicity equal to their diameter. The key strength of this type of mask is that the average periodicity is directly related to size distribution of the nanospheres which can be synthesised or purchased as monodisperse colloidal solutions with particle diameters as small as 5 nm up to tens of microns; the desirable $\Lambda \approx 100\,\text{nm}$ falls directly within this range.

The formation of a dense nanosphere monolayers is at the heart of the Colloidal Nanosphere Lithography process. Several variants of the monolayer formation technique exist, these include: evaporative assembly, spin-coating, Langmuir-Schaefer and Langmuir-Blodgett depositions. The ability of the host liquid to wet the substrate is critical in all of these processes and it is regular for the substrate to undergo surface group modification

prior to the deposition to enhance its wettability. This often involves either a piranha clean or a low-power O_2 plasma exposure.

Evaporative assembly is the simplest form of monolayer deposition. A volume of colloidal solution is allowed to wet the surface of the substrate, as the host liquid evaporates the mobility of the nanospheres restricted until finally they are set in place. This deposition technique often results in 'coffee staining' whereby convective currents create multilayer regions at the edge of the original colloidal puddle. Monolayer regions are created but do not have regular coverage.

Spin-coating involves either 'drop-' or 'puddle-casting' colloidal solution onto a substrate mounted in a spin-coater [50]. If the rotational speed is high enough, large monolayers regions can be created without 'coffee stain' effects. It is the only monolayer deposition techniques which is able to produce a quasi-stable square distribution of nanospheres as well as the normal hexagonal, honeycomb distribution. However, it can be difficult to coat large samples at high rotation speeds and inevitably a large proportion of the colloidal solution is wasted during the coating process.

The Langmuir-Schaefer and the Langmuir-Blodgett techniques are both closely related [102]. They exploit the confinement and formation of monolayers at the high surface-tension interface between air and water. Colloidal suspensions are carefully added to the surface of a water trough (the 'subphase'). The nanospheres which remain on the surface have a high mobility and nucleate (or are compressed) to form large, high-density floating monolayers. The Langmuir-Schaefer technique involves the transferal of the floating monolayer to a flat substrate via a *horizontal* dipping method, whereas, the substrate is *vertically* passed through the interface during Langmuir-Blodgett deposition. The advantage of these methods is that the formation and transferal of the monolayer can be carefully controlled and only a small portion of colloidal solution wasted.

Chapter 2

Context: smarter windows

2.1 The evolution of glass technology

Humankind has been captivated by glass for millennia, to this day techniques for its improvement continue to evolve. It is a material that can be moulded, formed, blown, plated or sintered. Decorative Egyptian glass beads, mimicking gemstones, are the earliest examples of glass production and date back to approximately 16th century BC [103–106]; over the following century glass-working techniques developed such that larger objects could be formed. By the 1st century BC Roman glass-blowing methods had been exported throughout their European empire and were used to create luxury objects and, in some special cases, glass windows [107, 108].

Optically transparent glass (used for spectacles) appears in portraiture dating back to the 13th century AD. Glass, as a window material, became common in England in the early 17th century. It replaced flattened animal-horn as a means to allow daylight to enter a dwelling without exposing the inhabitants to the external environment and convective thermal-loss. Around this time the optical quality of glass had matured to a point that facilitated Newton's prism and lens work and many other telescopic and microscopic investigations. The mid-18th century industrial revolution provided a strong stimulus for the development of large, transparent and cheap windows. Today, glass holds a position as both a luxury material and a basic commodity.

The continued development of glass fabrication techniques has always been driven by the desire to: (a) make the material easier to work with and shape; (b) improve the materials transparency (or in special cases its tint/colour); (c) make it more robust [109]. It is generally acknowledged that glass production techniques were improved upon empirically until the 19th century, at which time better understanding of the material's chemistry began to inform production methods. Prior to the 19th century developments 'crown glass', first produced in London, dominated. The first example of modern 'float glass' was demonstrated in 1843 by Henry Bessemer by pouring molten glass on to liquid tin. It took a century for the process to be improved upon and made a commercial success by Alastair Pilkington in 1959.

Polymeric glass, rapidly developed in the mid-20th century (for military purposes), has not yet transitioned to common architecture (windows for buildings) as a replacement for float glass. This type of glass is commonly used in small optical components such as

sunglasses due to its favourable mechanical properties [110]. One reason polymeric glass may not be expected to replace conventional glass materials in architecture and automotive applications, is its comparatively short lifetime, particularly under high intensity ultra-violet (UV) irradiation.

2.2 Fenestration in modern architecture

In addition to the improvements of the glass material, architectural glazing schema have undergone several key advances in the last century. These developments have been primarily focused upon plugging thermal-energy leakage through window elements in order to reduce energy consumption in buildings. Multiple glazing, and the development of 'low-emissivity' (low-e) glass, have enabled windows to become much more efficient conductive and radiative thermal insulators.

2.2.1 Insulated glass units

Insulated glass units (double/triple glazing) are now commonplace. These units are created by filling the cavity between glass panes with a noble gas such as Argon or Krypton. These gases are denser air but reduce the amount of heat transfer through the window as their thermal conductivity is low. When 90% Argon gas-fill is used in a multiple glazing unit, instead of air, a window's insulating value can be improved by up to 16%. Krypton can improve the insulating value in a low-e insulated glass unit by up to 27% [111, 112]. However, Krypton gas costs significantly more than Argon which introduces a trade-off. Economy insulated glass units are typically Argon-filled and thick as conduction falls off rapidly as the spacing between the glass units increases [113].

The key challenge for insulated glass units is gas leakage. The partial pressure differentials between atmosphere and the insulating gas cause both Argon and Krypton to naturally escape. The highest grade insulated glass units leak their gas at a rate of about 1% volume per year; for poorly constructed units the rate is much higher. Since air is unable to backfill into the unit, the glass panes begin to collapse into the centre of the unit. This can cause the glass to look distorted or, in some cases, to break.

2.2.2 Low-emissivity glazing

'Emittance' is a measure of how much thermal energy from a room-temperature blackbody source is radiatively transmitted through a window. Low-e windows are already widely in use, whereby a thin metal-oxide, such as F:SnO_2 (30-160 nm in thickness), is applied to an internal surface of a double-glazed unit [114, 115]. The methods by which emittance is defined and assessed are discussed in further depth in section 4.6 on page 64.

These films are spectrally selective; transmissive to the short wavelengths of visible light and the near-infrared solar-spectrum whilst remaining highly reflective to long-wavelength mid-infrared radiation from thermal blackbody sources at domestic temperatures [116]. The effect is to keep radiant, room-temperature heat on the same side of the window from which it originated. Performance of metallic low-e coatings is often improved by incorporating dielectric anti-reflection layers tuned towards the visible and near-infrared in a dielectric/metal/dielectric configuration [114, 117]. The deployment of low-e coatings on

the internal surface of insulated glass units protects the film from chemical and physical degradation, see fig. 1 on page 18.

The primary disadvantage of low-e glass is an enhanced greenhouse effect during hot weather. Visible and near-infrared radiation from direct-sunlight is converted into heat after being transmitted into an isolated indoor environment. Cooling via radiant heat-loss is limited by the low-e window film which reflects it back into the building causing internal temperatures to soar. Therefore, it is commonplace to see energy-intensive air-conditioning systems used to moderate internal temperatures on sunny days which counterbalances any energy-saving from the use of a low-e coating in cold weather.

2.3 Smart windows: a dynamic greenhouse-effect

Large quantities of solar-energy are incident upon buildings daily. If this energy enters the building via transmission through a window it can lead to a significant greenhouse heating effect, as described above. This is amplified in modern architecture where the ratio of window-area to room-volume is high. Conventional approaches toward counteracting this greenhouse effect with air-conditioning systems in hot weather is energy-intensive and can be self-defeating if it results in the formation of an 'urban heat-island' (as previously discussed). However, in some locations or seasons this greenhouse effect is an advantage as it provides the building with a zero-cost heat source during cold weather.

Smart-windows, the next evolution of window technology, harness the greenhouse heating effect when a building is below a comfortable temperature and limit solar-heating effects when the internal temperature is too high. Smart-windows are best thought of as controlled 'energy gates' for which transmittance is dictated by ambient temperature.

The architectural incorporation of windows that dynamically switch their transmittance characteristics, depending upon the ambient temperature, has generated interest for several decades. The role of these windows is to modulate the solar thermal energy entering a building by switching between 'hot' and 'cold' states. In its cold state an ideal smart-window transmits a large portion of the visible and the infrared spectrum, thus maximising heat gain. In its hot state, transmittance is limited and this contributes to a cooling effect.

Distinct approaches toward implementing smart-glazing have been developed and can be differentiated in several ways.

Active/passive 'Active' systems use digital sensors to detect the ambient temperature and switch between hot and cold states using control circuitry accordingly. 'Passive' systems switch between their hot and cold states intrinsically. Unsurprisingly, active systems are more complex and potentially expensive. However, they carry the advantage that conditional switching rules can be used to determine the optimum time at which to change states.

Transparency Another mode of comparison between smart-window systems is whether or not visible transmission is maintained in both hot and cold states. Many systems are not 'consistently transparent' and will block or scatter visible light in their hot state i.e. during hot periods visual contact between the internal and external environments may be lost.

Consistently transparent systems have an appearance much closer to a conventional window which allows them to be utilised as normal windows in existing architectural scenarios. *In*consistently transparent systems, introduce additional complexity as an adaptive lighting system may be required to compensate for blocked sunlight during its hot state. This mode of operation (losing transparency in the hot state) leads to higher solar energy modulation capabilities and can lead to consistently-transparent systems being overlooked. We would argue that care needs to be taken in this respect as losing transparency in the hot state may compromise the window's primary function.

The disadvantage of 'consistent transparency' is that it sets a 60% limit on the solar-energy transmission-modulation (see fig. 4.3 on page 58). This is an idealised value, and much higher than could be expected for a real smart-window system. It assumes perfect blocking of infrared wavelengths ($\lambda \geq 650\,\text{nm}$) in the hot state and full-transmission of visible and infrared wavelengths in the cold state. An ideal 'selective wavelength' of 650 nm is used in this calculation as it would leave 98.6% of visible light unaffected by the thermochromic switch (see fig. 4.1 on page 56, page 56).

The mode of operation for each system will have implications for its cost, aesthetics and energy efficiency. Further discussion of competing dynamic window systems is available in our review in appendix C on page 123. The key hurdles toward the commercialisation of smart-window technology remain performance, cost and durability.

Chapter 3

Material focus: vanadium dioxide

3.1 Thermochromism

Since the middle of the twentieth-century the metal-to-insulator phase transition in binary transition-metal oxides has been an active area of research. Morin was the first to report that the resistivity of several vanadium oxides (VO_2, V_2O_3, VO) and a titanium oxide (Ti_2O_2) changed abruptly as a function of temperature — impressively, five-orders-of-magnitude in the case of single-crystal vanadium dioxide (VO_2) [118]. Other correlated oxides have been shown to make similar temperature-mediated transitions, albeit at different characteristic metal-to-insulator critical temperatures (τ_c). These materials are termed 'thermochromic' and are shown ordered with respect to their τ_c in fig. 3.1. Thermochromic materials form a subset of the larger 'chromogenic' materials group: materials that change their optical properties in response to an external stimuli (e.g. electrical or magnetic field strength, presence of certain gas molecules or mechanical pressure/strain) [119, 120].

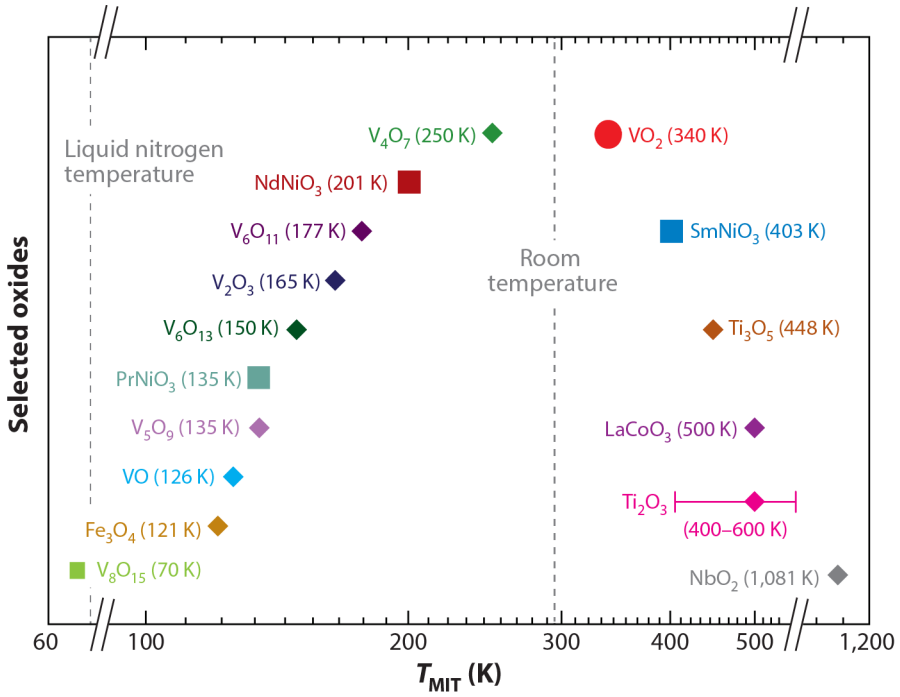

Figure 3.1: The critical metal-to-insulator transition temperatures (τ_c) for selected 'thermochromic' oxide materials (bulk crystals). Reproduced from [121].

3.2 Vanadium dioxide for window applications

It was a decade later that vanadium dioxide (VO_2) began to commanded attention as a potential material for use in temperature-responsive smart-windows [122, 123]. The reasons for this are twofold. Firstly, the MIT occurs close to room temperature and can be tuned through a variety of doping schema. Secondly, the resistivity change that occurs between its cold state and hot state is accompanied by a change in refractive index with a well-located 'switching-edge' close to $\lambda = 650\,\text{nm}$ (see section 4.3 on page 61 for more information on the ideal location for the switching-edge).

In its cold state, vanadium dioxide responds like a semiconductor with a high refractive index, see fig. 3.2. Absorption occurs as electrons are promoted from the valence- to conduction-band. However, in its hot state it becomes 'semi-metallic' as the material's Fermi-level sits within a conduction band; its extinction coefficient dominates the near-infrared wavelengths but remains largely un-changed in the visible region. The combined optical properties of these two states facilitate a self-stabilising smart-window (with no requirement for control circuitry) capable of modulating solar thermal (near-infrared) energy transmittance whilst maintaining constant visible transmittance.

It should be mentioned that VO_2's MIT occurs extremely fast, in the order of picoseconds to femtoseconds. However, for window applications this speed is limited by the heat capacity of the glass substrate.

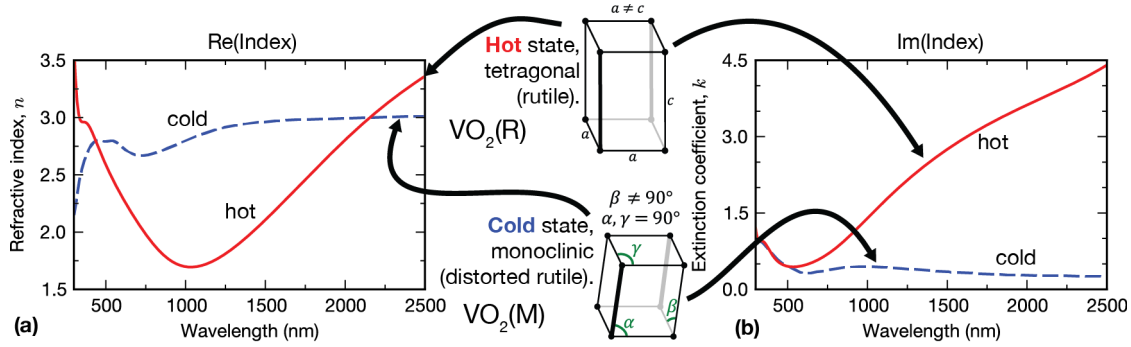

Figure 3.2: The structurally-induced change in the complex refractive index, VO_2(M) to VO_2(R). Data extracted from [124].

3.3 Crystalline structure

The crystal structure of vanadium dioxide undergoes a fully-reverseable transition between its hot and cold states. In its hot state, the crystal exhibits a tetragonal (rutile) formation. However, in its cold state, the structure becomes monoclinic (distorted rutile) as dimerization and twisting between neighbouring vanadium atoms causes compressive strain on the c-axis [125, 115], see fig. 3.3 on the next page. This change in crystal structure also brings with it a small (0.044%) volumetric change in the bulk material [126].

There are several schools of thought with regards to the relationship between vanadium dioxide's crystal and electronic structure and what causes the transition between its two phases.

The Mott-Hubbard model ascribes the metal-to-insulator transition effect to strong

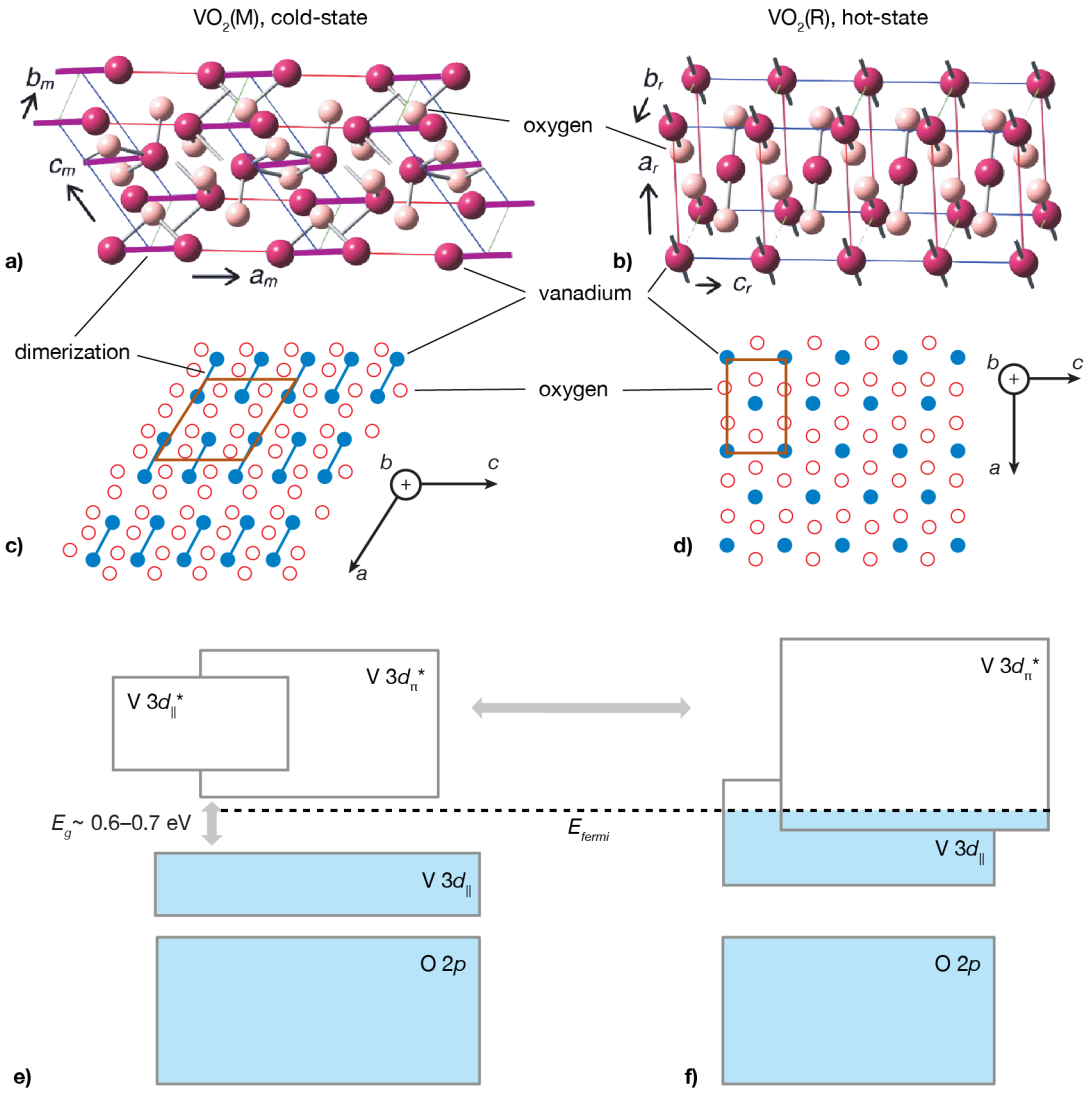

Figure 3.3: The crystal and band structure of vanadium dioxide in both its cold state (left-hand side) and hot state (right-hand side). The cross-section shown in subfigures (**b**) and (**d**) clearly show the high-temperature tetragonal-rutile structure. Subfigures (**a**) and (**c**) exhibit the low-temperature monoclinic structure (distorted-rutile) due to dimerization between neighbouring vanadium atoms. Figures adapted from [127, 121, 128–130].

electron-electron interactions ('correlation') within the material. It describes a critical carrier density, n_c, above which a phase transition occurs,

$$n_c \approx \left(\frac{0.25}{a_H}\right)^3 \tag{3.1}$$

where $a_H = 1.77\,\text{nm}$ is the Bohr-radius of VO_2 [131]. Thereby the structural transformation is 'coerced' by the temperature-induced change of the material's electronic properties [126].

An alternative description is provided by the Peierls model which places the key-emphasis on electron-*phonon* interactions. In this scenario, the strained monoclinic crystal deforms into a rutile form as the temperature increases which alters the ionic potential within the material. This structural change modifies the periodic ionic-potential; giving rise to an altered electronic band structure [121].

Our primary focus is upon the optical manifestation of vanadium dioxide's electronic properties: its complex refractive index. This topic is has formed a popular battleground but the exact cause for the change in phase, be it Mott-like or Peierls-like, is of little consequence for its deployment in smart-window applications [132–136].

3.4 Metal-ion doping

A key feature of vanadium dioxide is its susceptibility to doping. The practice of substituting a few percent of the V^{4+} cations for equivalent or higher-valence cations (e.g. W^{6+}, Mo^{6+}, Ta^{5+}, Nb^{5+} or or Ru^{4+}) is known to reduce the metal-to-insulator critical transition-temperature, τ_c [137–139, 129]. For example, it has been shown that in order to tune-down the transition-temperature from its pure-bulk value, $\tau_c = 68°C$, to room-temperature it is sufficient to dope the material at 7 at.% with Mo or at 3 at.% with W [140]. On the other hand, doping with lower-valence cations (such as Cr^{3+} and Fe^{3+}) *increases* the transition-temperature and therefore doing so is unfavourable for window applications. Tungsten-doping (W) is by-far the most popular τ_c-reducing doping method as it can reduce the phase-transition-temperature in a controlled manner to as low as $-23\,°C$ without significantly altering the material's optical properties [141, 142]. This allows for the deployment of VO_2-based smart-windows in a range of different domestic environments across the globe.

A metal-to-insulator transition exhibits a hysteresis whereby the rising critical-temperature is greater than the falling critical-temperature: $\tau_c^+ > \tau_c^-$. This hysteresis effect ($\Delta\tau = \tau_c^+ - \tau_c^-$) can be in the order of $\Delta\tau = 10$–$15\,°C$; minimising it significantly improves the energy performance of VO_2-based smart-windows [143, 144]. One of proposed methods to reduce $\Delta\tau$ is to use a Ti doping scheme [145, 146].

An independent stream of investigation has been directed toward improving the optical properties of VO_2 films by modifying the bulk refractive index. The most promising dopants for doing this are magnesium, Mg, and fluorine, F which widen the fundamental band gap in the VO_2 and blue-shift its absorption-edge [147, 148]. The major-drawback for fluorine-doped vanadium dioxide is that, as a low-valence cation, it is known to increase the metal-to-insulator transition temperature and can also widen the transition hysteresis [149].

Finally, it is useful to consider that doping-schema needn't be mutually-exclusive.

Multiple studies of co-doped VO_2 films have produced material-libraries from which an ideal-hybrid doping scheme can be chosen from [145, 150].

3.5 Synthesis techniques

Synthesis of monoclinic-phase vanadium dioxide has been demonstrated using a variety of techniques. However, achieving the correct oxide phase (VO_2(M)) is a common challenge as vanadium is polymorphic and vanadium *pent*oxide (V_2O_5) is the thermodynamically more stable form [151]. In addition, each deposition technique (along with its individual conditions), gives rise to VO_2 films with differing morphologies. Density, topography and phase-composition are key features in vanadium dioxide synthesis. It is critical that these three properties are well-controlled.

3.5.1 'Flat' coatings

DC and RF magnetron sputtering are common techniques used to produce VO_2 films [152, 153]. The method involves a vanadium target which is bombarded and ballistically-emits material which deposits on the nearby substrate — the process takes place under vacuum conditions. It is capable of producing high-density thin-films ($\sim 90\%$ of bulk) but is a physical vapour (line-of-sight) process which excludes it from use in conformally coating three-dimensional nanostructured substrates.

Pulsed Laser Deposition, another physical vapour method, has been used for the deposition of VO_2 thin-films [154]. The process is also performed under vacuum conditions and requires a vanadium target. It results in high-density films and has been used to produce continuously varied single- and double-doped vanadium dioxide 'material libraries' [155]. In a similar manner to the sputtering methods (above), this deposition technique would not be appropriate for coating motheye nanostructures due to its line-of-sight dependency.

Aerosol Assisted Chemical Vapour Deposition is perhaps the simplest of several surface reaction methods for depositing VO_2 thin-films [156–161]. A vanadium precursor is aerosolised and then fed into a heated furnace along with a co-reactant (typically water vapour). The two chemicals react on the surface of the substrate between 400 and 500 °C, producing films that are often 'powdery' in texture and polydisperse on the order of several hundred nanometres. The process can be performed on an industrial scale but unfortunately is not suitable for producing thin-coatings on motheye nanostructures.

Atmospheric Pressure Chemical Vapour Deposition is a thin-film deposition technique very commonly used for producing medium-to-high density VO_2 thin-films [142, 162–166]. It is compatible with industrial float glass production lines used by commercial glazing companies such as Pilkington/NSG and has therefore received a lot of attention. Vapour-phase vanadium-precursor and oxygen-donating co-reactant flow over the glass substrate at temperatures above 400 °C. A surface reaction occurs, producing vanadium dioxide thin-films with a variety of morphologies depending upon the deposition conditions. This technique can be used to conformally coat micron, and even nano-scale, features. However, its typically-high growth-rates can make *thin* coatings which cover high aspect-ratio features difficult to achieve [161, 139].

Atomic Layer Deposition has only recently been demonstrated as a viable method

for producing VO_2 thin-films [167, 168]. The technique is executed in discrete steps: first, dosing the substrate surface with a vanadium precursor; second, purging excess precursor material to leave only a monolayer on the substrate; third, dosing with an oxygen rich co-reactant until all surface reaction sites are filled; fourth, purging remaining co-reactant from the chamber. The sequence is repeated many times and builds up high-density, sub-nanometre layers. Since the technique is self-limiting it can be used to conformally coat high-aspect ratio nanostructures but would be inefficient if used to produce a thick ($> 100\,\text{nm}$) thin-film. The surface reaction occurs between 200 and 300 °C but can be reduced to plastic-compatible temperatures by striking a plasma in the reaction chamber [169].

3.5.2 Micro- and nano-structured films

Over recent years interest a lot of work has been put into purposely inducing micro- or nano-structure in VO_2 films. The majority of this is centred around manipulating the film's synthesis conditions; not on coating a *pre*-nanostructured substrate. However, the motivations underpinning growth-induced nanostructure are usually similar to those of the motheye surface: to improve the transmissive and/or thermochromic switching properties of the film or to promote hydrophobic self-cleaning.

The specific synthesis kinetics behind each of these methods are often bespoke and are therefore outside the realm of our current research. However, we will draw attention to two notable examples. Firstly, the synthesis of 'nanorods' and 'nanofibres' has been demonstrated many times over, including SiO_2 and TiO_2 core-shell structures [126, 170–172]. Secondly, the synthesis of 'pseudo-dendritic' shrub-like VO_2 microstructures produced via Electric Field Assisted Chemical Vapour Deposition shows much promise [173, 174]. The crystalline-range of these films have been shown to be inversely-proportional to the electric field strength, and interestingly, the morphologies it produces are bias-sensitive (the reverse fields produce spherical 30–40 nm island structures) [175].

3.6 Ultra-thin films

Ultra-thin ($\leq 10\,\text{nm}$) vanadium dioxide films exhibit noteable characteristics. The phase-transition-temperature is reduced by both geometric confinement [176] and strain [177, 156]. The reduction of τ_c as a function of thickness has been attributed to variation in the average VO_2 grain-size due to strong substrate binding and strain relaxation at the grain-substrate interface [178]. In support of this, it has been shown that variations in *substrate* microstructure can have an effect upon the deposited VO_2 grain-size and consequently its transition-temperature [179]. Therefore, ultra-thin films typically require lower doping concentrations in order to bring their phase-transition to an appropriate level. There is also some evidence to suggest that the width of the phase-transition hysteresis-loop bears relation to the film thickness. The premise is that strain relaxation upon nucleation leads to an increased hysteresis-loop for small grain-sizes [180].

The electron mean-free path in Nobel metals (such as gold) and transition metals (such as silver) is often tens of nanometres. If the film thickness for one of these metals approaches the length scale of the mean free path length the imaginary part of the material's

dielectric constant typically increases, leading to higher absorptance [181]. When this thickness-dependent absorptance effect occurs it is more pronounced at long wavelengths. However, the situation with regards to VO_2 is somewhat different. During its metallic phase the material's conductivity increases by several orders of magnitude to around $10^4\ \Omega^{-1}\mathrm{m}^{-1}$ [182]. However surprisingly, within VO_2 the electron mean-free-path is less than the inter-atomic spacing and therefore violates the Ioffe-Regel-Mott limit for resistivity [183, 184]. Studies have been conducted into the thickness dependence of the optical switching for ultra-thin VO_2 films [185, 186]. Thermochromic switching is observed at film thicknesses of 5 nm although the refractive indices of the films produced in these studies are not explicitly calculated. The transmittance switching-depth for these studies appears to correlate directly with the film thicknesses [185, 186]. Therefore, an absorptance-penalty for the ultra-thin vanadium dioxide films is not apparent (as would be expected *if* the film-thickness became less than the electron mean free path).

Chapter 4

Quantifying glazing states

Our motivation to define a principal set of metrics arises from the need for direct comparison between smart-window designs. In accordance with international standards (ISO 9050 and EN 410, [187, 188]) the critical energy performance characteristics of a window relate to both its visible and solar transmittance.

The metrics used to describe the transmittance characteristics for smart-window coatings vary throughout the academic literature. In some cases, transmittance (and its cold to-hot difference) are quoted for only a single wavelength — typically 2500 nm [142, 163, 189, 162, 159, 143]. However, in others [190–192, 124, 115] the transmittance spectra are weighted by a secondary function, such as the solar spectrum or response of the human eye, and then integrated to produce a single, broadband metric.

4.1 Spectrum weighted metrics for interfaces

In the following equations transmittance is our primary concern. However, equivalent metrics for reflectance and absorptance are reached through the substitution of T^{σ} with either R^{σ} or A^{σ} (σ represents the temperature-state, 'hot' or 'cold').

4.1.1 Response of the human eye

In order to quantify the amount of visible-light useful for daytime human vision under normal conditions we define the photopically-averaged visible transmittance in the hot state,

$$T_{\text{vis}}^{\text{hot}} = \frac{\int_{\lambda=350\,\text{nm}}^{780\,\text{nm}} \bar{y}(\lambda) \cdot T^{\text{hot}}(\lambda)\, d\lambda}{\int_{\lambda=350\,\text{nm}}^{780\,\text{nm}} \bar{y}(\lambda)\, d\lambda} \tag{4.1}$$

and in the cold state,

$$T_{\text{vis}}^{\text{cold}} = \frac{\int_{\lambda=350\,\text{nm}}^{780\,\text{nm}} \bar{y}(\lambda) \cdot T^{\text{cold}}(\lambda)\, d\lambda}{\int_{\lambda=350\,\text{nm}}^{780\,\text{nm}} \bar{y}(\lambda)\, d\lambda} \tag{4.2}$$

where $\bar{y}(\lambda)$ is the CIE photopic luminous efficiency of the human eye and is used as the weighting functions for the wavelength-dependent transmittance coefficients, see fig. 4.1 on the following page. An alternative weighting function, the 'scotopic' efficiency, would be used under low-light conditions. However, for daytime applications, the 'photopic' efficiency is most appropriate. The wavelength range used for our photopically averaged calculations, $350\,\text{nm} \leq \lambda \leq 780\,\text{nm}$, corresponds to the absolute limits of human vision (see fig. 4.1 on

the next page).

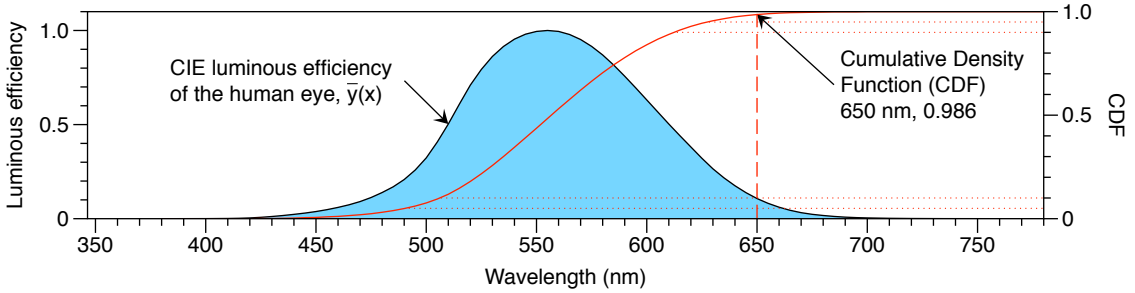

Figure 4.1: The photopic luminous efficiency of the human eye, $\bar{y}(\lambda)$, used to weight the transmittance functions in eqs. (4.1) to (4.2) on page 55. The data is sourced from [193]. The Cumulative Density Function shows that if the thermochromic transmission-selectivity of a smart window occurred at 650 nm then 98.6% of visible light would be unaffected.

Equations (4.1) to (4.2) on page 55 are normalised by their denominators and subsequently take values between zero and unity corresponding to no transmittance ($T_{\text{vis}} = 0$) and full transmittance ($T_{\text{vis}} = 1$).

The window's hot state dimming is quantified as ΔT_{vis},

$$\Delta T_{\text{vis}} = T_{\text{vis}}^{\text{cold}} - T_{\text{vis}}^{\text{hot}} \tag{4.3}$$

Since our human understanding of 'dimming' is relative, variations between low T_{vis} values are more significant than variations in high T_{vis} values [194]. If a dimming effect were to be of importance in a thermochromic smart-window system it may be more appropriate to quantify dimming as:

$$\Delta^{*} T_{\text{vis}} = \frac{T_{\text{vis}}^{\text{cold}} - T_{\text{vis}}^{\text{hot}}}{T_{\text{vis}}^{\text{cold}}} \tag{4.4}$$

Although dimming of specular transmission is not a requirement, it may be desirable in some environments; for example, in order to reduce direct glare from the sun at peak solar activity. On the other hand, if a large thermochromic window were to contain areas in different states a large ΔT_{vis} may give a 'dirty' or 'patchy' appearance [195]. As the merits of a high or low $T_{\text{vis}}^{\text{hot}}$ and ΔT_{vis} are unclear, our discussions from this point onward are centred around the cold-state visible transmittance value only, $T_{\text{vis}}^{\text{cold}}$.

4.1.2 Colour calculations

The 'greenish-brown' tint of flat, undoped VO_2 thin-films is commonly regarded as a barrier against bringing this type of smart-window to the market. The structural properties of a thin-film affect its perceived colour; therefor, predicting the colour of a smart-window interface prior to its fabrication is valuable. It is possible to counteract undesirable colours by tuning the optical resonance within a single layer, adding additional resonant interlayers or compensate by adding an absorbing layer, see for example fig. 7.1 on page 83. However, only by performing the following calculations can a compensatory coloured-film be specified.

We use the Commission Internationale de l'Eclairage's (CIE) 1931 standard observer colour matching functions to obtain the window's tint based upon its transmittance spectrum [193]. This provides a qualitative description of transmittance and is helpful for

understanding a smart-window's aesthetic properties. Within our colorimetric calculations the CIE Standard Illuminant D65 defines the white point as a representative daylight illuminant against which the transmittance spectra are normalised [196]. Displayable iRGB colour hex-strings are extracted from the XYZ tristimulus values using standard functions. Our calculations of the colour code assume display chromaticities and physical gamma components as defined in the sRGB standard.

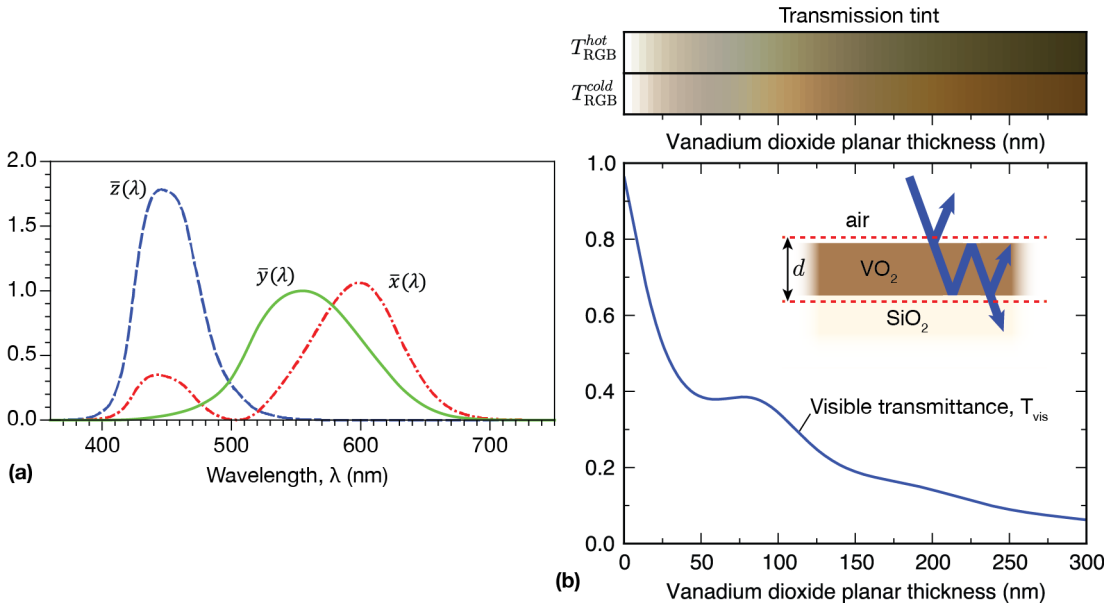

Figure 4.2: Transmission 'tint' colour calculations. Subfigure (**a**) shows the CIE tristimulus response functions for the human eye used to calculate the perceived transmission colour: $\bar{x}$, $\bar{y}$ and $\bar{z}$. Subfigure (**b**) shows the transmission tint as calculated for a thin VO_2 film on glass. The colour bars along the top of (**b**) show the difference between the hot and cold state transmittance tint (T_{RGB}) to be low. It is evident that the visible transmittance value, T_{vis}, becomes unacceptably dark for VO_2 coatings with thicknesses greater than 100 nm.

4.1.3 Solar irradiance

In order to quantify the amount of solar thermal energy entering a building we define the solar-averaged transmittance in the hot state as,

$$T_{\mathrm{sol}}^{\mathrm{hot}} = \frac{\int_{\lambda=300\,\mathrm{nm}}^{2500\,\mathrm{nm}} \mathrm{AM}_{1.5}(\lambda)\cdot T^{\mathrm{hot}}(\lambda)\,d\lambda}{\int_{\lambda=300\,\mathrm{nm}}^{2500\,\mathrm{nm}} \mathrm{AM}_{1.5}(\lambda)\,d\lambda} \tag{4.5}$$

and in the cold state as,

$$T_{\mathrm{sol}}^{\mathrm{cold}} = \frac{\int_{\lambda=300\,\mathrm{nm}}^{2500\,\mathrm{nm}} \mathrm{AM}_{1.5}(\lambda)\cdot T^{\mathrm{cold}}(\lambda)\,d\lambda}{\int_{\lambda=300\,\mathrm{nm}}^{2500\,\mathrm{nm}} \mathrm{AM}_{1.5}(\lambda)\,d\lambda} \tag{4.6}$$

where the $\mathrm{AM}_{1.5}$ irradiance spectrum is chosen for our solar averaged transmittance calculations as it represents an overall yearly average for mid-latitudes including diffuse light from the ground and sky on a south facing surface tilted 37° from horizontal [197].

Solar Energy Transmittance Modulation, ΔT_{sol}, is defined as,

$$\Delta T_{\mathrm{sol}} = T_{\mathrm{sol}}^{\mathrm{cold}} - T_{\mathrm{sol}}^{\mathrm{hot}} \tag{4.7}$$

With regards to the desirable level of ΔT_{sol}, there is a direct relationship between the solar transmittance modulation and the energy saving potential of a smart-window. It is perhaps the single most important metric for a smart-window system. It has been shown that if ΔT_{sol} is maximised, and the hot to cold state transition-temperature is suitably low, a VO_2-based thermochromic window could improve the energy consumption of a building in hot and sunny environment by almost 50% [198].

The wavelength range used for all of our solar-thermal calculations is $300\,\text{nm} \leq \lambda \leq 2500\,\text{nm}$ which accounts for 99.2% of terrestrial solar-energy. However, integration limits used for similar solar transmittance calculations in the academic literature can vary, in particular the lower limit; $\lambda_{\text{min}} = 250\,\text{nm}$ and $\lambda_{\text{min}} = 350\,\text{nm}$ are both common. Although only 1.39% of solar-energy exists with $\lambda \leq 350\,\text{nm}$, it is important to make this observation as any change in the integration limits of eqs. (4.5) to (4.6) on page 57 will affect ΔT_{sol}.

We use $\lambda_{\text{min}} = 300\,\text{nm}$ as our fabrication process (described in upcoming chapters) is centred around quartz substrates which are know to have a transmission cut-off, $T_{\text{cut-off}} \leq 300\,\text{nm}$ (and in the case of fused-quartz, $T_{\text{cut-off}} \approx 200\,\text{nm}$). Some argue that using $\lambda_{\text{min}} = 350\,\text{nm}$ as an integration limit may be preferable as this coincides with sharp cut-off in transmittance through float glass, see fig. 4.4 on the next page. In practice, our adoption of $\lambda_{\text{min}} = 300\,\text{nm}$ as an integration limit results in a *lower* calculated ΔT_{sol} values than methods which use $\lambda_{\text{min}} = 350\,\text{nm}$ as $\Delta T_{300<\lambda<350\,\text{nm}}$ is generally much lower than $\Delta T_{\lambda>700\,\text{nm}}$. Whichever limits are chosen, the principle requirement in the comparison of smart window performance metrics is internal consistency; this is maintained throughout the presented work.

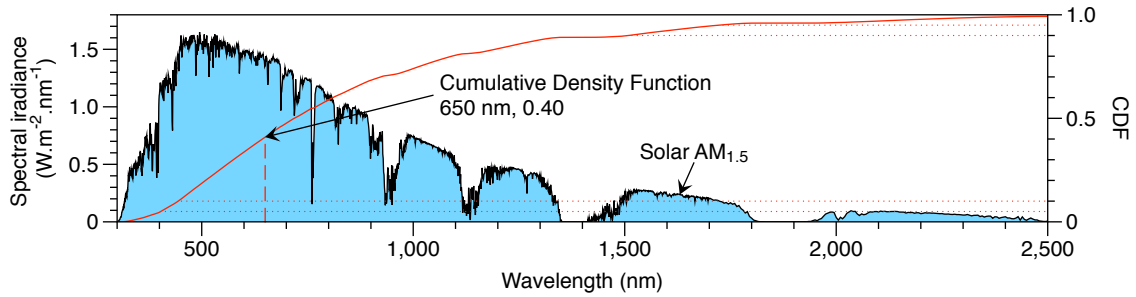

Figure 4.3: The solar $AM_{1.5}$ irradiance spectrum used to weight the transmittance function in eqs. (4.5) to (4.6) on page 57. The data is sourced from [197]. The Cumulative Density Function shows that if the thermochromic transmission-selectivity of a smart window occurred at 650 nm then 60% of solar energy would be affected, indicating a ΔT_{sol} limit.

4.1.4 'Interface' to 'system' conversion

What unites academic smart-window metrics is that, more often than not, the measure (e.g. transmittance) is reported for an *interface* (e.g. air–VO_2–glass). This is in contrast to industrial metrics which report transmittance as a property of an entire window *system* (e.g. a pane of glass or a complete double-glazed unit), see section 4.4 on page 62. However, conversion from an 'academic' (interface) metric to an 'industrial' (system) metric can be reasonably straight-forward. For example, an interface transmittance spectra can be altered to account for absorption within float glass and reflection losses at an additional air–glass interface using the lower panel of fig. 4.4 on the next page.

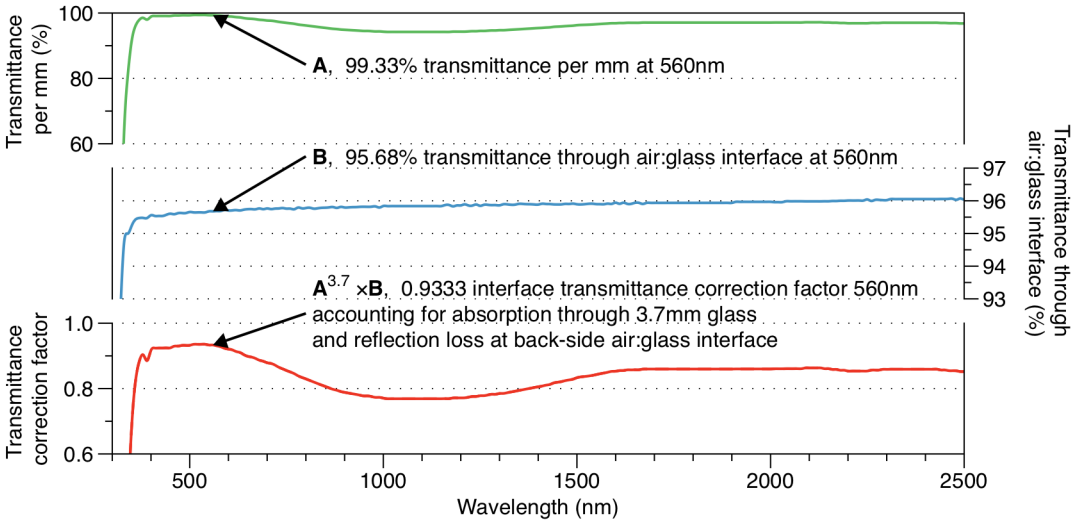

Figure 4.4: Correction factors used to convert from an interface (e.g. air–VO_2–glass) transmittance spectra to a system transmittance spectra (e.g. air–VO_2–glass-air). The substrate is assumed to be Pilkington float glass with a thickness of 3.7mm. Multiple reflections have not been taken into consideration.

4.2 Visual representations of smart-window systems

It is helpful to have a visual tool when: (a) making a comparison between competing smart-window systems; (b) when choosing the optimum parameters for a smart-window design.

In our first publication [19] we used heat-maps to pick-out the best parameter sets for motheye smart window systems (see fig. 4.5 on the following page). We were able to show variations in T_{vis} and ΔT_{sol} but the optimum trade-off of VO_2 thickness and motheye height was hard to decipher. At that point our method for comparison between competing smart-window systems was to tabulate and compare the transmission metrics. This was cumbersome, particularly difficult with large data-sets, and provided only limited modes of comparison.

4.2.1 Scatter and locus representation

We have adopted a method for representing, and making comparisons between, competing smart-window systems that has become popular within the field during the past few years. The method employs a T_{vis} vs. ΔT_{sol} scatter plot, see fig. 4.6 on the next page. It represents each system (in both its hot and cold state) as a unique point. The method inevitably discards a lot of information, however, it makes the process of identifying high-performing systems simple (they sit toward the top-right of the graph).

The choice of T_{vis} along the x-axis and ΔT_{sol} along the y-axis are carefully-considered. A system's energy-saving potential is arguably proportional to its solar-transmittance dynamics, ΔT_{sol} (y-axis). Therefore, it is suggested that smart window systems which occupy the top of the plot are best suited to reducing a building's heating/cooling load. Visible transmittance, T_{vis} (x-axis), contributes toward the 'performance' of a smart-window in two separate ways. Firstly, it indicates how intrusive the window coating is and some applications may dictate a functional lower-bound. Secondly, high visible-transmittance

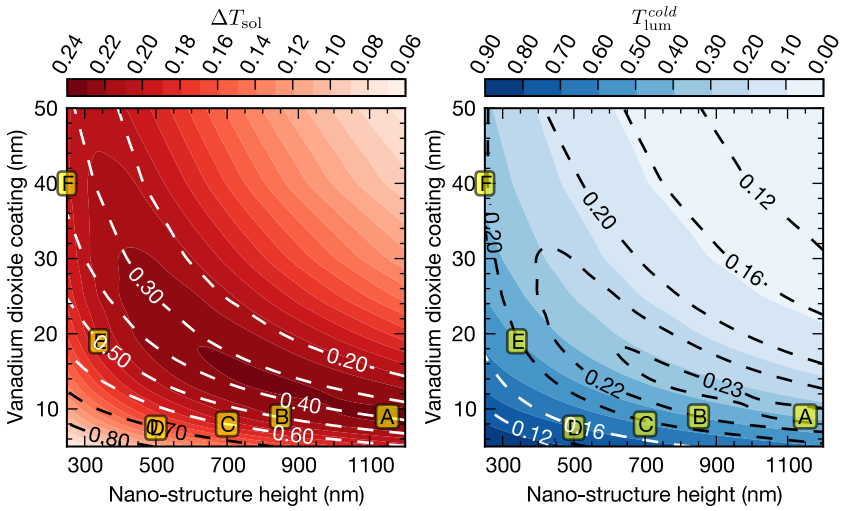

Figure 4.5: Representing T_{vis} and ΔT_{sol} in the *height* and *coating thickness* parameter space using heat-maps. We used this method in our first publication to select six cases (A-F) of high-performing motheye smart window geometries [19]. This method has been superseded by our scatter approach, fig. 4.6.

reduces the requirement for compensatory indoor lighting and can therefore lead to a reduction in a building's electrical load.

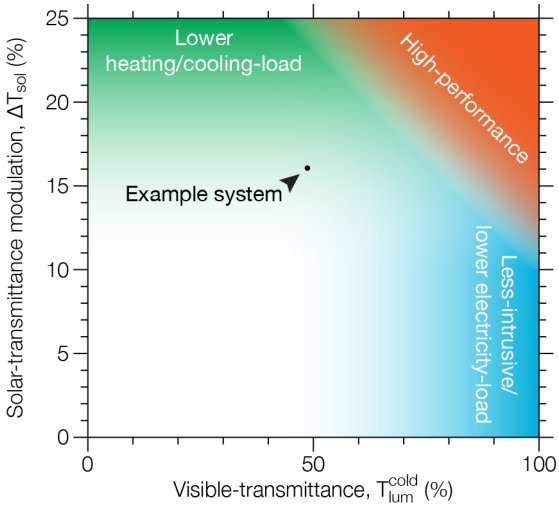

Figure 4.6: The T_{vis} vs. ΔT_{sol} scatter/locus representation for smart-window systems. The upper-right corner represents the high-performance region which we wish to access.

A third mode of comparison could be incorporated into these plots: the colour of each point. Although we do not currently implement this, it may be a helpful means by which to differentiate if clusters of window-systems fell within the same area. For example, the colour of each point could represent the transmission colour for the window in its cold state (see section 4.1.2 on page 56).

Finally, the method of comparing between smart-window systems using a single graphic enables 'performance boundaries' to be defined. The boundary-approach is novel and we believe it is particularly valuable when comparing between *classes* of thermochromic smart-windows. Our method of using the plot to extract the parameters of the highest-performing geometries for smart windows involves: firstly, performing a parameter search of all possible geometries; secondly, isolating the boundary points; and thirdly, plotting

each parameter for the boundary points in an aligned-axis. This is demonstrated fully in fig. 7.8 on page 90.

4.3 Transmittance switching-edge

The wavelength at which differences between hot and cold state transmittance occurs can be referred to as the *switching-edge*. In energy modelling publications it is often assumed that an 'ideal' transmittance spectra exhibits a switching-edge at $\lambda = 700\,\text{nm}$, see fig. 4.7. However, there is limited discussion as why this value is chosen and how its choice may affect the performance of a smart-window [199].

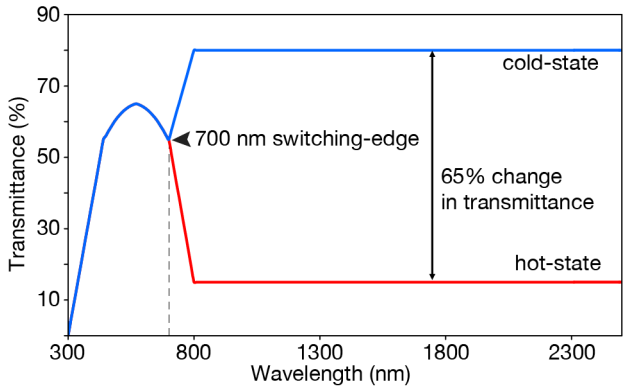

Figure 4.7: Example of an idealised transmittance spectrum for a VO_2 smart window; the switching-edge occurs at $\lambda = 700\,\text{nm}$. Figure adapted from [199].

Using the cumulative density functions (CDF) for both the solar spectrum and photopic efficiency of the human eye, it can be seen that the switching-edge can have an impact upon the performance of a smart-window and should therefore be carefully considered. A switching-edge at $\lambda = 650\,\text{nm}$ would allow 60% of the solar spectrum to be modulated with almost no affect upon visible transmittance. Whereas, a switching-edges that occur at shorter wavelengths, $\lambda = 560\,\text{nm}$ for example, facilitates more solar energy transmittance modulation (75% in this case) but would in turn also modulate the transmittance of visible light by 50%. Performing these calculations provides us with the insight that practical upper-limits exist for ΔT_{sol} i.e. 60–75%. And that achieving anything higher than this would significantly degrade the principal operation of a window: a visibly-transparent building element.

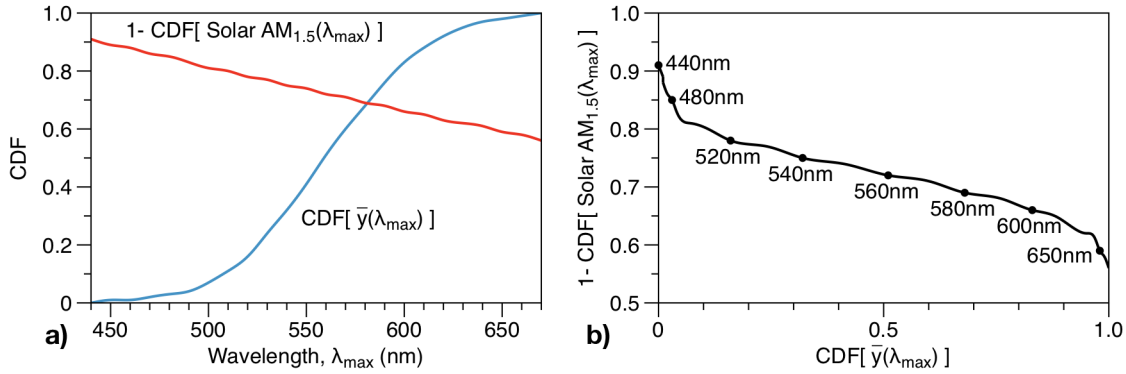

Figure 4.8: The affect of the switching-edge upon the performance of an ideal VO_2 smart-window. Subfigure (**a**) shows the cumulative density functions (CDFs) for both the luminous efficiency of the human eye ($\bar{y}$ from fig. 4.1 on page 56) and the solar spectrum (from fig. 4.3 on page 58). This data is re-plotted as a single series in subfigure (**b**) which shows that a switching-edge at $\lambda = 650\,\text{nm}$ would allow 60% of the solar spectrum to be modulated without *any* affect upon visible transmittance. Switching-edges that occur at shorter wavelength, $\lambda = 560\,\text{nm}$ for example, allow 75% of solar energy to be modulated but *also* modulate the transmission of visible light by 50%.

4.4 Industrial metrics for window systems

Several industrially recognised metrics exist for the quantification a window's energy impact, these include: 'Visible Light Transmittance', 'G-value' and 'U-value' [200]. As noted previously, a distinction can made between academic and industrial metrics. Academic metrics are almost always reported for a single interface, air-to-glass, and do not take into account system-level attributes of the window, whereas, industrial metrics account for sheets of glass (two interfaces), insulating gaps between panes and in some cases (such as Air Leakage and Condensation Resistance) the window's frame. In some cases, such as 'Visible Light Transmittance', the industrial calculation methods are very similar to their academic analogues. We will dedicate some attention to the principal industrial quantifications as they form a series of common benchmarks by which the energy characteristics of windows can be judged.

4.4.1 U-value

The most commonly quoted industrial energy-metric for windows is their 'U-value': the rate of heat transfer measured in Watts per square meter per degree Kelvin temperature difference ($\frac{W}{m^2 \cdot K}$) [201]. This is the reciprocal of the window's thermal resistance 'R-value', R: heat transfer per unit-area per unit-time ($\frac{m^2 \cdot K}{W}$) which is approximated to be independent of temperature. A window's U-value, U, is related to its thermal conductance, K ($\frac{W}{m \cdot K}$), by,

$$U = \frac{1}{R} = \frac{K}{L} \tag{4.8}$$

where L is the thickness of the glass unit. For multiple glazing systems the R-values are summed thereby giving,

$$U_{\text{total}} = \frac{1}{R_{\text{total}}} = \frac{1}{R_{\text{glass}} + R_{\text{gas}} + R_{\text{glass}}} \tag{4.9}$$

The U-value for a window ($U \approx 5.8$ for single glazing) is decreased by the use of low-e coatings, which can bring the value closer to 1.5. This demonstrates that a window's U-value accounts for not only thermal conductance but also *radiant transmission* (for room temperature blackbody sources). The convention for calculating a windows U-value are complex, particularly when ventilated and unventilated elements are present or if the window is inclined. A complete definition can be found in *BR 443: Conventions for U-value calculations* (2006).

4.4.2 G-value

'G-value' (also referred to as 'Window Solar Factor', 'Solar Heat Gain Coefficient' or 'Total Energy Transmittance') is equivalent to our solar-weighted transmittance definition, T_{sol}. Slight differences between G-value and Solar Heat Gain Coefficient arise from their use of different air-mass solar spectra. This industrial metric differs from the academic equivalent as it not only accounts for solar energy transmitted directly through the window but also energy that is absorbed and subsequently convected or re-radiated into the building [202]. G-value has superseded 'Shading Coefficient', a historical metric that compared the solar transmittance of a test window to transmission through 3 mm of clear sheet glass.

4.4.3 Light to Solar Gain

The glass manufacturers PPG combine 'Visible Light Transmittance' and 'Solar Heat Gain Coefficient' into a quick-reference metric 'Light to Solar Gain'.

$$\text{Light to Solar Gain} = \frac{\text{Visible Light Transmittance}}{\text{Solar Heat Gain Coefficient}} \tag{4.10}$$

A high 'Light to Solar Gain' value indicates a room will be bright without inducing excessive solar-heating. This is an interesting metric as it is scales well with window-area. An equivalent academic metric, $G_{\text{V/S}}$, could take the following form,

$$G_{\text{V/S}} = \frac{T_{\text{vis}}}{T_{\text{sol}}} \tag{4.11}$$

leading to scatter analysis of $G^{\text{hot}}_{\text{V/S}}$ vs $G^{\text{cold}}_{\text{V/S}}$ (similar to that described in section 4.2.1 on page 59).

4.4.4 Damage Weighted Transmittance

'Damage Weighted Transmittance' is an acknowledgement of the degradation to furnishings caused by UV light [203]. The metric weights transmittance of short-wavelength light by the CIE 'Damage Factor' and is helpful in predicting fading effects, see subfigure (**a**) in fig. 4.9 on the following page. The damage response curve for furniture-colour follows a similar shape to the skin-damage (sunburn) response curves shown in subfigure (**b**).

4.5 Legal and industrial guidelines

Legal guidelines exist for the minimum visible light transmittance through automotive wind shields; in parts of the United States, Europe and Russia T_{vis} must be greater than 70%

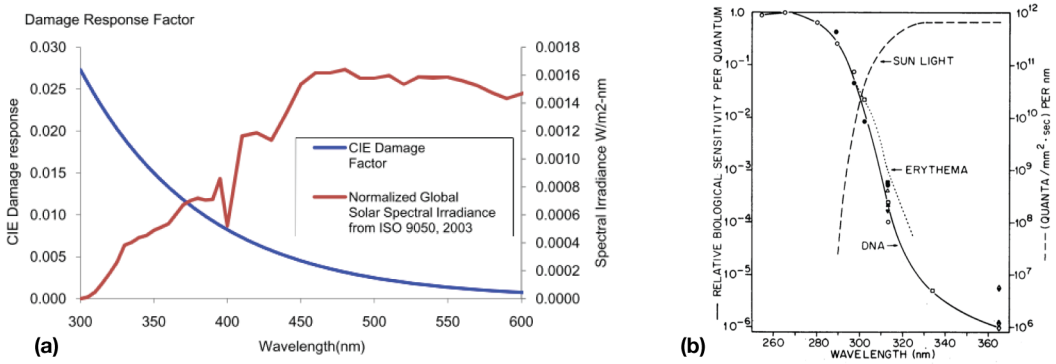

Figure 4.9: The ultra-violet damage response curves. Subfigure (**a**) shows the CIE damage response curve used to calculate the effect of UV exposure on coloured furnishing [203]. Subfigure (**b**) shows the erythemal [204] (sunburn) and DNA-damage [205] response curves, reproduced from [206].

(75% for the front windscreen of vehicles in the UK [207]). Transparency of architectural windows is not regulated but this figure indicates what is considered to provide adequate visibility under *all* light conditions. For reference, the glazing company PPG market 'tinted' glass with $9\% \leq T_{\text{vis}} \leq 37\%$ [194].

It is also interesting to observe the visible light transmittance values as defined by the Luxotica/Ray-Ban scale. Recommended indirect 'glare-reduction': on a cloudy day ($T_{\text{vis}} = 80\%$); on a moderately sunny day ($T_{\text{vis}} = 43\%$): in bright sunlight ($T_{\text{vis}} = 18\%$); and for water-sports/snow ($T_{\text{vis}} = 8\%$). This gives us a sense of the degree to which visible light can be attenuated for different applications.

4.6 Emittance

Radiative heat-transfer calculations are rarely (if ever) referred to in academic VO_2 smart-window literature; the focus is almost exclusively within the solar range ($300 < \lambda < 2500\,\text{nm}$). Convective calculations and thermal conductivity values, which are related to the bulk properties of the glass pane, are clearly best suited to complete window systems. However, interfacial calculations for energy absorptance *and re-radiation* would certainly be of value to academic work on smart-windows. Not only would this help quantify how much heat can be lost by thermal radiation, it would also provide a better picture of what levels of non-transmitted solar energy contribute to a building's internal temperature.

Interfaces that are highly absorbing exhibit different emissivities from those that are not. By Kirchhoff's law of thermal radiation, at thermal equilibrium the emittance of a surface at a specific wavelength, $\epsilon(\lambda)$, is given by,

$$\epsilon(\lambda) = A(\lambda) \tag{4.12}$$

where $A(\lambda)$ is the absorptance (ratio of energy-absorbed to incident-energy) at the same wavelength, λ i.e. a perfect 'black body' has unity emittance at all wavelengths, $\epsilon = 1 \forall \lambda$. The thermal spectral radiance, $P(\nu, \tau)$ (power radiated per unit area of emitting surface in the direction of the surface-normal per unit solid angle), at frequency $\nu = \frac{c}{\lambda}$ for a surface

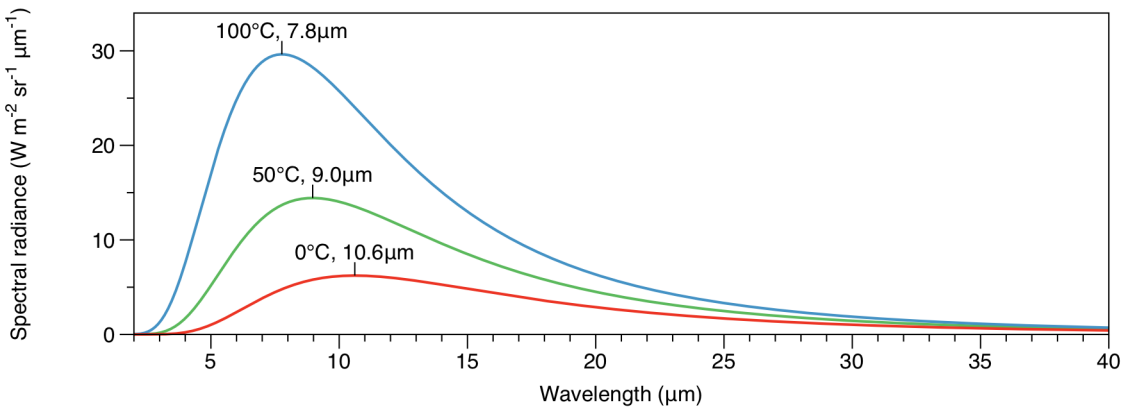

Figure 4.10: The spectral radiance of black body emitters as defined by Plank's law eq. (4.14). The wavelength of peak radiance is calculated using Wein's displacement law and is shown in the label for each of the series.

at absolute temperature τ is defined as,

$$P(\nu, \tau) = \int \epsilon(\nu) \cdot I(\nu, \tau)\ \delta\nu \tag{4.13}$$

where $I(\nu, \tau)$ is the black body spectral radiance defined as,

$$I(\nu, \tau) = \frac{2h\nu^3}{c^2} \cdot \frac{1}{e^{\frac{h\nu}{k_B \tau}} - 1} \tag{4.14}$$

where c is the speed of light, k_B is the Boltzmann constant and h is Plank's constant [208].

Since absorption is dependant upon both the nanostructure and the optical properties of an interfacial material (which for VO_2 is known to be strongly frequency-dependant within the mid-infrared region [209]), measuring the emittance for a smart-window interface requires specialist techniques – standardised in EN763. Although rare to find, emissivity measurements for VO_2 films have previously been reported by Saeli et al. [161]. These emissivity measurements were significant as they exhibited little variation between the cold state ($0.80 \leq \epsilon \leq 0.837$) and the hot state ($0.752 \leq \epsilon \leq 0.837$) and were reasonably close to unity, which lead the authors to suggest that VO_2 may not be suitable for deployment cooler climates.

It would be of particular interest if it could be shown that the absorptance/emittance spectra for a VO_2 coated motheye interface could be maximised in the atmospheric transmissive-window (7–14 μm) and minimised elsewhere. This has previously been demonstrated, with different materials (and not motheye nanostructures), to result in highly-effective radiative-cooling under direct sunlight [210].

4.7 Summary

No single metric can fully describe the energy impact of window system. In this work we use the academic (interface) weighted-mean methods. We place particular influence on $T_{\text{vis}}^{\text{cold}}$ and ΔT_{sol} as together, they give a reasonably complete description of the energy transmittance characteristics for a window interface without the excessive complexity of industrial metrics such as the G-value.

Part III

Results

Chapter 5

Energy mapping

In the previous chapter we defined two key transmittance-metrics for smart-windows $T_{\mathrm{vis}}^{\mathrm{cold}}$ and ΔT_{sol}. Both of these metrics are useful for comparisons between different thermochromic interfaces. However, they do not quantify the energy-impact of incorporating a smart-window within a building.

5.1 Building-centric calculations

5.1.1 Software modelling

Building-level energy-models account for both human use (artificial light and heat) and local environmental conditions. The most common software used to make this type of calculation is 'EnergyPlus' ('DesignBuilder') [198, 144, 211–214]. Alternatives include 'BuildingEnergy' and 'ESP-r' [215, 216].

The methodology for modelling thermochromic smart-windows is not standardised; some studies have yielded surprising results. For example, one study [215] concluded that controlling the transmittance of windows was much less important than controlling its emittance, concluding that smart-windows offer no advantage over conventional modern glazing. However, the majority of these numerical studies demonstrate that thermochromic smart-windows *do* offer significant energy-saving, particularly in warmer climates [217, 198]. For example, it was reported (using an EnergyPlus model) that a thermochromic smart-window in Rome could reduce a building's energy consumption by 51.6% [218].

5.1.2 Physical modelling

A complementary method to assess the energy impact of smart windows in a specific location is the physical construction a model-room. The energy impact of smart-windows installed within the model are assessed by monitoring the its energy consumption over a period of time [216].

A recent study in which two identical, full-scale rooms were constructed on top of a building in southern China showed that a simple VO_2 based smart-window was able to reduce the cooling load by 10.2-19.9% [219]. Despite the requirement for additional lighting in the smart-window equipped room, total electricity consumption was reduced by 9.4%. This study, conducted over a seven-day period, was notable as very few experimental demonstrations have been performed on this scale.

It is generally accepted the potential to save energy using smart-windows scales with the window-area to room-volume ratio. This is normally attributed to the blocking or passing of *direct* solar radiation. Interestingly however, it was found that a smart-window equipped room had a reduced cooling-load regardless of the room's orientation [219].

5.2 Map-centric calculations

The building-level approach to calculating the energy-impact of thermochromic smart-windows is location-specific. Although some studies do include energy-impact calculations for a range of locations we feel that a broader view could be helpful. We have developed an approach toward prospecting smart-window locations across the globe. What sets this method apart is that it makes no assumptions about a building's materials or geometry. Instead, it focuses upon weather patterns and the thermochromic response of a smart-window. The method supports multi-mode analysis: we will demonstrate this by combining weather data, solar-intensity and population distribution statistics. In principal, the technique could be extended to include additional data such as the local cost of energy or source of local electricity (e.g. renewable or fossil fuel). To the best of our knowledge, this is the first time a study of this its kind has been conducted in an academic context.

5.2.1 Data

We utilised three key data elements: world population distribution, local temperatures patterns and solar-intensity cycles.

Population

Our source of population data was the Socioeconomic Data and Applications Centre (part of NASA's Earth Observing System Data and Information System hosted by Columbia University). The data-set has a location resolution of 1° and was derived from the 'Population Count Grid Future Estimates' for the year 2015 (see fig. 5.4 on page 72).

Climate

Weather data was sourced from the same databases used by the 'EnergyPlus' software. The extraction of the data was automated allowing us to parse data from 2590 individual weather stations. This comprised of: the coordinates of each weather station, the 'dry-bulb' temperature and 'Global Horizontal Irradiance'. Both 'dry-bulb' and 'Global Horizontal Irradiance' values were provided as monthly averages for each hour of the day i.e. a $[24 \times 12]$ data-set. Therefore, in order to reconstruct the weather patterns over the course of a year this was expanded to a $[24 \times 365]$ data-set. See the 'stepped' data in fig. 5.1 on the following page.

Dry-bulb temperature, measured in °C, is the temperature recorded by a thermometer in a moisture-free atmosphere shielded from solar radiation.

Global Horizontal Irradiance is the sum of both 'Direct Normal Irradiance' (line of sight from the sun) and 'Diffuse Horizontal Irradiance' (from all directions, scattered by particles in the atmosphere).

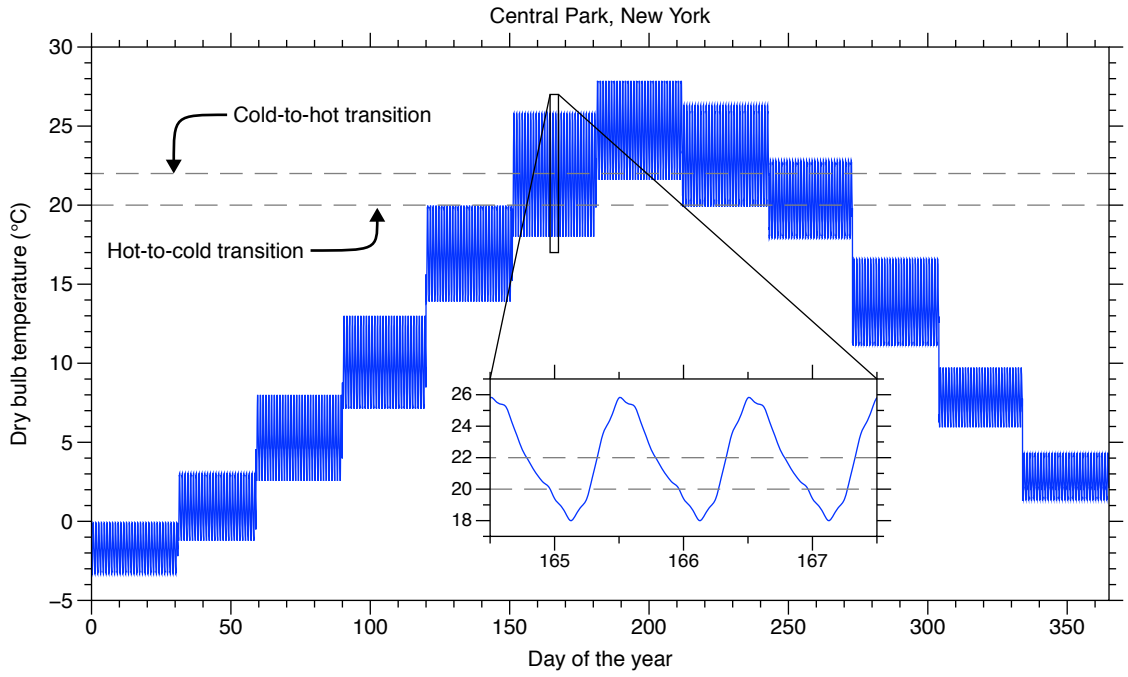

Figure 5.1: Temperature variations over the course of a year in New York's Central Park (USA).

5.2.2 Thermochromic-window model

Our model for a thermochromic window accounted for a phase transition-hysteresis of 2 °C which falls within the bounds established by previous energy modelling studies and is close to what is achievable through Ti doping [218, 146].We assumed that the cold to-hot transition occurred at 22 °C and whilst the hot to-cold transition occurred at 20 °C (see fig. 5.2) i.e. imitating a film that was doped with approximately 3 % tungsten [140]. These is an idealised case, it is of course likely that a real system would have a larger transition hysteresis, for example. However, these values were chosen for the purpose of discussion and could be modified in a future study.

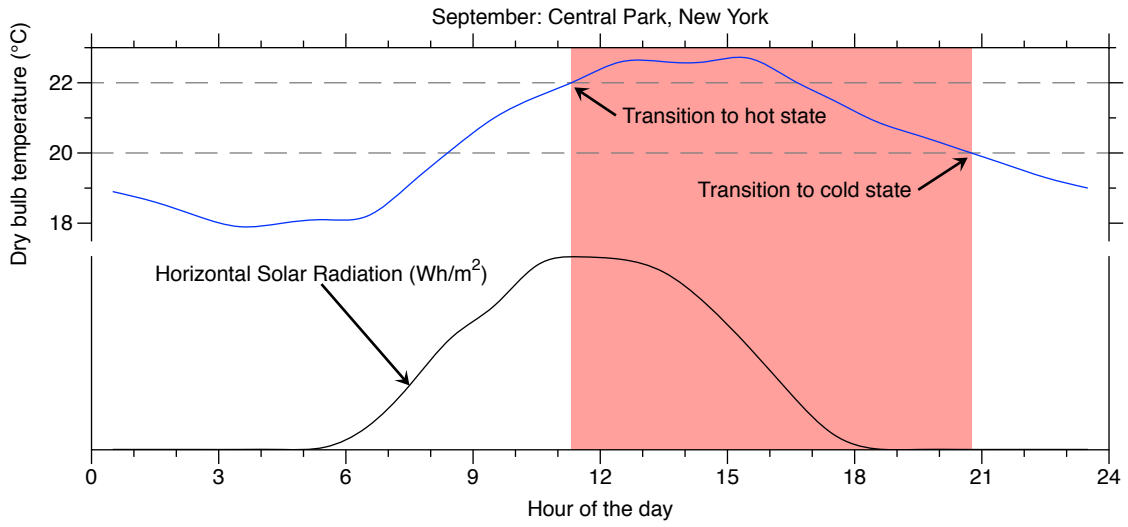

Figure 5.2: The temperature profile for Central Park in New York (USA) for an average day in the month of September.

5.2.3 Calculation procedure

The calculation method involved time-stepping through an entire year and recording a figure of merit (e.g. number of transitions between thermochromic states) for each location (see fig. 5.1 on page 69 and fig. 5.2 on page 69). The figures of merit were then interpolated across a world map.

Number of transitions between thermochromic state

Our initial hypothesis was that thermochromic windows would be most effectively deployed in locations where they switched frequently. However, it became clear that regions which induce large numbers of switches over the course of a year (e.g. India) do so as a result of low *night-time* temperatures. A smart window in this scenario would enter its cold state but would not incur a solar-heating benefit due to the lack of sunshine. It would then enter its hot-state early in the morning and remain like this for the remainder of the day before returning to its cold-state in the evening. Therefore, switching-frequency was abandoned as a deployment indicator.

5.2.4 Solar-averaged share-of-states

We believe the most promising indicator for the effective deployment of a thermochromic smart-window is the 'solar-averaged share-of-states'. This takes into account variations in solar intensity over the course of a day. Figure 5.3 on the following page shows a global map of the 'solar-averaged share-of-states' during the course of a complete year. Dark-blue areas indicate regions in which most of the sun's energy is incident whilst the window is in its cold state. Dark-red areas indicate regions in which most of the sun's energy is incident whilst the window is in its hot state.

Our premise is that an ideal location for a thermochromic smart window is one in which the sun's energy is useful for heating during some parts of the year but, during other times, should be rejected. In the dark-blue regions of the map a greenhouse effect (solar-transmitting) is almost always desirable, whereas in the dark-red regions solar-blocking is required for most of the year. It would be reasonable to assume that a static coating could be designed to best fulfil the energy requirements in these more 'extreme' areas. Therefore, it is the light-coloured, mid-blue and mid-red temporate climates in which the dynamic properties of a thermochromic smart window are best exploited. Further work will be required to link a thermochromic window's energy-impact (on a building-level) with our 'solar-averaged share-of-states' metric.

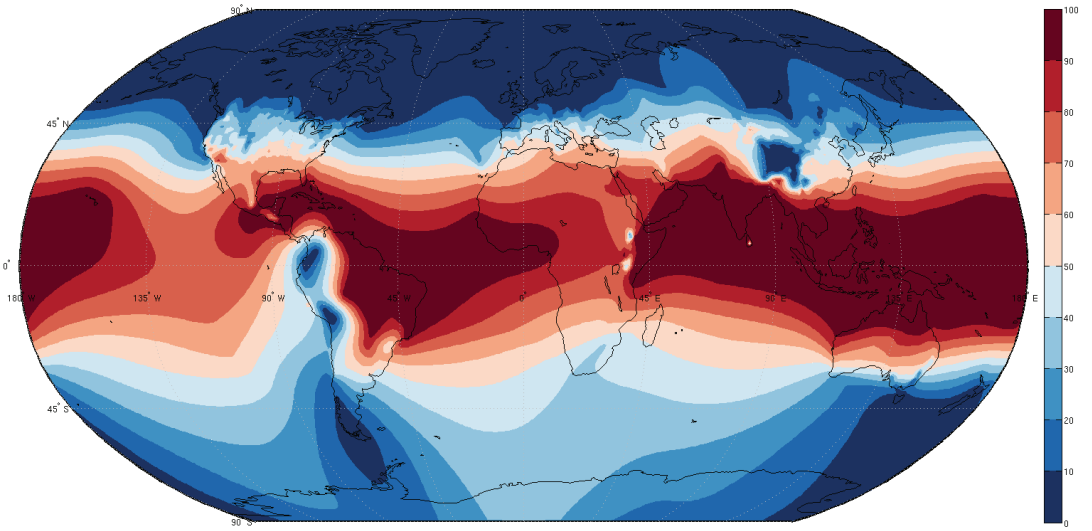

Figure 5.3: World map of the solar-averaged share-of-states. Dark-blue areas indicate regions in which most of the sun's energy is incident whilst the window is in its cold state. Dark-red areas indicate regions in which most of the sun's energy is incident whilst the window is in its hot state. The light-coloured, mid-blue and mid-red temperate-climates are those in which the dynamic properties of a thermochromic smart window are best exploited.

Case study: New York

A good example of a region in which a thermochromic smart-window would have both positive heating- and cooling- effect is New York. It has a solar-averaged share-of-states close to 50% (see fig. 5.3). During the winter months solar energy would be allowed to enter buildings, whilst during the summer months it would be rejected (see fig. 5.1 on page 69).

In the intermediary spring and autumn months the window would begin each day in its cold state (helping to raise the internal temperature of cold buildings). Around midday, during these months, the window would undergo a phase-change and enter its hot state, thereby counteracting any excessive heating which may otherwise have occurred By the late-afternoon the window will have switched back to its cold state which induces a final greenhouse heating effect to end the day. See fig. 5.2 on page 69 for details.

5.3 Assessing market potential

We found mega-cities such as São Paulo (Brazil) and Chongqing (China) also exhibited a good 'solar-averaged share-of-states'. As part of this study we combined our 'solar-averaged share-of-states' data (fig. 5.3) with population distribution-statistics (fig. 5.4 on the next page) to estimate what portion of the world's population could experience a benefit similar to New York, São Paulo or Chongqing.

We used a histogram to visualise these results (see fig. 5.5 on the following page). We bracketed the population who occupied the 40-60% 'solar-averaged share-of-states' range which accounted for approximately 1.5 billion people. However, the choice of these bounds is somewhat arbitrary (2 billion people occupy the 35-65% region). Clearly, populations occupying the centre of the histogram will see a significant benefit from the technology.

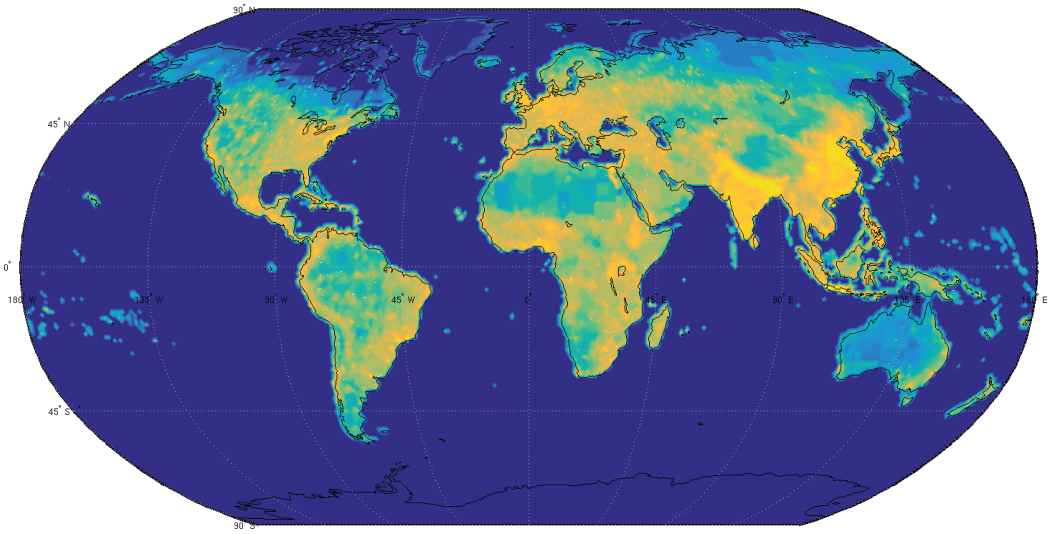

Figure 5.4: Map of the world's population distribution.

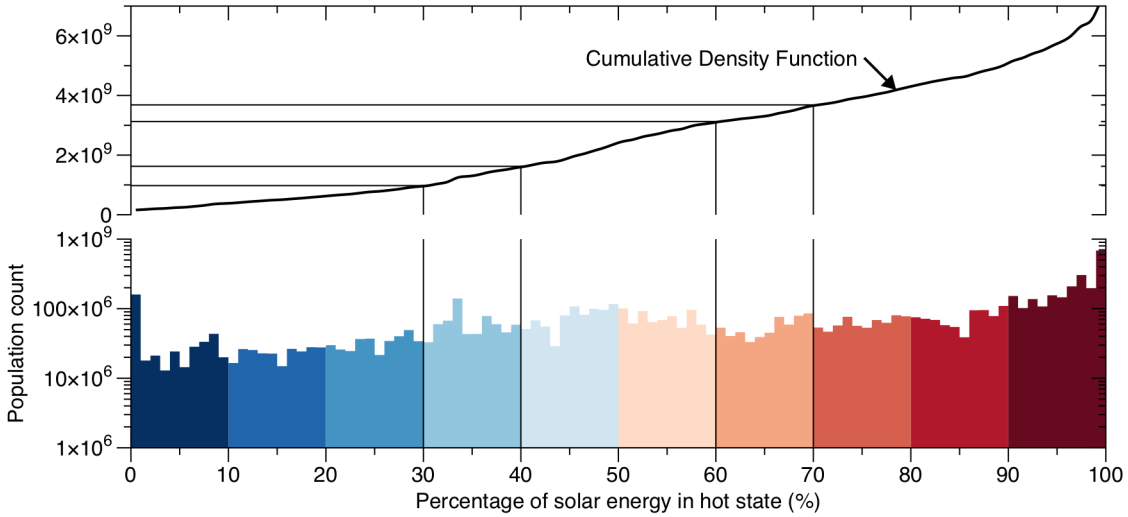

Figure 5.5: Histogram showing the number of people world-wide who would experience different 'solar-averaged share-of-states'. Population on the far-left would experience cold state temperatures year-round and would see no benefit in blocking solar-radiation. Population of the far-right would experience hot state temperatures year-round and would never wish to transmit infrared solar-energy into their homes. The population occupying the centre would benefit from both a reduced greenhouse effect in hot weather and solar-heating during cold weather. The cumulative density function (top) shows that 2.7 billion people live in regions where the solar-averaged share-of-states is 30–70%, and 1.5 billion of these people live within the 40–60% sub-bound.

5.4 Conclusions

In conclusion, we have used global weather data to predict the response of an ideal thermochromic window. By combining this information with solar-intensity data we have identified regions in which a balance of hot and cold states can be achieved. Finally, we have integrated population distribution statistics into our model in order to gain insight into what proportion of the world's population could experience a benefit from thermochromic smart windows.

This study represents the first-step toward assessing the market-potential for thermochromic smart-windows. It remains to be proven that our assumption of a balanced 'solar-averaged share-of-states' is a good indicator of energy saving for thermochromic smart windows. Correlation should be sought between 'solar-averaged share-of-states' and both software and physical smart window models (as described at the beginning of this chapter, section 5.1 on page 67).

An extension of this study could expose the tolerance to large phase transition-hysteresis and different switching temperatures by varying these parameters in the model (see fig. 5.2 on page 69). It would also be of interest to combine additional regional data such as the local share of energy expenditure on lighting, heating and cooling; the local cost of energy per kWh; and finally the source of local energy.

Chapter 6

The optical constants of vanadium dioxide

The optical properties of vanadium dioxide, such as transmittance, can be calculated and predicted only if its refractive index in known. In this chapter we describe the synthesis of vanadium dioxide, via Atmospheric Pressure Chemical Vapour Deposition (APCVD), and its full-scale characterisation. This chapter includes results obtained as part of a collaborative effort led by myself which includes Delphine Malarde, Christian Sol, Michael Powell and Raul Quesada Cabrera.

6.1 Synthesis via Atmospheric Pressure Chemical Vapour Deposition

The thin-film used for this study was produced with Delphine Malarde within UCL's Department of Chemistry. A reaction between vanadium tetrachloride (VCl_4, the V source) and ethyl-acetate ($C_4H_8O_4$, the O source) took place on the surface of a 15×7.5 centimetre piece of Pilkington barrier glass, see fig. 6.1 on the next page. The glass substrate (3.2mm total thickness) included a pre-deposited 10 nm SiO_2 layer that prevented Sn ions in the bulk material from diffusing into the synthesised vanadium oxide. Deposition took place at 600 °C within a furnace free to vent to atmosphere. The gas-phase precursors were transported into the furnace (first through the mixing chamber and then through a series of baffles)and over the substrate by N_2 carrier gas at a combined plain flow of 23.25 litres per minute (equivalent to 165 mmHg). The VCl_4 bubbler, held at 45 °C, measured a flow rate of 0.80 litres per minute (equivalent to 42 mmHg); the ethyl-acetate bubbler, held at 32 °C, measured a flow rate 0.16 litres per minute (equivalent to 7 mmHg). Deposition time was 63 seconds. We have previously reported a variation of this route to vanadium oxide synthesis [166].

We applied an indexing system (2.5×2.5 cm square grid) in order to distinguish between different regions of the film. A post-deposition visual inspection showed reasonably uniform growth, darker toward C1 (closest to the point of entry of the vanadium precursor into the reactor), and little or no transmittance haze, see fig. 6.1 on the following page.

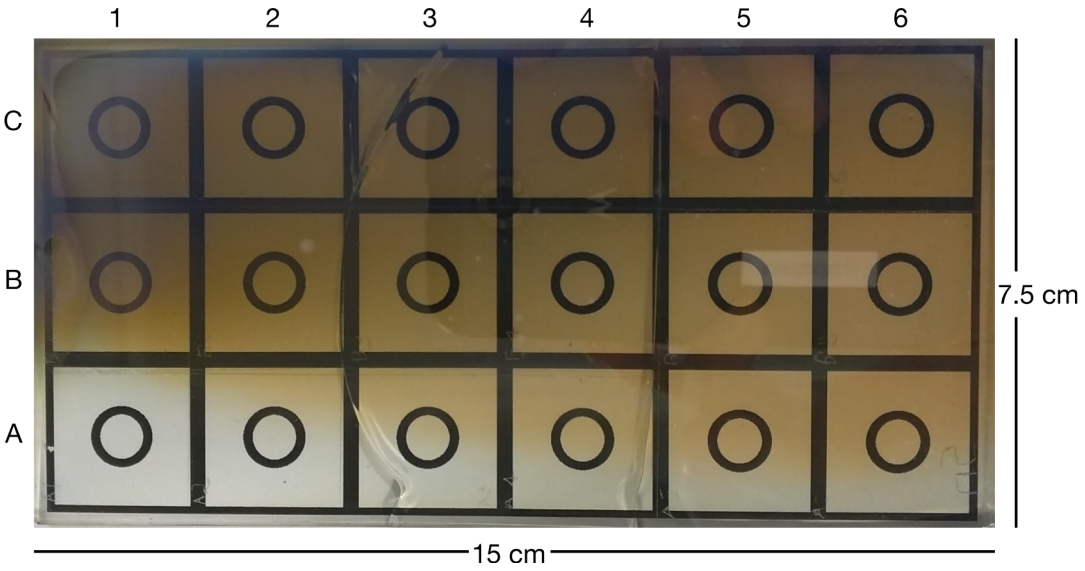

Figure 6.1: The vanadium dioxide film, synthesised via Atmospheric Pressure Chemical Vapour Deposition, used as the subject of this study. A 2.5×2.5 cm square-grid coordinate system is underlaid in order to distinguish between different regions of the film. The gaseous precursors entered the furnace closest to C1 and flowed from left-to-right. The sample partially shattered during the cooling process. Full deposition conditions are provided in section 6.1 on page 74.

6.2 Phase-mapping

In order to ascertain the oxidation state of the synthesised material and verify it was not contaminated, we performed a series of phase-mapping studies at each coordinate location.

6.2.1 X-ray Diffraction crystallography

X-ray Diffraction (XRD) measurements were performed using a 1.54060 nm X-ray source. Reference patternswere obtained from the Inorganic Crystal Structure Database (ICSD), provided by the National Chemical Database Service, and extracted using the 'Mercury' software package, see fig. 6.2 on the next page. The signal-to-noise ratio is poor, particularly for positions A1 and A2, as the synthesised film is very thin at these points.

The diffraction patternsfor our sample exhibited a strong peak at $2\theta = 28°$ corresponding to the monoclinic VO_2(002) peak [220]. In some locations, a small peak was also visible at $2\theta = 42°$, this is a peak position shared by both the VO_2(M) and V_2O_5 phases. However, none of the principle V_2O_5 peaks ($2\theta = 20°$, $21°$, $31°$ or $15°$) were observed. This evidence would support the observed $2\theta = 42°$ peak should be attributed to VO_2(M), not V_2O_5.

Finally, a peak at $2\theta = 14°$ was observed at position C1. This peak does not match with any for the VO_2(M) phase or those within the V_2O_3 or V_2O_5 patterns. However, it *does* make a match with a peak found in the VO_2(B) phase. Indeed, upon closer inspection of the C1 diffraction pattern, a small peak may also be visible at $2\theta = 29°$ and may also be present in the C2 diffraction pattern (although not strongly expressed). Therefore, there is some evidence that within the highest growth-rate regions (nearest the precursor entry point) some VO_2(B) material may have been synthesised and a mixed phase is present.

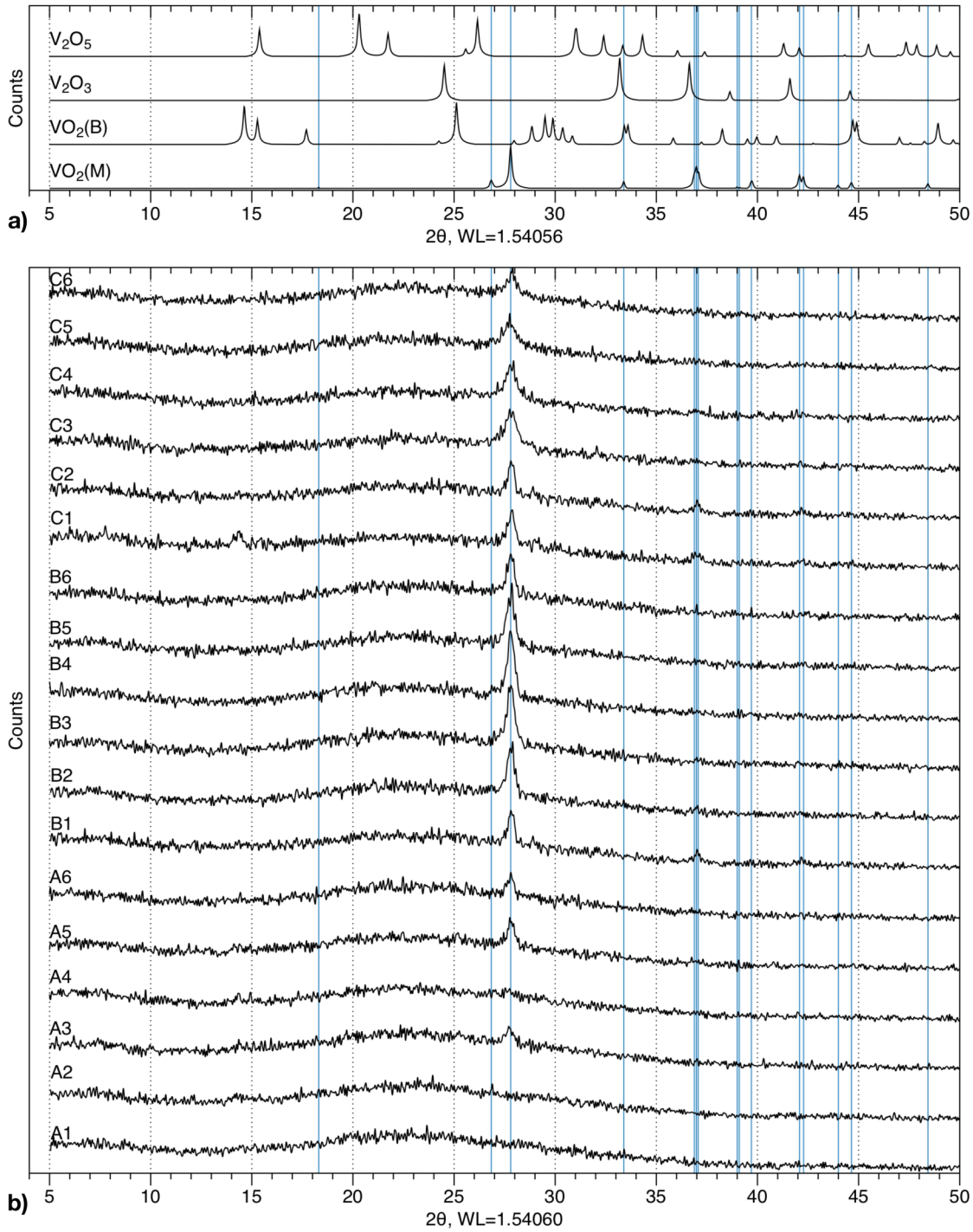

Figure 6.2: X-ray diffraction crystallography of vanadium oxides. (**a**), reference diffraction patterns for common vanadium phases V_2O_5, V_2O_3, VO_2(B) and VO_2(M) obtained from the Inorganic Crystal Structure Database (ICSD) and extracted using the 'Mercury' software package. (**b**), X-ray diffraction patterns for each coordinate position of our sample (shown in fig. 6.1 on page 75). Vertical purple lines have been underlaid on both plots to show the positions of peaks matching the VO_2(M) phase. This data was captured by Delphine Malarde.

6.2.2 Raman spectroscopy

A Renishaw spectrometer system was used to perform Raman spectroscopy using a 514.5 nm, 6 mW argon-laser excitation source. The measurement was performed at room-temperature as it is known the VO_2(M) exhibits clear bands, whereas VO_2(R) does not [142].

Our measurements, shown in fig. 6.3 on the following page, are in good agreement Raman spectra for VO_2(M) found in the literature [221, 142, 156]. A comparison with the Raman band structure for VO_2(B) and V_2O_5 shows that all of the peaks can be attributed to VO_2(M) – no stray peaks belonging to either VO_2(B) or V_2O_5 were found [220].

6.3 Topography

6.3.1 Atomic Force Microscopy

Using Atmospheric Pressure Chemical Vapour Deposition in a previous study, we showed that the same chemical precursors could produce VO_2 films with a high surface roughness (RMS of 124.55 nm [166]), see subfigure (**b**) in fig. 6.4 on page 79. These films appeared hazy in both reflection and transmission. In this study we used increased flow-rates in order to counteract the high reactivity of our VCl_4 precursor; we found this produced a film with noticeably less haze than our previous attempt. In order to verify this was due to a different surface morphology, we performed Atomic Force Microscopy (AFM) on the sample in several locations over $5 \times 5\,\mu$m areas, see subfigure (**a**) in fig. 6.4 on page 79. These scans showed the samples produced for this study were significantly smoother, exhibiting an RMS roughness of 11.8 nm, and were therefore likely to scatter less light than their rougher predecessors.

6.4 Refractive Index

6.4.1 Dispersive models in the literature

A variety of dispersive models have been used to describe the refractive index of vanadium dioxide. The first reported dispersive model for vanadium dioxide (by Verleur [209]) comprised of an ensemble of nine different Lorentzian oscillators. The modern-day standard employs only two oscillators in the semiconductor cold state with energies of $E_1^{\text{cold}} \approx 3.5$ eV (attributed to interband transitions from the oxygen $2p$ to the empty vanadium $3d$ band) and $E_2^{\text{cold}} \approx 1.4$ eV (related to the transition of trapped carriers between the split vanadium $3d$ band) [226]. Upon transition to the hot state, the energy of the first oscillator decreases to $E_1^{\text{hot}} \approx 3.1$ eV (due to a reduction of the vanadium $3d$ band energy) and the second oscillator collapses to $E_2^{\text{hot}} \approx 0$ eV (as the increased Fermi level frees electrons localised in the vanadium $3d$ band), see fig. 3.3 on page 50 and our discussion in section 3.2 on page 49.

6.4.2 Variable Angle Spectroscopic Ellipsometry

We performed variable angle ellipsometric measurements on our sample using a Semilab SE2000 spectroscopic ellipsometer over a range of angles. The angles of incidence were chosen to cover the range of Brewster angles 66° ($n = 2.5$) up to 74° ($n = 3.2$) in steps of 2° in order to maximise the measured amplitude component, Ψ, and phase difference, Δ. Our

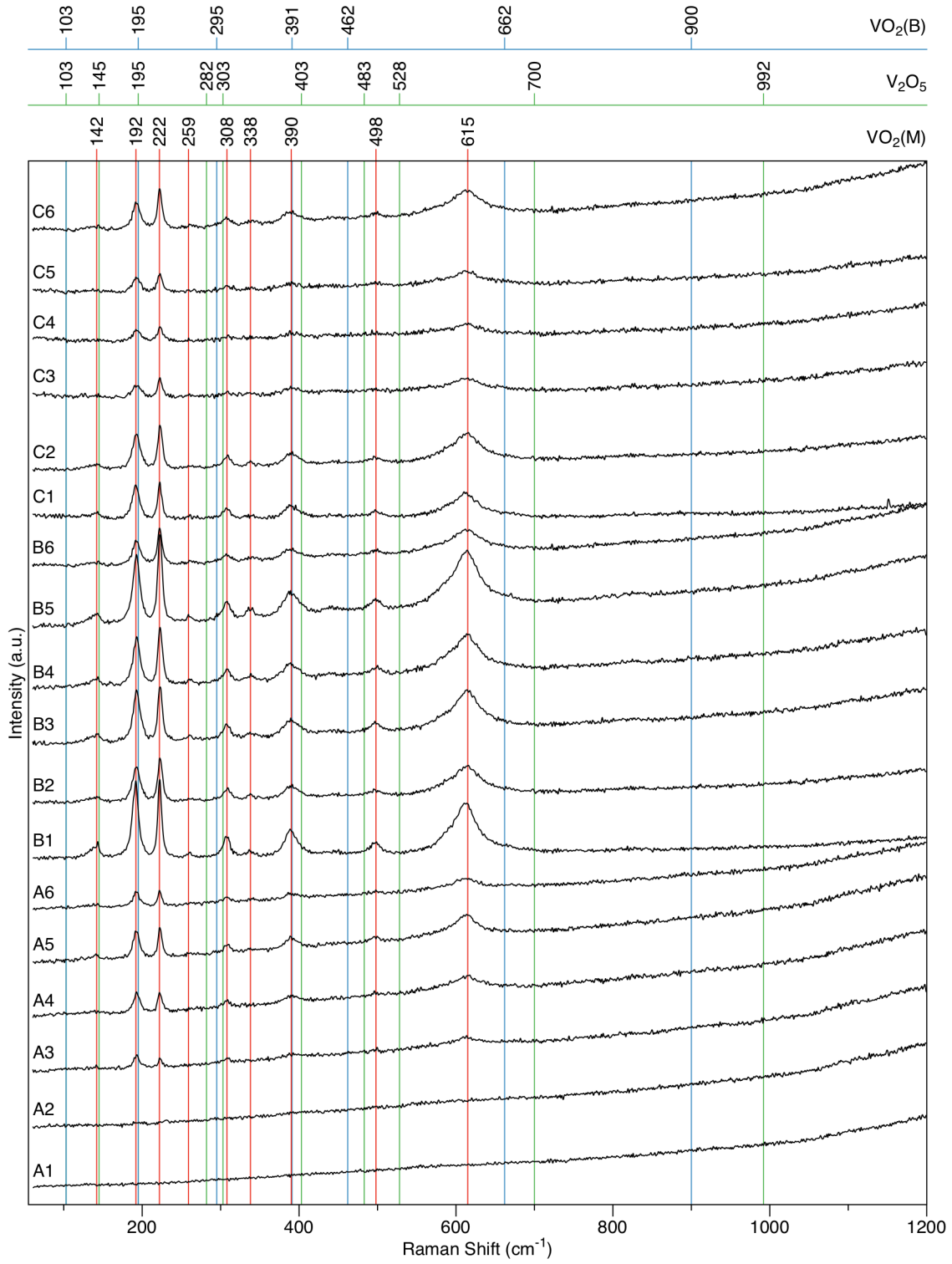

Figure 6.3: Raman spectra taken from our sample and a variety of vanadium oxides. Vertical red lines have been underlaid to show the positions of peaks matching the VO_2(M) phase [222–224, 220, 225]. The purple and green vertical lines represent the position of band that would exist had either a VO_2(B) or V_2O_5 phase been synthesised [220]. This data was captured by Raul Quesada Cabrera.

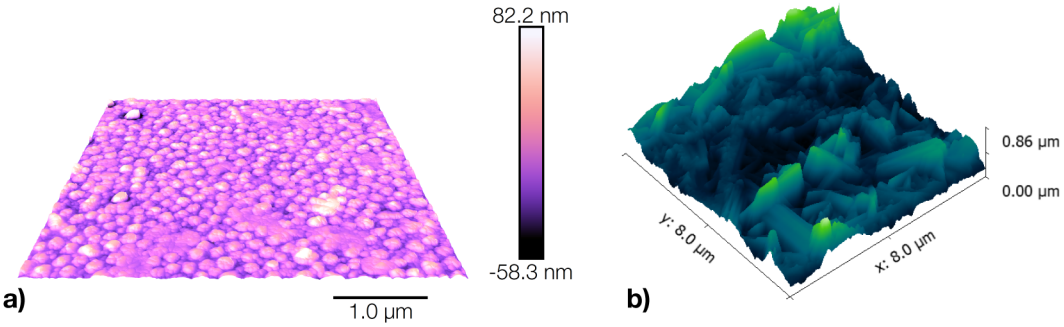

Figure 6.4: Atomic Force Microscopy scans of VO_2 films fabricated by Atmospheric Pressure Chemical Vapour Deposition using VCl_4 and ethyl-acetate. Subfigure (**a**), is the subject of this chapter; subfigure (**b**), is a the film synthesised in a previous publication [166].

measurements were taken for wavelengths between 250 nm (4.96 eV) and 1650 nm (0.75 eV). Region B4 of our sample was chosen for our ellipsometric investigation as, based upon our investigations up to this point, it showed no presence of mixed oxidation-phases.

Our structural model consisted of a bulk substrate (soda-lime glass) topped with a 10 nm layer of SiO_2, the combination of which mimics the structure of 'Pilkington barrier glass'. Upon this, our dispersive model for vanadium dioxide was divided into two-halves: the bottom layer (in contact with the SiO_2 substrate) was modelled at 100% density whilst the top layer was treated as a Bruggeman effective-medium (discussed previously) with variable density composed of air and VO_2 representing the effect of sub-wavelength surface roughness.

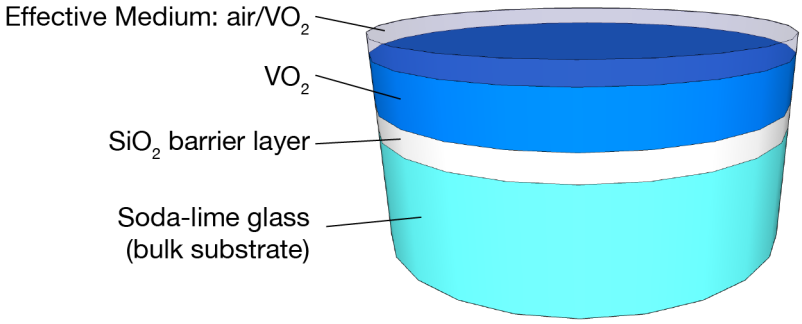

Figure 6.5: The structural model used for ellipsometric fitting.

Our dispersive model for soda lime glass (the bulk substrate material) comprised of a Cauchy term and a single high-energy Lorentz oscillator which accounted for the absorbing presence of Sn from the float-glass process. The SiO_2 barrier layer was modelled as a single-termed Sellmeier material. Both our cold state and hot state models for VO_2 employed two Lorentz oscillators (for the reasons discussed above), however, the hot state dispersive model also included a Drude term in order to account for the semi-metallic behaviour of the the rutile crystal. The effective medium model used as an inter-layer between the air and VO_2 was chosen to follow a Bruggeman form as this made no assumption regarding which material has the highest constituent fraction.

The Levenberg-Marquardt algorithm was used to fit the dispersive and structural parameters described above. For the cold state, it converged when the root-mean-square error reached RMSE = 0.37 yielding an R-squared value of $R^2 = 0.996$; for the hot state

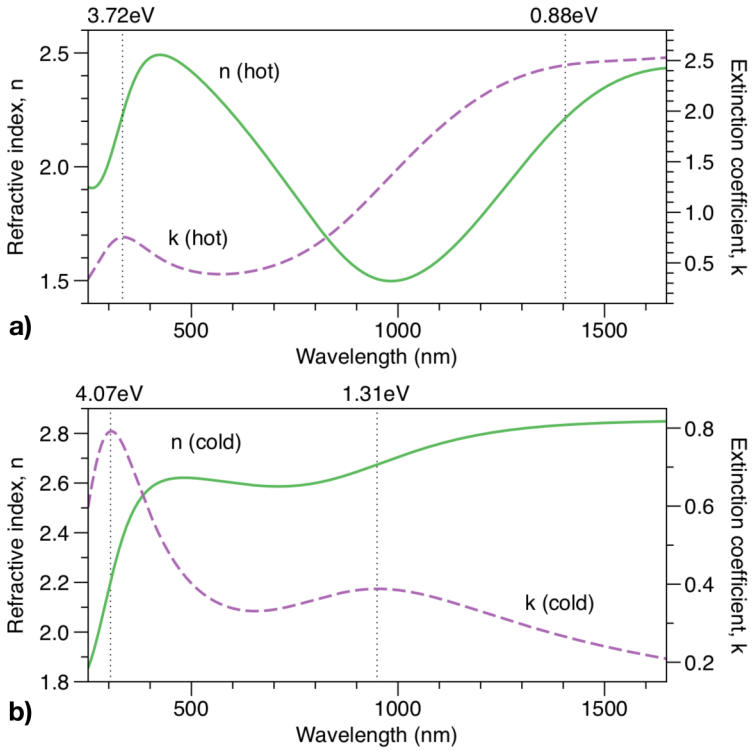

Figure 6.6: Refractive index for our VO_2 sample (DM27) in both (**a**) the hot (90 °C), and (**b**) cold states (22 °C). The energy of the two Lorentz oscillators used to make the fitting have been underlaid (vertical dotted lines).

it converged with when the root-mean-square error reached RMSE = 0.61 yielding an R-squared value of $R^2 = 0.992$.

It was determined that the thickness of the SiO_2 barrier layer was 10 nm (as expected), the high-density VO_2 region 32 nm and the low-density 'roughness' region to be 22 nm with a 12% fraction of VO_2 (the remainder being air). The cold state VO_2 Lorentzian oscillators were determined to have energies (and broadening terms) of $E_0 = 4.07$ eV ($\Gamma = 3$ eV) and $E_0 = 1.31$ eV ($\Gamma = 1.1$ eV) — only slightly less than Kakiuchida's value for electrons trapped between the split vanadium $3d$ band and slightly greater for the oxygen $2p$ to vanadium $3d$ transition [226]. The hot state VO_2 Lorentzian oscillators were determined to have energies (and broadening terms) of $E_0 = 3.72$ eV ($\Gamma = 2.24$ eV) and $E_0 = 0.88$ eV ($\Gamma = 0.61$ eV) with a Drude term exhibiting a plasma energy of $E_\mathrm{p} = 2.74$ eV and associated broadening of $E_\Gamma = 0.35$ eV.

6.5 Summary

The refractive index obtained in this investigation (fig. 6.6) represents a key result. We know that from our Atomic Force Microscopy that our structural model for the ellipsometric fitting was appropriate and that the vanadium dioxide used for these measurements was phase-pure. These optical constants form the back-bone for our calculations and simulations in the following chapters.

Chapter 7

The performance boundaries of vanadium dioxide smart window systems

Studies in which the geometry of a given VO_2 smart window system is optimised through a series of parameter searches are commonplace [124, 148, 227, 228, 19]. However, the mode of comparison between each element of these series is often bespoke and the choice of an 'ideal' geometry can appear arbitrary.

In this chapter we will explore the capability of the $T_{\text{vis}}^{\text{cold}}$ vs. ΔT_{sol} scatter-representation to expose geometry-specific performance boundaries for smart-window systems (as discussed previously, section 4.2.1 on page 59). We also demonstrate how the technique can be used to expose exactly which parameters of a given system contribute to the best-performing 'boundary-cases'. This information is then available to inform geometry-specific design-rules.

Trade-off principal The persistent challenge for VO_2-based smart-windows has been to simultaneously maximise the transmittance of visible light (T_{vis}) and the window's solar-energy modulation (ΔT_{sol}). The penalty for modulating solar transmittance via an absorption process is a reduction of visible light transmittance. In order to increase T_{vis}, one must either accept a reduced ΔT_{sol} or compensate for absorption losses by engineering a reduction of reflectance in order to enhance transmittance. In this chapter we show that there is a maximum absorptance-mediated solar energy transmittance modulation, ΔT_{sol}. This is directly related to the shape and magnitude of vanadium dioxide's extinction coefficient (k, see fig. 6.6 on page 80).

7.1 Calculation methods

We use two different methods to calculate the transmittance through smart-window interfaces: Finite Difference Time Domain simulations and the Transfer Matrix technique. The choice between each of these calculation methods is based upon the complexity of a given system's geometry. Simple planar-stacks of thin-films can be well-described by the Transfer Matrix technique. However, for systems with a three-dimensional nanostructure (such as motheye smart windows) Finite Difference Time Domain simulation provides

reliable results at the expense of computational resources.

7.1.1 Finite Difference Time Domain

The principle behind the Finite Difference Time Domain technique (FDTD) is to divide the simulation region into a three-dimensional mesh, the 'Yee-grid'. Each element of the Yee-grid is assigned a permittivity that represents the dispersive materials at that point in periodic-space. A broadband electromagnetic pulse is injected into the simulation space and Maxwell equations are then solved iteratively, in small time-steps. Propagation of electromagnetic fields within the simulation region are monitored and then undergo post-processing to determine, for example, an interface's transmittance value. A series of convergence tests must be made in order to verify that the discretisation of a nanostructured interface in both spatial and temporal dimensions accurately represents reality. The resolution of each simulation parameter must be varied until a steady-state is achieved.

7.1.2 Transfer Matrix

Transfer Matrix calculations are significantly less resource-intensive than FDTD. However, the core technique is limited to one-dimensional systems (i.e. layered interfaces) and cannot account for effects such as scattering. The calculation is performed independently for each wavelength and must be repeated multiple times in order to extract the broadband transmittance of an interface. Phase information of an electromagnetic wave is preserved throughout the simulation space and at each interface the Fresnel equations for transmittance, reflectance and angle of propagation are solved. Absorptance is based upon the extinction coefficient of each material within the simulation. Multiple reflections within each layer, as per a resonant cavity, are fully supported. However, since there is normally no loss of phase information, electromagnetic waves are treated as infinitely coherent. Therefore, care must be taken that the optical thickness of each layer within the system is less than the free-space coherence length, l_c, of the illuminating source (e.g. $l_c = 600\,\text{nm}$ for sunlight [229]).

7.1.3 Electromagnetic material models

Both of the techniques used in this section are broadband and require the refractive indices of every material to be fully-specified.

As discussed in chapter 3 on page 48, the refractive index of VO_2 can differ between deposition techniques and its layer thickness etc. For simplicity, we use the same material model regardless of the simulated system's geometry. The calculations presented in this chapter use the refractive index of VO_2 reported in chapter 6 on page 74.

It is important to acknowledge that the absolute values of transmittance used to construct a performance boundary (T_{vis} and ΔT_{sol}) may differ due to different synthesis conditions and material density. However, the relationships between the boundaries of each system are unlikely to be significantly altered. Therefore, assuming the characteristic shape of vanadium dioxide's refractive index remains unchanged, the design rules that we deduce in this investigation are assumed to be (to a reasonable degree) universal.

Simple dielectric models (non-dispersive) were used for air and glass. Our material model for SiO_2 (glass) was taken from Palik [230]. Air was modelled as a dielectric with a unity refractive index ($n = 1$).

7.2 Planar vanadium dioxide thin-film

The simplest VO_2 smart-window interface is a planar, thin-film on glass. We calculated $T_{\text{vis}}^{\text{cold}}$ and ΔT_{sol} for thicknesses of VO_2 ranging from 0–300 nm using the Transfer Matrix technique.

Our results are plotted as a function of the VO_2 layer-thickness in fig. 7.2 on the following page. As the film thickness increases, constructive and destructive resonances contribute to an undulating $T_{\text{vis}}^{\text{cold}}$ (subplot (**a**)). The undulations are not pronounced for ΔT_{sol} as it is a very broadband weighted metric. It is interesting to note that at specific thicknesses, around 66 nm, these resonances contribute to a flat transmittance spectrum (in the cold state) i.e. light transmitted through this interface would receive a neutral tint. See fig. 7.1.

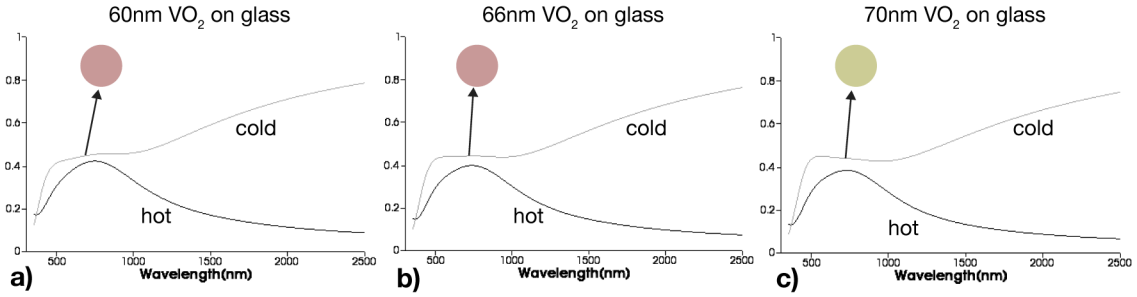

Figure 7.1: Transfer Matrix calculations of transmittance through planar VO_2 thin-films on glass. Subfigure (**a**) shows a 60 nm layer of VO_2; (**b**) shows a 66 nm layer of VO_2; (**c**) shows a 70 nm layer of VO_2. The perceived tints for the cold-state transmittance spectra are displayed as circular insets. A shifting resonance peak in the visible part of the spectrum manifests as flat transmittance (neutral tint) at 66 nm, (**b**).

It is clear from subplot (**a**) (fig. 7.2 on the following page) that ΔT_{sol} is limited; its value initially increases as the volume of thermochromic material also increases. However, there comes a point ($d \approx 145$ nm) whereby absorption penalties within the layer dominate and the solar-transmittance modulation becomes capped at $\Delta T_{\text{sol}} = 14.5\%$. Planar systems in which the thickness of VO_2 is greater than 145 nm see diminishing returns as both $T_{\text{vis}}^{\text{cold}}$ and ΔT_{sol} suffer from parasitic absorption.

In fig. 7.2 on the next page we plot both $T_{\text{vis}}^{\text{cold}}$ and ΔT_{sol} as a function of VO_2-thickness and also ΔT_{sol} as a function of $T_{\text{vis}}^{\text{cold}}$ (as discussed in section 4.2.1 on page 59). The dashed line in subplot (**b**), fig. 7.2 on the next page, represents our primary smart-window 'performance boundary' or 'performance limit'.

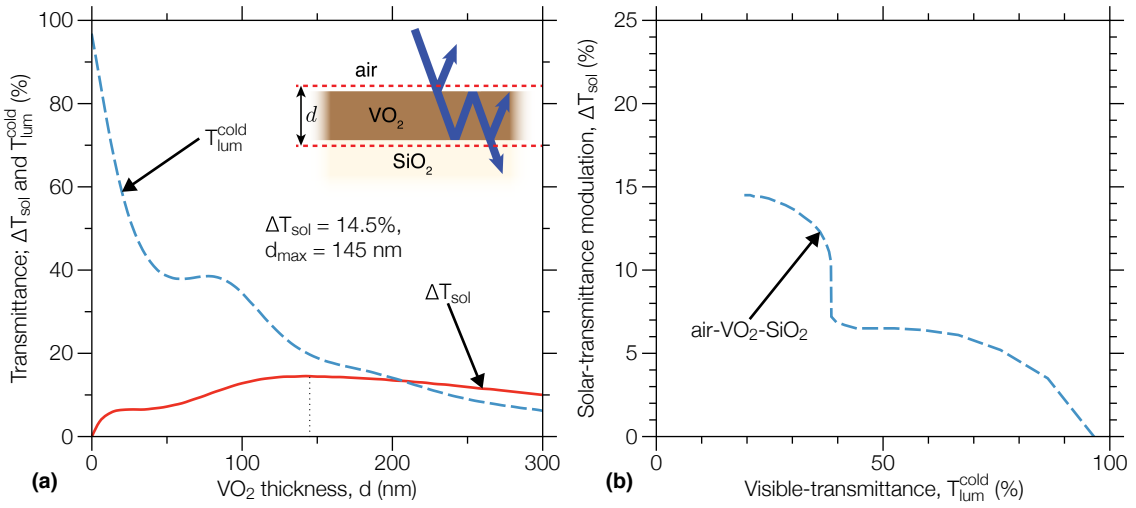

Figure 7.2: Interference within a simple planar VO_2 layer contributing to a nuetral tint. Transmittance calculated using a Transfer Matrix method for planar VO_2 thin-films on glass: the simplest VO_2 smart-window system. Subfigure (**a**) shows $T_{\text{vis}}^{\text{cold}}$ and ΔT_{sol} for different VO_2 film-thicknesses, whereas (**b**) plots these two metrics directly against one-another. The dashed line in subplot (**b**) is a 'boundary' that must be engineered across in order to access the high-performing upper-right region of the plot.

7.3 Bulk vanadium dioxide

Performing the same calculation as above but removing the SiO_2 and air materials from our model allows us to decouple both the interface-driven Fresnel-losses and resonant-cavity effects from the transmissive properties of VO_2. The two metrics, $T_{\text{vis}}^{\text{cold}}$ and ΔT_{sol}, are plotted as a function of bulk-distance in fig. 7.3 on the following page. A key result is that solar-transmittance modulation has an upper limit of $\Delta T_{\text{sol}} = 24.9\%$ and is maximised by travelling through 109 nm of bulk–VO_2. For distances greater than this, absorption penalties degrade both the solar-energy modulation and visible transmittance through the material.

We have never seen this type of calculation performed in the academic smart-window literature but we think it provides some valuable information. It does not claim to represent a 'physical' system, but what it does expose are the transmissive and modulation capabilities of VO_2 (irrespective of structure). In our view, the red boundary in subplot (**b**) of fig. 7.3 on the next page represents the 'absorptance-mediated performance limit' for all VO_2 systems. We will show later in this chapter that motheye geometries can approach this limit as they approximate 'perfect coupling' in and out of the material.

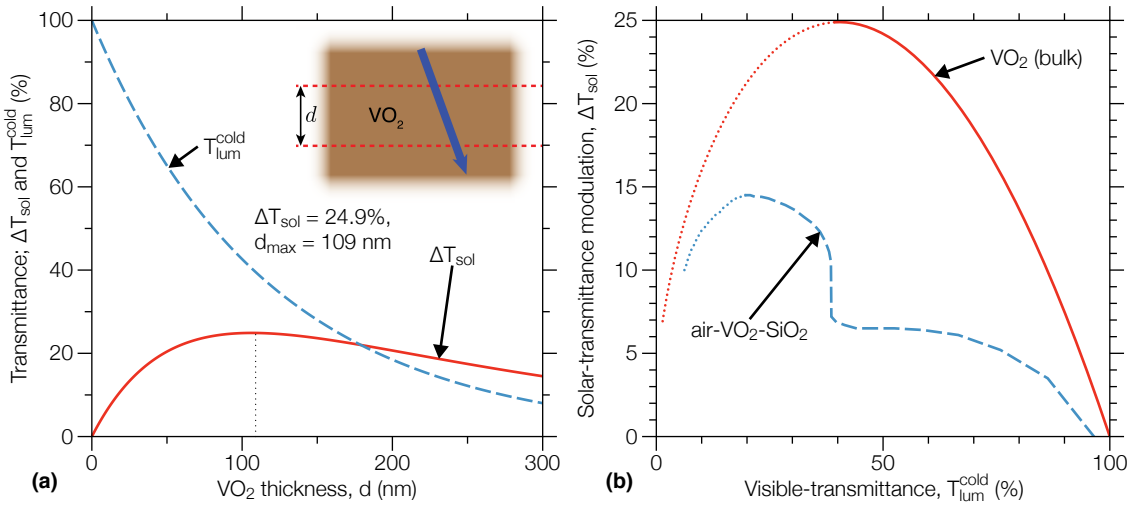

Figure 7.3: Transfer Matrix boundaries of transmittance through bulk–VO_2 (no reflections, equivalent to perfect-coupling in and out of the material). Subfigure (a) shows $T_{\text{vis}}^{\text{cold}}$ and ΔT_{sol} for different transmission-distances, whereas (b) plots these two metrics directly against one-another. The solid-red line in subplot (b) represents the absorptance-mediated performance limit for all VO_2 systems.

We plot *transmittance-per-nm distance* through bulk–VO_2 (ignoring interface reflections) in fig. 7.4. When compared with fig. 7.5 on the next page, the origin of vanadium dioxide's 'brown-ish' colour is apparent: absorption, not reflection. Transmittance-per-nm decays rapidly for wavelengths shorter than 600 nm (in both the hot and cold state). Whereas, fig. 7.5 on the following page shows a reasonably flat cold state reflection-mediated transmittance spectra at both the air–VO_2 and glass-VO_2 interfaces. The hot state reflection-mediated transmittance spectra follow a similar shape to the absorption-mediated transmittance-per-nm (suppression of wavelengths less than 600 nm) thereby exacerbating the 'brown-ish' colour at elevated temperatures.

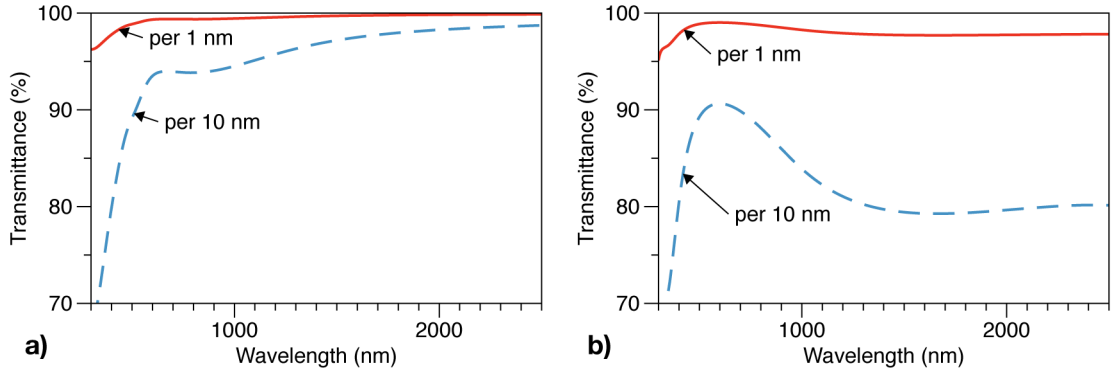

Figure 7.4: Transfer Matrix calculations of transmittance-per-nm through bulk–VO_2 (no reflection losses). Subfigure (**a**) shows the cold state transmittance per 1 nm and per 10 nm of VO_2. Subfigure (**b**) shows the hot state transmittance per 1 nm and per 10 nm of VO_2. Spectrum weighted averages of these spectra reveal that per-nm visible transmittance (in the cold state) is 99.139% and per-nm solar energy transmittance modulation is 0.696%.

7.4 Interfaces and cavities

We saw in subplot (**b**) of fig. 7.3 on page 85 the stark difference between the performance-limit for bulk–VO_2 and a planar thin-film on glass. The calculations in this section examine how interface-reflections and cavity-resonances contribute to the planar performance-limit (first discussed in section 7.2 on page 83).

We performed calculations of transmittance through each interface of the planar system, fig. 7.5: (**a**) air–VO_2 (hot state); (**b**) glass-VO_2 (hot state); (**c**) air–VO_2 (cold state); (**d**) glass-VO_2 (cold state). These calculations do not include any absorption effects i.e. they represent the Fresnel coefficients only. As expected, transmittance losses are greater for the air–VO_2 than the glass–VO_2 interface. This is due to a the refractive index discontinuity at the air–VO_2 interface being greater than that for the glass–VO_2 interface, see eq. (1.11) on page 29. Due to the time-invariance of Maxwell's equations, the same transmittance/reflectance would occur if the interfaces were reversed i.e. glass–VO_2⇔VO_2–glass and air–VO_2⇔VO_2–air.

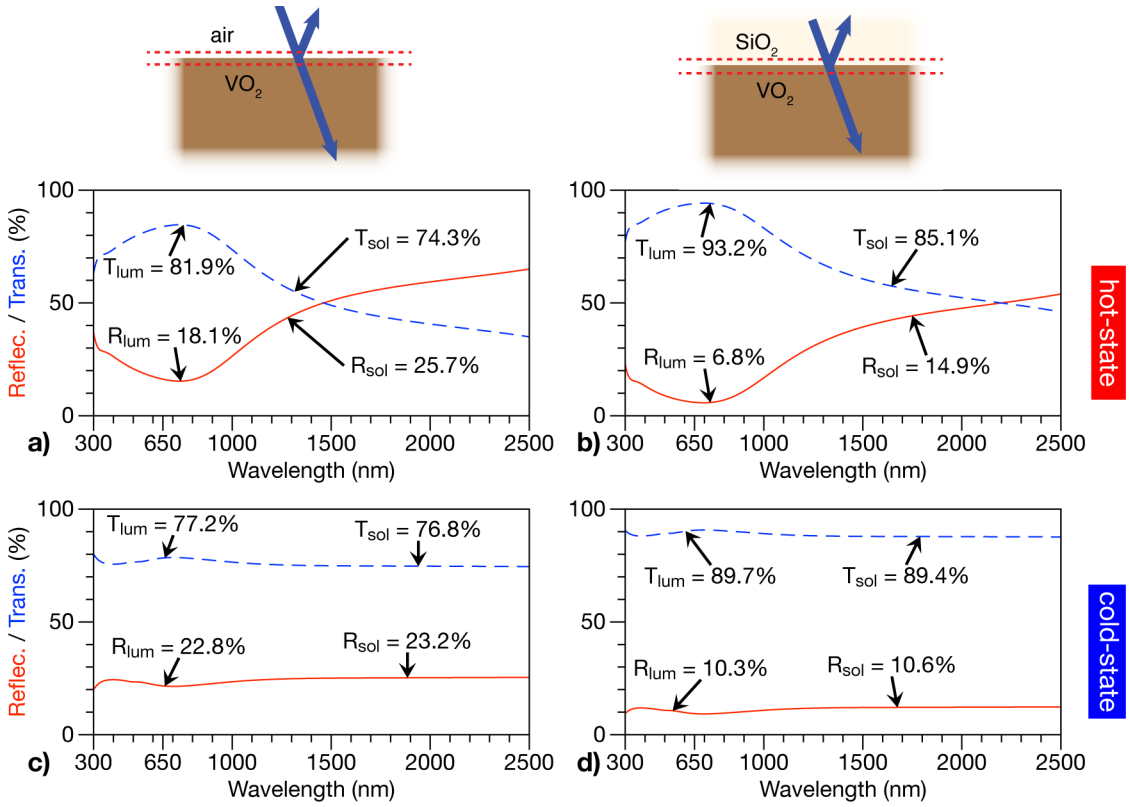

Figure 7.5: Transfer Matrix calculations of reflection-mediated transmittance through the interfaces of (**a**) air–VO_2 (hot state); (**b**) glass-VO_2 (hot state); (**c**) air–VO_2 (cold state); (**d**) glass-VO_2 (cold state). Visible and solar transmittance and reflectance values are included for each spectra. These figures explicitly show the Fresnel interface losses for a planar VO_2 smart window system.

Using the result shown in fig. 7.5 we were able to make an additional calculation: transmittance through a thin film of VO_2 on glass *ignoring cavity effects* i.e. no reflections within the VO_2 interlayer. The boundary for our 'no-cavity' model is shown in fig. 7.6 on the following page.

Each series in fig. 7.5 is labelled with the VO_2 thickness values in units of nanometers.

Blue and yellow connectors are used to map the relationship between each series e.g. a line which joins 15 nm resonant cavity VO_2, no-cavity VO_2 and 15 nm bulk–VO_2. The 'no-cavity boundary' sits between the planar model (resonant cavity) and the boundary for bulk–VO_2. It can be seen immediately that cavity resonance in the VO_2 interlayer makes no enhancement to solar transmittance modulation, ΔT_{sol} (for any thickness of VO_2).

Yellow connectors identify exactly which planar thicknesses of VO_2 contribute to improvements in visible transmittance. As an example, the resonant cavity created by a 90 nm VO_2 film enhances visible light transmittance, whereas destructive interference in a 40 nm cavity degrades visible light transmittance. Naturally, the distribution of enhancing and degrading cavity-thicknesses follow a band pattern.

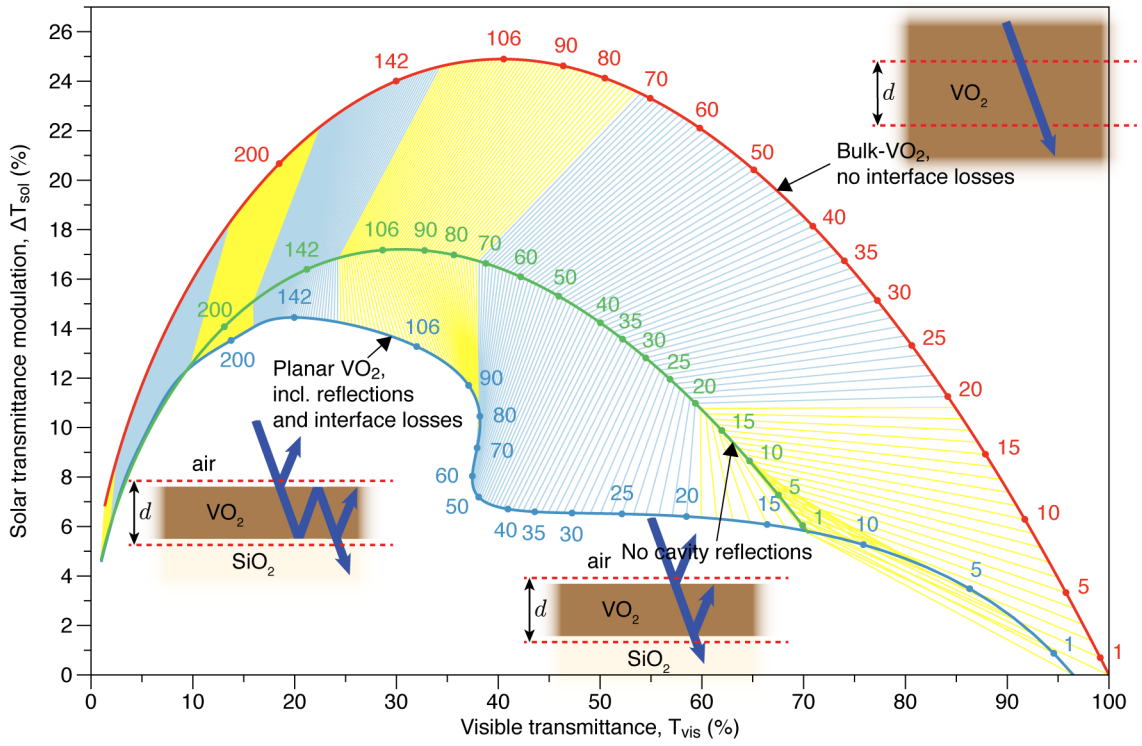

Figure 7.6: The boundary for our 'no-cavity' model (green) in which reflections within the VO_2 interlayer are excluded. The performance boundary for both bulk–VO_2 (red) and a planar VO_2 thin-film on glass (blue) are shown. Each series is labelled with VO_2 thickness values in units of nm. Connectors (yellow and blue) map the relationship between each series. Yellow connectors signify a planar VO_2 thickness that improves visible transmittance through the creation of an appropriately-tuned resonant cavity.

Further analysis of fig. 7.6 is possible. The offset between the 0 nm elements of the 'no-cavity' boundary and the 'bulk–VO_2' series is accounted for by purely interface processes i.e. it is reflectance-driven (due to the change in refractive index between the hot and cold state).

If we were to discount reflections in the VO_2 interlayer, Fresnel reflection modulation alone would account for $\Delta T_{sol} = 5.4\%$ solar transmittance modulation. Indeed, reflection-mediated modulation of solar transmittance dominates absorption-mediated modulation for VO_2 thicknesses up to 6 nm. However, for all VO_2 thicknesses greater than 6 nm, the principal mode of solar transmittance modulation (for a planar system) is absorption.

Finally, if one were to ignore cavity reflections (and all absorption processes), the

combined effect of the refractive index discontinuities at the air–VO_2 and VO_2–glass interfaces would reduce visible transmittance to $T_{\text{vis}}^{\text{cold}} = 69\%$ i.e. almost a third of visible light transmittance would be lost. However, low-absorptance in the visible region (see fig. 7.4 on page 85) and multiple reflections within the VO_2 layer overcome these visible transmittance 'Fresnel' losses for VO_2 thicknesses up to 19 nm.

7.5 Motheye Smart Windows

Motheye smart windows are significantly more complex than the planar geometries explored above. There exist many system-parameters which contribute toward the performance of such a surface: VO_2 coating-thickness; the nanocone height, rate-of-taper, average-periodicity, and finally, the nanocone-base surface-fill-factor.

In this section we present a series of Finite Difference Time Domain simulations that form the basis of a five-parameter search for the optimum geometry of a VO_2-based motheye smart window. This investigation supersedes our earlier work in which only two system-parameters were simultaneously optimised [19].

In a little more detail, the parameters included within our search were the following:

1. The **height** of the glass motheye nanostructures; this ranged from $h = 400\,\text{nm}$ to $h = 800\,\text{nm}$. Using eq. (1.12) on page 30, nanostructures of these heights are able to act in an antireflective capacity for wavelengths from $\lambda_{\text{max}} = 800\,\text{nm}$ (the entire visible spectrum and 59% of the solar spectrum, $h = 400\,\text{nm}$) up to $\lambda_{\text{max}} = 1600\,\text{nm}$ (the entire visible spectrum and 92% of the solar spectrum, $h = 800\,\text{nm}$).

2. The **average-periodicity** (or 'pitch') of the hexagonally-packed nanostructures; which ranged from $\Lambda = 50\,\text{nm}$ to $\Lambda = 300\,\text{nm}$. Using eq. (1.8) on page 27, and assuming a refractive index of $n_{\text{max}} = 2$ (based upon our effective medium approximations for VO_2-coated motheyes, fig. 7.15 on page 95), the quasi-static condition was satisfied for all wavelengths greater than 300 nm at all angles of incidence (when $\Lambda = 50\,\text{nm}$); and for all wavelengths greater than 600 nm at normal incidence (when $\Lambda = 300\,\text{nm}$).

3. The VO_2 conformal **coating thickness**; which ranged from 4 nm to 20 nm. These thicknesses were chosen to be deliberately low in order to account for the large surface area of the substrate i.e. mediate the volume of VO_2 within our simulations.

4. The nanocone-base **surface-fill-factor**; which varied between 0.5 (sparse nanocones which expose regions of the flat substrate) and 1 (high-density nanostructures, no flat interfaces).

5. The nanocone **rate-of-taper**; which is fully specified by the radius of curvature at the tip. The maximum radius of curvature for a conic-section motheye is a function of both its height and base-width (itself a function of surface-fill-factor). Therefore, in order to account for variation in these two elements of the geometry, the *index*-of-curvature was varied between 0.01 (sharp-tipped nanostructures with a fast rate-of-taper) and 1 (dome-tipped nanostructures with the slowest possible rate-of-taper).

Each parameter was varied independently; in total, approximately 25,000 different geometries were simulated. The $T_{\text{vis}}^{\text{cold}}$ and ΔT_{sol} metrics for each combination of system-parameters are presented as a cloud in fig. 7.7. The performance-boundary of the motheye cloud is highlighted in red, as are the planar and bulk–VO_2 boundaries.

The boundary was constructed by filtering-out all of the data-points that did not sit on the upper-right edge of the cloud. The remaining data-series becomes the locus of a 'conservative' performance-boundary. It cannot claim to be an absolute boundary as not all of the possible system-parameters could be checked.

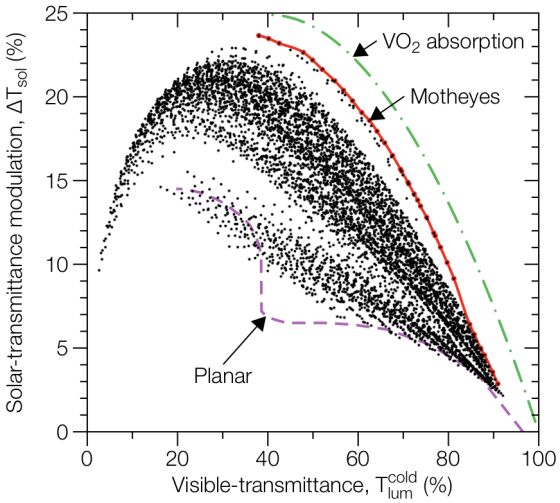

Figure 7.7: Finite Difference Time Domain simulations of VO_2-coated motheye smart window interfaces. Conic-section motheyes were simulated with: heights that varied between 400 and 800 nm; and hexagonal periodicities which ranged from 50 nm to 300 nm. The tapered nanostructures were conformal coated with VO_2 of thicknesses between 4 nm and 20 nm; the nanocone-base surface-fill-factor varied between 50% and 100%. Different rates-of-taper were simulated, ranging from 'sharp-tipped' to 'dome-tipped'. In total, approximately 25,000 different motheye geometries were simulated (black points); the performance-boundary of the motheye cloud is highlighted in red. The planar boundary (purple dashed) and bulk–VO_2 (green dot-dashed) boundaries are also shown for comparison.

The motheye performance-boundary (red line, fig. 7.7) clearly exceeds the planar limit established in the previous sections. It approaches (but does not breach) the performance-boundary of bulk–VO_2. This is because the motheye anti-reflective geometry approximates the idealised case of perfect-coupling of electromagnetic waves both in and out of the VO_2 material.

Visible transmittance through the window surface is significantly increased by the structure-induced optical-impedance-matching at the motheye interface. Meanwhile, significant reflectance-mediated solar-energy transmittance-modulation is facilitated by the interface's large surface area which supports a high volume of VO_2.

7.5.1 Geometry sets

In order to elucidate the precise combination of parameters which contribute to the highest-performing boundary cases we present fig. 7.8 on the next page. Subfigure (**a**) of fig. 7.8 on the following page shows the same motheye *cloud* as previously shown in fig. 7.7. Alongside, subfigures are provided for each of the system's parameters. All six plots share

the same y-axis. The distributions of each parameter are clearly visible. Subfigure (**g**) is an adaptation of (**a**) and shows only the *boundary* cases (as previously discussed). The additional subfigures, (**h**) to (**l**), show the filtered parameters of the system. Reading horizontally across the figure, the exact set of parameters which contribute to each of the boundary cases can be identified.

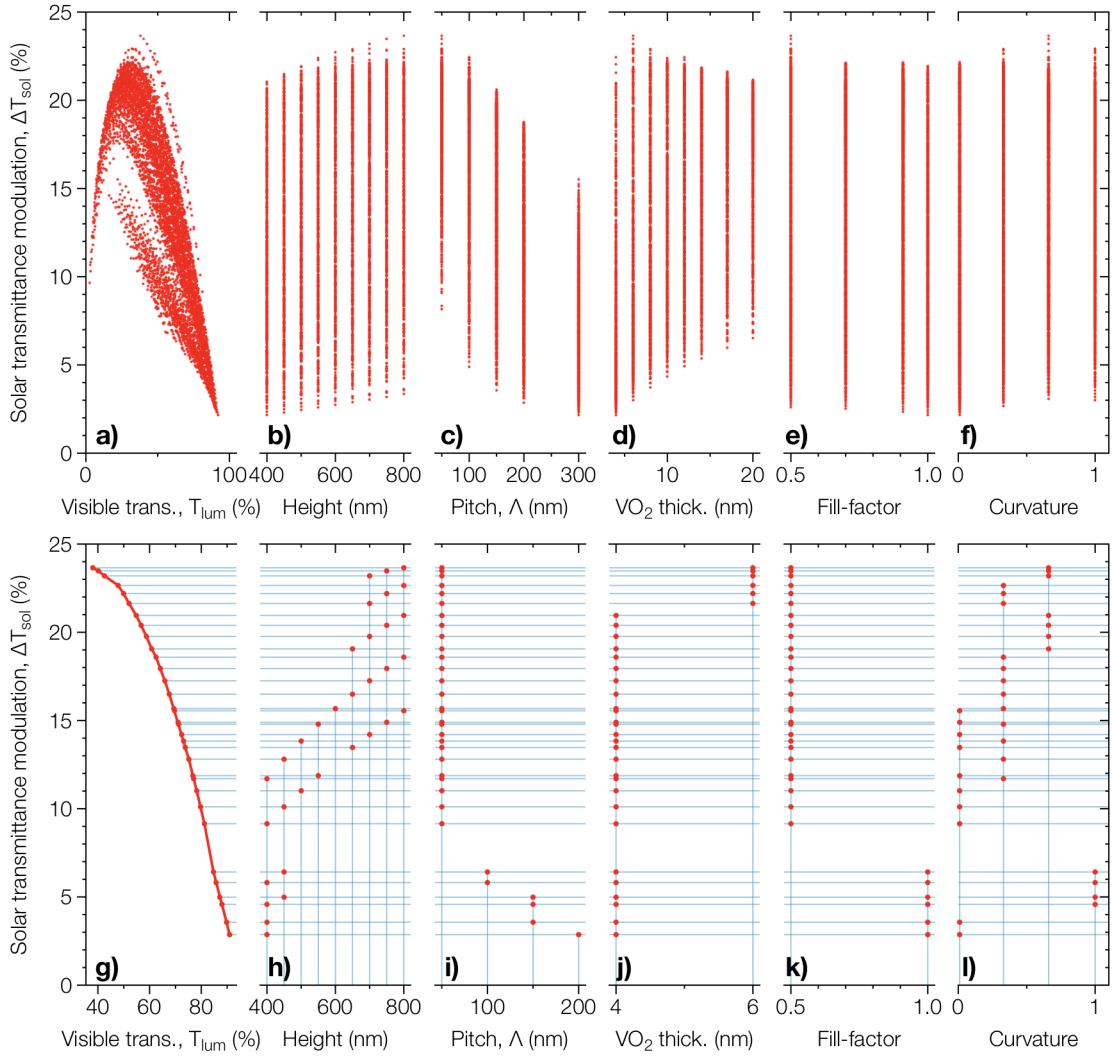

Figure 7.8: Finite Difference Time Domain simulations of approximately 25,000 different motheye smart window structure combinations (top) and the filtered 'boundary' cases (bottom). The transmittance metrics, $T_{\text{vis}}^{\text{cold}}$ and ΔT_{sol}, are show in (**a**) and (**g**). The remaining subfigures show the distribution of each independent system parameter used in our calculation sweep. All subplots share the same y-axis, ΔT_{sol}. The high-performing boundary cases from our motheye smart window Finite Difference Time Domain parameter sweep. The specific combination of system parameters which contribute to each boundary case are provided explicitly by reading horizontally across each subfigure.

Looking at fig. 7.8, some trends are immediately evident. The best solar-energy modulation is achieved by tall motheyes (between 700 and 800 nm in height), of sparsely packed motheyes (50% surface-fill-factor) with a hexagonal periodicity of 50 nm. Only the thinnest conformal coatings of VO_2 are required for optimum performance (4 to 6 nm). There is some evidence to suggest that sharp-tipped structures (with a small radius of curvature) provide the best visible transmittance. However, the optimum rate-of-taper of the nanostructures may have a secondary dependence as the boundary correlation is weak.

The results in fig. 7.8 on page 90 challenge the conventional wisdom that high aspect-ratio structures are required for motheye smart windows. Indeed, the boundary cases with the highest visible transmittance have aspect ratios as low as 2:1 (height:pitch). Shorter motheyes benefit from better visible transmittance at the expense of solar transmittance modulation.

7.5.2 Motheye design rules

The geometry parameter-sets reported in the previous section are valuable in so far as they provide the specific combinations required to achieve the highest-performing boundary cases. However, it is frequently the case that practical constraints (for example fabrication resolution) limit which geometries are accessible.

In this section we explore the performance-boundary's tolerance to geometry subsets. The data-cloud (fig. 7.7 on page 89) was filtered for each system parameter: VO_2 coating thickness, fig. 7.9; surface fill-factor, fig. 7.10 on the following page; motheye height, fig. 7.11 on page 93; rate-of-taper, fig. 7.12 on page 93 and finally the hexagonal periodicity, fig. 7.13 on page 94. Using this information, we establish generalised design rules for the motheye class of smart windows.

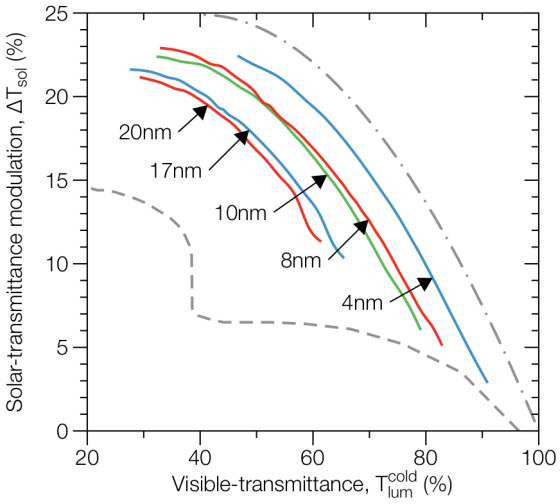

Figure 7.9: The performance-boundary's tolerance toward different thicknesses of VO_2. The data-cloud in fig. 7.7 on page 89 is filtered (by unique thickness of the VO_2 layer) and the boundaries re-extracted for each series.

From fig. 7.9 it is evident that a motheye smart window's performance is strongly dependent upon the thickness of its VO_2 coating. This does not come as a surprise. The exceptionally high surface area of the motheye interface accentuates the volume of VO_2 per-nm of deposition thickness. An uncertainty in deposition thickness leads to parasitic absorptance that degrades the performance of the surface. Ultra-thin VO_2 films ($< 4\,nm$) may go some way toward bridging the performance-gap to bulk–VO_2. This sets a significant fabrication challenge: to synthesise monoclinic crystalline VO_2 thin-films that maintain their oxidation phase over the lifetime of a window.

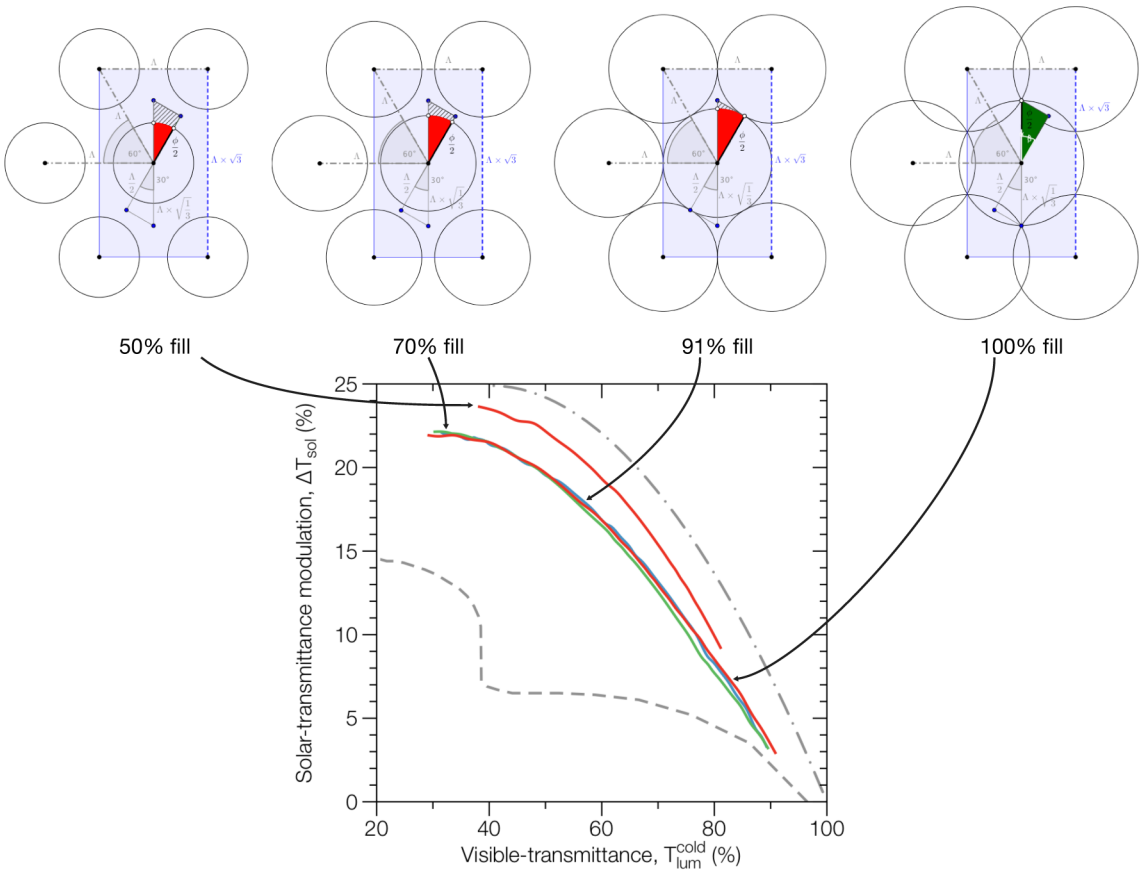

Figure 7.10: The performance-boundary's tolerance toward different surface-fill-factors. The data-cloud in fig. 7.7 on page 89 is filtered (by unique surface-fill-factors) and the boundaries re-extracted for each series.

Figure 7.10 provides an interesting and unexpected result. It shows that sparse motheye nanostructures (i.e. fill-factors that leave 50% of the surface flat) perform significantly better than dense nanostructures. This may be due to either lower volumes of VO_2 being deposited on these surfaces or a reflectance-modulation effect arising from the partially flat interface. It could be speculated that nanowire VO_2-rods represent the limit of this case. These findings merit further investigation.

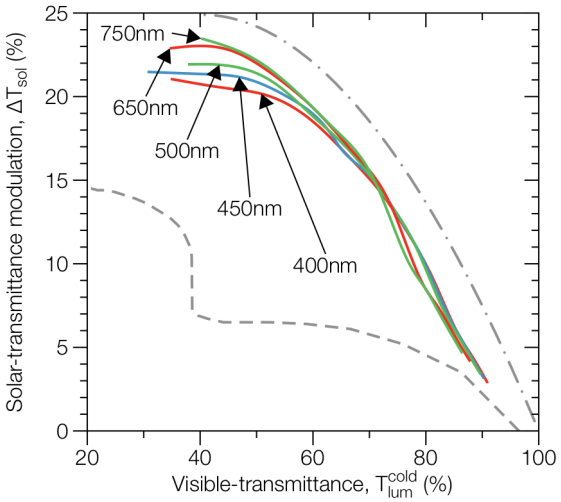

Figure 7.11: The performance-boundary's tolerance toward different motheye heights. The data-cloud in fig. 7.7 on page 89 is filtered (by unique motheye heights) and the boundaries re-extracted for each series.

Tall nanostructures modulate the most solar energy; the best performing nanostructures were 750 nm in height (see fig. 7.11). This can be attributed to both their increased anti-reflection bandwidth (as described previously) and increased surface area (which increases the volume of VO_2 on the surface).

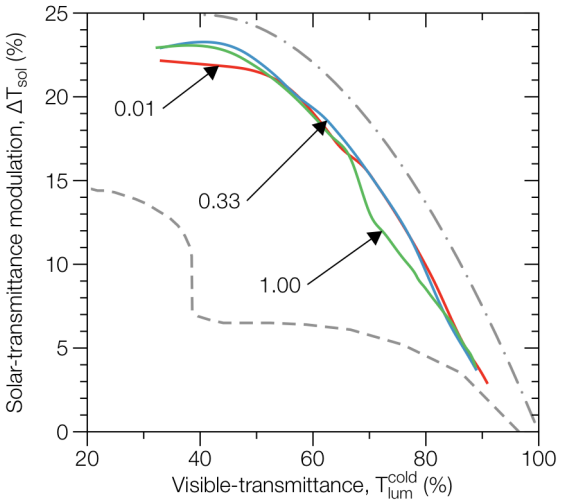

Figure 7.12: The performance-boundary's tolerance toward different nanostructure rates-of-taper. The data-cloud in fig. 7.7 on page 89 is filtered (by unique index-of-curvature) and the boundaries re-extracted for each series.

Motheye smart windows are exceptionally tolerant to variations in nanostructure's rate-of-taper. Figure 7.12 shows that performance-boundary cases exist for both sharp-tipped and dome-tipped geometries. That being said, it would appear that sharp structures do have a slight advantage over dome-tipped structures when high visible transmittance is required, and in reverse, dome-tipped structures outperform their sharper counterparts when solar transmittance modulation is of principal concern.

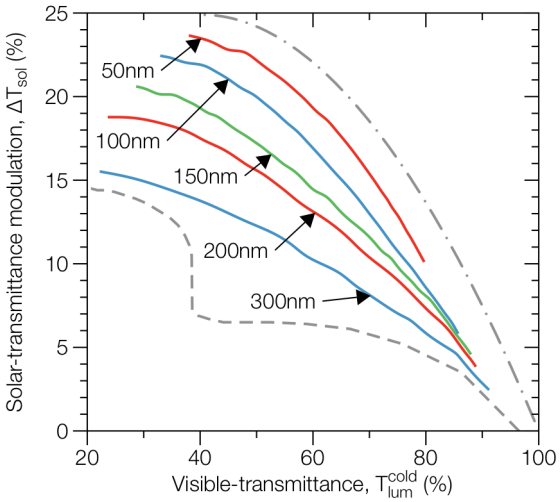

Figure 7.13: The performance-boundary tolerance of different hexagonal periodicities. The data-cloud in fig. 7.7 on page 89 is filtered (by unique pitch, Λ) and the boundaries re-extracted for each series.

Finally, the performance boundary for motheye smart windows is strongly affected by periodicity. There is a direct negative-correlation between the maximum achievable solar transmittance modulation and the periodicity of the nanostructures. For example, dense nanostructures ($\Lambda = 50\,\text{nm}$) are able to achieve ΔT_{sol} of 24% whereas the maximum achievable ΔT_{sol} of larger periodicities ($\Lambda = 300\,\text{nm}$) is less than 16%.

7.5.3 Exemplary cases

Three geometry combinations from the motheye 'performance-boundary' (established in fig. 7.7 on page 89) are shown in fig. 7.14. Subfigure (**a**) shows the transmittance spectrum for the Motheye Smart Window interface capable of transmitting the most solar energy. Whereas (**c**) is the geometry combination providing the best visible transmittance. For the specific set of parameters that contribute to each of these cases the reader is referred to fig. 7.8 on page 90.

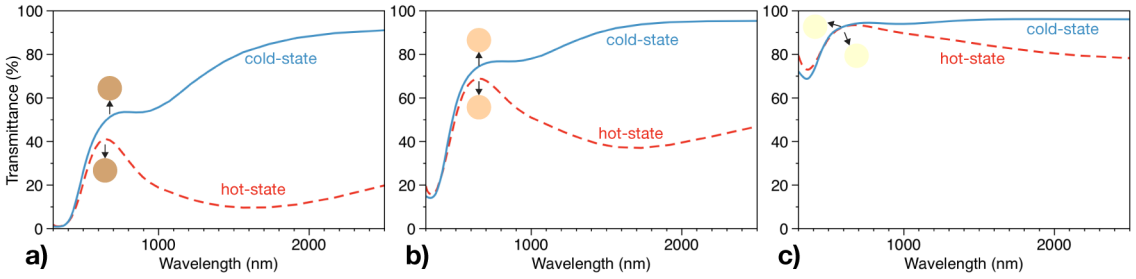

Figure 7.14: Exemplary transmittance spectra for different 'performance-limit' motheye geometries. The hot and cold state transmittance tints are displayed above. Spectrum-averaged transmittance: subfigure (**a**), $T_{\text{vis}}^{\text{cold}} = 38.0\%$ and $\Delta T_{\text{sol}} = 23.7\%$; subfigure (**b**), $T_{\text{vis}}^{\text{cold}} = 65.9\%$ and $\Delta T_{\text{sol}} = 17.2\%$; subfigure (**c**), $T_{\text{vis}}^{\text{cold}} = 90.9\%$ and $\Delta T_{\text{sol}} = 2.9\%$. The specific combinations of parameters for each of these motheye smart window interfacial geometries are provided in fig. 7.8 on page 90. The perceived visible transmittance colours for each spectrum are inset as circles.

We used eq. (1.9) on page 28 to calculate the effective refractive index profiles for each

of the three exemplary geometries, see fig. 7.15. The surface-fill-factors for (**a**) and (**b**) are both 50% and therefore flat area of the substrate cause the 'jump' at $z = 0\,\text{nm}$. The smoothest refractive index profile is exhibited in (**c**), there are two reasons for this. Firstly, the thickness of VO_2 (4 nm) is very low. Secondly, the surface fill-factor for this geometry is 100% i.e. there are no exposed flat regions on the interface.

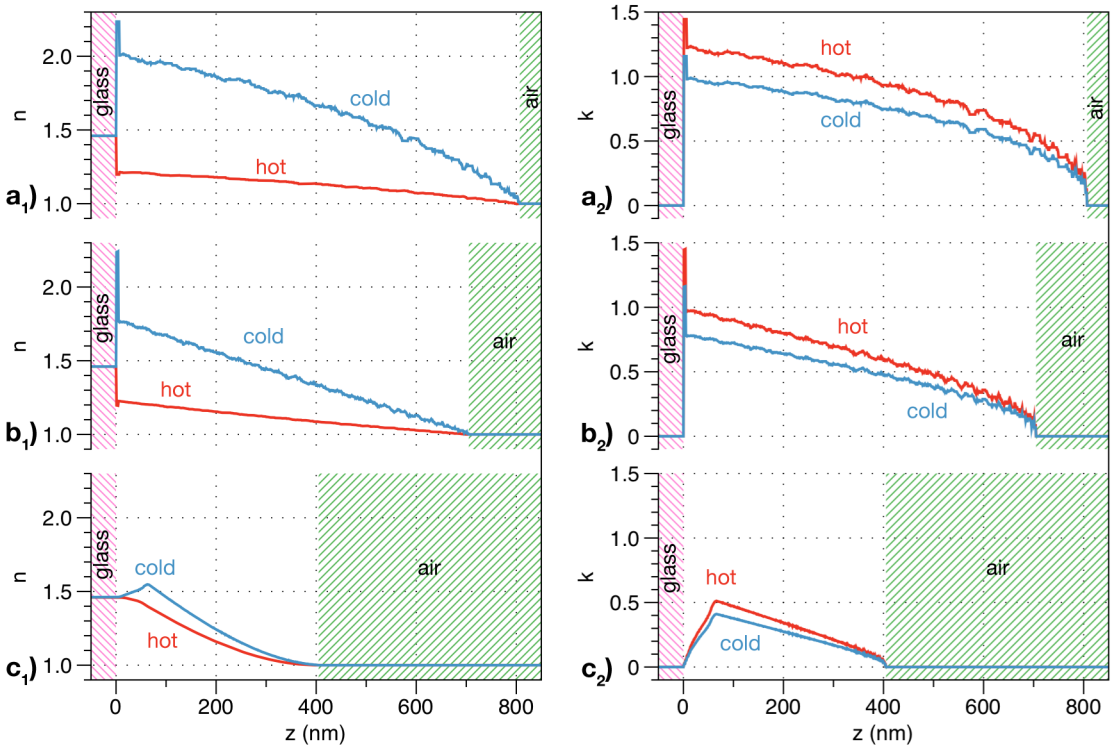

Figure 7.15: Effective medium approximations of the refractive index (n) and extinction coefficient (k) for the three 'performance-limit' motheye geometries shown in fig. 7.14 on page 94. The pink-hatched region represents the bulk substrate (glass), whilst the green-hatched region represent air.

7.6 Conclusions

In conclusion, our analysis of planar VO_2 systems has exposed the fundamental mechanisms which contribute to dynamic, spectrally-selective smart window behaviour. We are not aware of any previous studies which go into the same depth with regard to modulation mechanics and cavity resonance.

This technique is not just limited to assessing geometrical smart window systems. As an extension of this work, it would be of interest to re-perform these boundary calculations for doped VO_2 films. For example, the common presumption that low-levels of tungsten doping (W:VO_2, in order to lower the metal-to-semiconductor transition temperature) does not adversely affect the refractive index could be tested directly. In addition, routes toward engineering the refractive index for enhanced visible transmission through magnesium doping (Mg:VO_2) could benefit from this style of analysis.

The design rules for motheye smart windows we established in section 7.5.2 on page 91 represent our key result in this chapter. They were valuable for informing many of our choices in the fabrication process described in the following chapter. As an example of

this, knowing that high-performing motheye interfaces do not require the nanostructures to be taller than approximately 500 nm (from fig. 7.11 on page 93) allowed us to develop processes without the need for high material etch contrasts. Further still, our choice between fabrication techniques placed constraints on the periodicity of the nanostructures we were able to fabricate. However, using fig. 7.13 on page 94 we were able to strike an appropriate balance between practicality and performance in selecting solutions of monodisperse colloidal nanospheres for the self-assembled lithographic masks, for example.

Chapter 8

Fabrication of motheye nanostructures

8.1 Top-down via Electron-Beam Lithography: motheye nanostructures over small areas

Our first approach toward fabricating motheye nanostructures in glass was to use electron-beam lithography, a 'top-down' method. The method involved writing a pattern into a resist material that is then be used to define a 'hard-mask' for subsequent reactive-ion etching. See section 1.4 on page 38 for our discussion regarding subtractive methods for creating motheye nanostructures from a bulk material.

8.1.1 Writing on non-conductive substrates

Charging occurs as an electron-beam is directed at a non-conductive surface. When performing Scanning Electron Microscopy on glass, it is common practice to pre-deposit a thin layer of gold onto the surface in order to dissipate charge. Our first challenge was to develop a method by which our electron-beam resist poly(methyl methacrylate) (PMMA) could be exposed on a non-conductive substrate (quartz). The three schemes we investigated to do this are shown in fig. 8.1 on the next page. The choice between which dictates the later stages of the lithography sequence.

When exposed correctly, PMMA acts as a 'positive tone' resist; regions exposed to the electron-beam can be 'developed'/removed using a diluted solution of methyl isobutyl ketone (MIBK). PMMA is generally considered to provide a higher-resolution than the alternative ZEP resist and has been shown to be capable of forming 20 nm features; perfectly adequate for motheye applications [231].

Conductive polymer, PEDOT:PSS

Our first approach was to first spin-coat our PMMA resist and then subsequently spin-coat a thin layer of conductive polymer; poly(3,4- ethyl enedioxythiophene):poly(styrenesulfonate) (PEDOT:PSS), see subfigure (**a**) in fig. 8.1 on the following page. This charge-suppression technique has been previously reported [86].

The advantage of using PEDOT:PSS as a conductive top-layer is that it is water-soluble

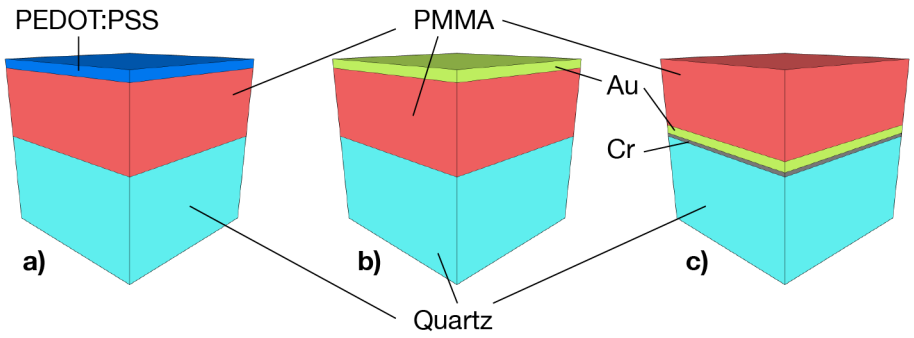

Figure 8.1: Three different exposure schemes for electron-beam writing on quartz. Subfigure (**a**) uses a layer of conductive polymer (PEDOT:PSS) on top of the PMMA resist whereas subfigure (**b**) shows a similar configuration with the overlayer being replaced by gold (Au). Subfigure (**c**) comprises of a metallic underlayer (gold on chrome) that sits between the PMMA resist and the substrate.

whereas PMMA is not. The post-exposure lithography sequence would have been to first remove the PEDOT:PSS using deionized water and then develop the exposed pattern in a solution of MIBK. This would be followed by a physical vapour deposition (line-of-sight) of a hard-mask and then a solvent lift-off before being etched in an RIE system.

However, our experience with PEDOT:PSS was that it was unable to suppress the charging effects on our quartz substrates (even at low beam-currents) and so we were unable to perform satisfactory exposures. Therefore, this method of charge-suppression was abandoned after several failed attempts.

Metallic over-layer

Following our experience with PEDOT:PSS, we looked for an alternative (more conductive) over-layer and decided to try using a thin layer of gold (Au $\approx 5\,\text{nm}$), see subfigure (**b**) in fig. 8.1.

Charging effects were not observed during the exposure process. However, we found that forward scattering of the electrons (after passing through, and interacting with, the Au layer) severely limited the exposure resolution, see fig. 8.2 on the following page.

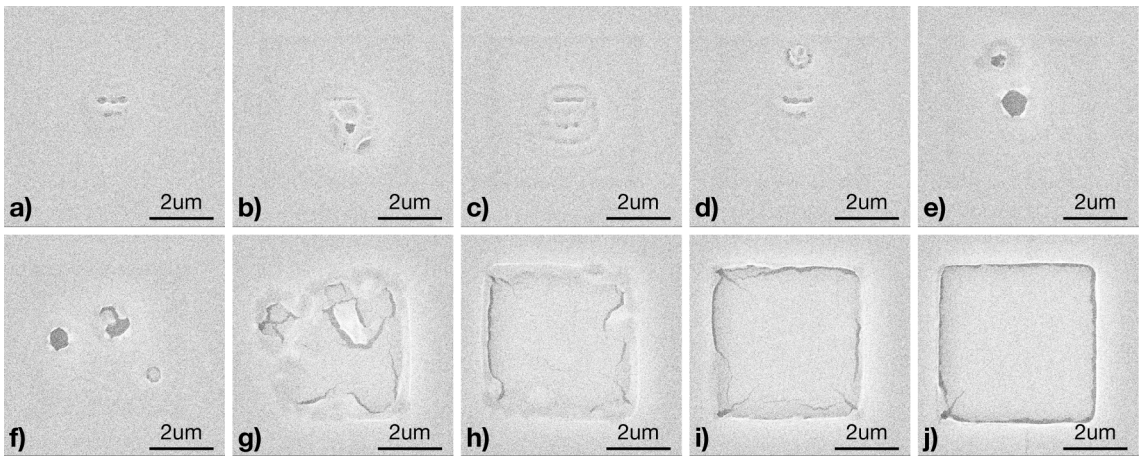

Figure 8.2: Post-development SEM images of a patterned PMMA mask. Patterns of circle-arrays ($5 \times 5\,\mu$m, $\Lambda = 130\,$nm) were exposed using an electron beam with a 10 kV accelerating potential. Increasing dosages/dwell-times for the same pattern are shown in subfigures (**a**)–(**j**). Charging (due to the non-conductive quartz substrate) was mitigated by using a thin Au over-layer, see subfigure (**b**) in fig. 8.1 on page 98. Due to forward scattering of the electrons following their interaction with the gold-layer, the high-resolution patterns failed to write correctly. However, the low-resolution bounding-box for the circle array is visible; particularly for high-dosages, see subfigure (**j**).

Metallic under-layers

Our third and final strategy for exposing high-resolution patterns onto a non-conductive substrate employed metallic *under*-layers, see subfigure (**c**) in fig. 8.1 on page 98. The advantage to using an under-layer is that the resolution-degrading effects of forward scattering (shown for metallic over-layers in fig. 8.2) are avoided and only back scattering electrons degrade the resolution.

The substrate was prepared by first evaporating a thin layer of chrome ($\approx 2\,$nm) followed immediately (without breaking vacuum) by the deposition of a thin layer of gold ($\approx 5\,$nm). The Cr-layer acted as an 'adhesive' between the Au-layer and the substrate – this was important as adhesion between thermally-evaporated Au and glass is known to be very weak and could otherwise lead to delamination of the patterned resist during a subsequent process step. The drawback of using a chrome under-layer is that it acts as a highly-effective hard-mask during the final reactive ion etching process. Therefore, its thickness was kept to an absolute minimum.

This charge-mitigation scheme worked well and we were able to correctly expose and develop hexagonal arrays of circles with a periodicity of $\Lambda = 130\,$nm and a range of diameters/fill-factors, see fig. 8.3 on the next page. This periodicity was chosen based upon the design rules established in the previous chapter and could be expected to form motheyes with a maximum solar-energy transmittance modulation of approximately 22%, see fig. 7.13 on page 94.

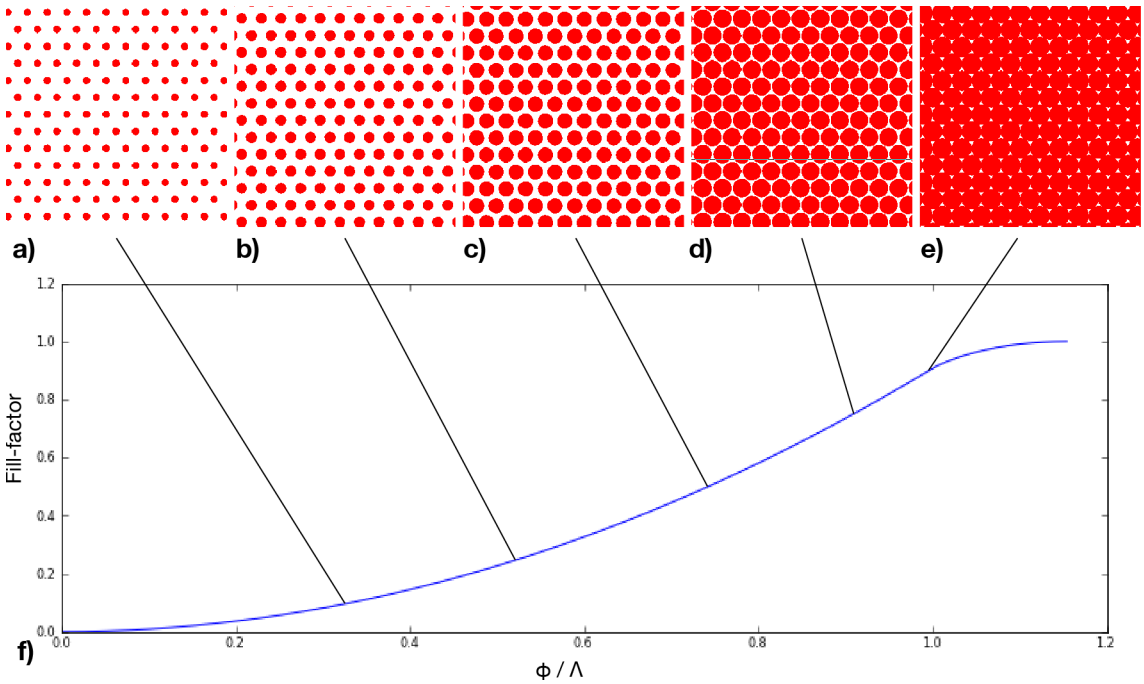

Figure 8.3: Examples of the electron-beam mask designs for hexagonal arrays of circles ($\Lambda = 130\,\text{nm}$). Subfigures (**a**)–(**e**) show circle-arrays with a range of diameters (ϕ) leading to fill-factors of (from left to right): 10%, 25%, 50%, 75% and 100%. Subfigure (**f**) shows the circle-diameter to periodicity ratio relationship ($\frac{\phi}{\Lambda}$) and fill-factor for hexagonal arrays.

8.1.2 Fast exposures over large areas: reducing pattern dimensionality

Having established a method for writing high-resolution patterns onto a non-conductive substrate, our next milestone was to do the same but over a large-area. In order to make a proof-of-principal motheye interface that could be characterised for both its optical and wetting properties, our approximate minimum target-area was $3 \times 3\,\text{mm}^2$.

We simulated the writing process in order to calculate the write-time per mm^2 for a hexagonal array of circles with a surface fill-factor of 50% requiring an area-dose of 100 uAs cm$^-$1 using a 10 keV accelerating potential and a 30 μm aperture. On the electron beam system available to us (Raith-150), these beam parameters were known to contribute to a beam-current of approximately 175 pA. Our calculation indicated that writing a single 1×1 mm^2 area would take an impressive 14 days and 14 hours: therefore, a 3×3 mm^2 area would take an excessive 4 months to complete.

Upon inspection, it was noticed that 98.6% of the projected write-time was devoted to *calculating* the electron-beam's movement sequence. Only 1.43% of the time was devoted to exposure/'dwell-time' (the remainder was movement-time/'beam-blanking'). The reason for the seemingly disproportionate allocation of time is that the exposure required decomposition of each and every circle-element in the design. This was the case even when the design-file efficiently referenced only a single unit-cell that was tiled over a $100 \times 100\,\mu\text{m}$ write-field that was then in turn tiled over the entire exposure region.

The only method to mitigate the computational overheads for writing circle-arrays would have been to modify the electron-beam system; upgrading it with a module that efficiently handled periodic designs. However, doing so would was outside of the project's budget.

Our solution was to alter the nature of our design files entirely. Instead of specifying two-dimensional objects, we switched to using zero-dimensional dots. The computational advantage is immediately apparent: no decomposition of the design file is required as the location of each write-feature is directly specified. The exposure of a 'circle' is possible as the electron beam has a finite diameter and back-scattering from the substrate and underlying metallic layer doses nearby regions of the resist. Therefore, the diameter of the circle can be controlled directly from the dot-dose, see fig. 8.4.

In contrast to our simulations of the writing process for two-dimensional circle-arrays, the write-time per mm for an array of zero-dimensional dots was very short. We assumed the same beam-parameters as above and a dot-dose of 0.1 pAs. This resulted in a write-time for a $1 \times 1\,\mathrm{mm}^2$ region of 11 hours and 16 minutes; a factor of 31 improvement. The fraction of calculation-time was reduced from 98.6% to less than 5%. In addition, the beam-blanking to dwell-time ratio was reduced from 25% to 5.3% as the movement-path reduced.

Due to the reduced dosing-efficiency of exposing a two-dimensional circle via back-scattering, the dwell-time for zero-dimensional dot -patterns was approximately 2.16 times longer than for the exposure of an equivalent two-dimensional circle-patterns. In total, we predicted that the exposure of a $3 \times 3\,\mathrm{mm}^2$ dot-pattern would take less than 5 days. An exposure of this length of time remains impractical, ,not just due to the cost and availability of an electron beam system, due to the tendency for the electron beam to de-focus over several hours of operation.

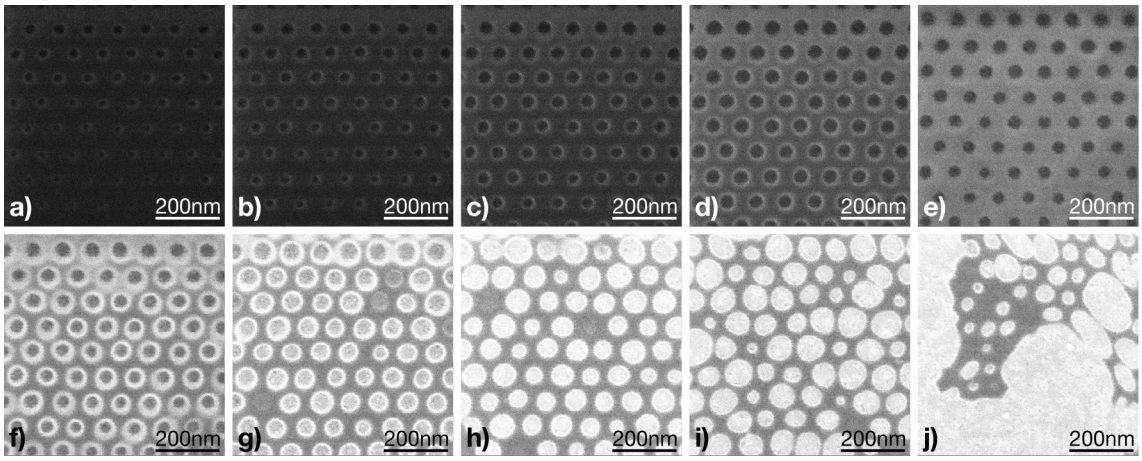

Figure 8.4: Arrays of hexagonal 'circles'/holes produced via the exposure of 'dots' with increasing dwell-times/dosages, (**a**)–(**j**). Subfigures (**h**)–(**j**) have been over-exposed and have therefore been distorted during the development process.

8.1.3 Metallic inversion

Following the post-exposure development of the PMMA resist, the pattern of holes was converted into an array of Cr dots via a lift-off process. A 30 nm chrome layer was deposited using an Edwards A-306 thermal evaporator in order to produce 750 nm-tall motheye features after reactive ion etching. This thickness was chosen based upon the conservative assumption of a reactive ion selectivity of Cr:SiO_2 being 25:1 (derived from a series of step-tests). The target height of 750 nm was based upon our simulation results

which showed that motheye structures with these dimensions could achieve solar-energy transmittance-modulation of almost 24%, see fig. 7.11 on page 93. Lift-off was achieved by immersing the sample in acetone and sonicating for 20 minutes, see subfigure (**c**) in fig. 8.6 on the next page.

8.1.4 Reactive Ion Etching: varied diameter-dose

The process of etching a tapered motheye nanostructure requires the etch processes to include simultaneous vertical and horizontal components i.e. deep etch into the SiO_2 substrate whilst under-cutting and shrinking the etch-mask. The diameter of the chrome islands is therefore a key factor; its optimum value likely to be somewhere in the range 0.5Λ–0.9Λ giving rise to fill-factors in the region of 30%–80%, see subfigure (**f**) in fig. 8.3 on page 100.

In order to optimise the diameter of the Cr-island etch-mask as a function of etch time we created an electron-beam dot-dose pattern that produced a controlled range of diameters, see fig. 8.5.

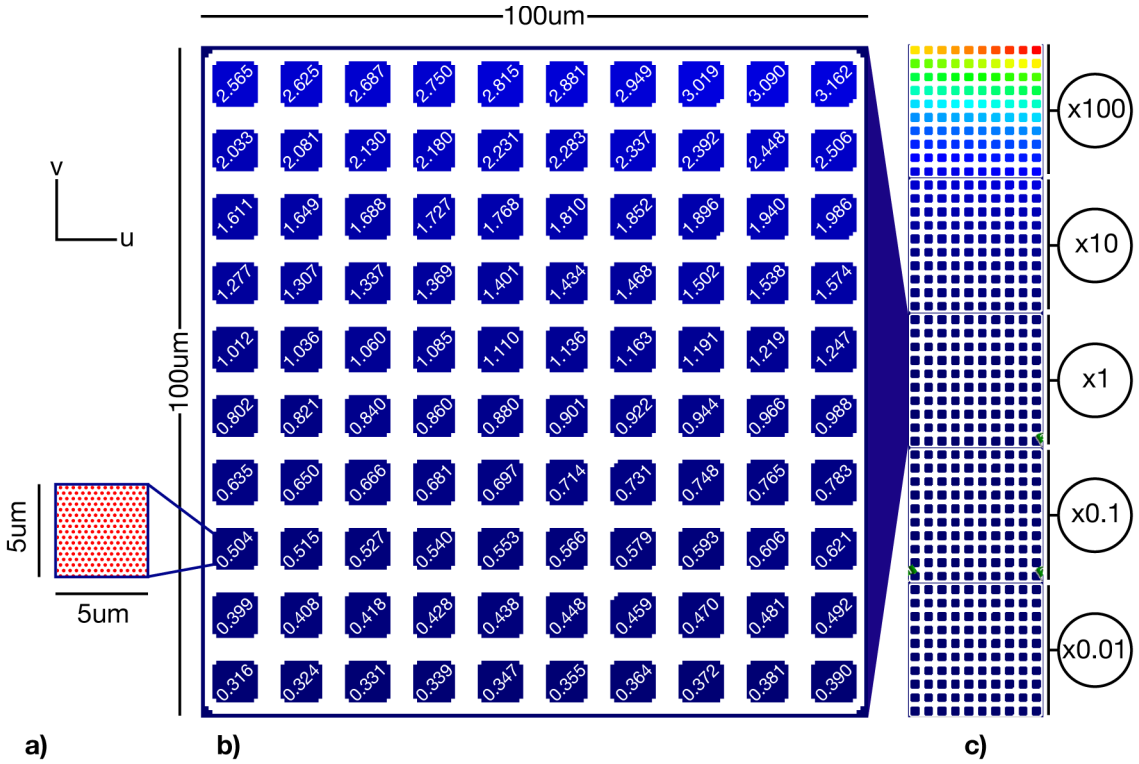

Figure 8.5: A dot-dose exposure test pattern used to optimise the diameters of the etch-mask Cr-islands as a function of etch time. This is single write-field ($100 \times 100\,\mu$m), the full pattern is shown in fig. 8.6 on the next page; each write-field contains 100 different $5 \times 5\,\mu$m dot-matrices. Within a single write-field the dot-dose is varied logarithmically by a factor of 10, from 0.316 to 3.162. Relative factor: column-to-column, $u = 1.024$; row-to-row, $v = 1.262$.

Our reactive ion etch process used CHF_3 (flow-rate 30 sccm) and O_2 (flow-rate 10 sccm) in a chamber held at 30 mTorr and 20 °C. An RF-power of 200 W was used to strike a plasma and accelerate the reactive species vertically, toward the sample. Our etch rates (based upon the step-tests referred to previously) for SiO_2 was 50 nm min^{-1} and

2 nm min^{-1} for the Cr hard-mask. Therefore, our etch process was allowed to run for 15 minutes in order to reach the point at which complete removal of the 30 nm-thick Cr hard-mask could be expected. Upon examination of the sample using a high-resolution Scanning Electron Microscope, we found that a dot-dose of 0.00372 pAs gave rise to the best formed motheyes, see fig. 8.6.

We found that both higher chamber-pressure or increased oxygen flow-rate reduced the aspect ratio of the final nanostructures. The former, due to undercutting of the mask by the increased isotropy of a 50 mTorr etch, for example. The latter (higher oxygen content), degraded the etch by stripping-away the side-wall passivating polymers that form as a byproduct of the reaction between CHF_3 ions and SiO_2.

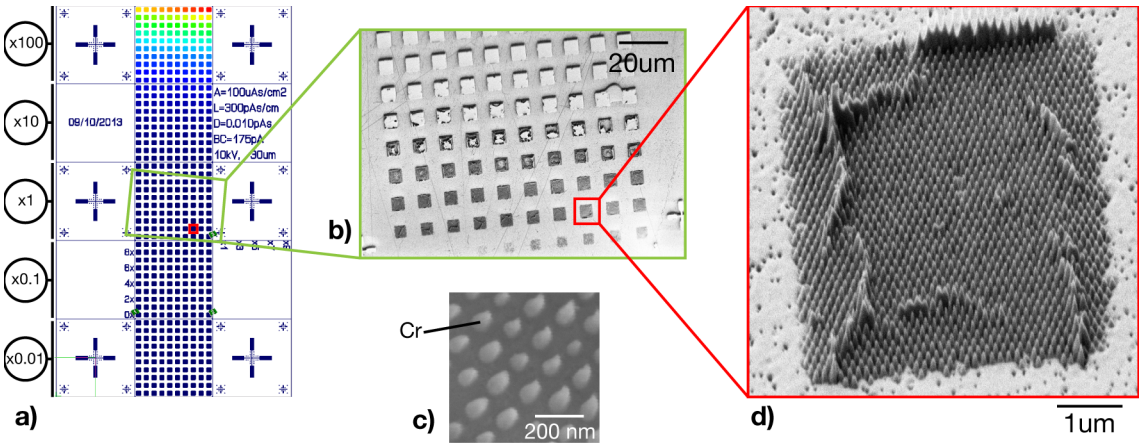

Figure 8.6: Subfigure (**a**): the dot-dose exposure test-pattern used to optimise the diameters of the etch-mask Cr-islands. Each write-field (shown in detail in fig. 8.5 on page 102) is repeated five times with an additional 10× dose-factor applied to each subsequent repeat; full pattern has a dynamic range of 10^6. Subfigures (**b**) and (**d**) show that the optimum motheye nanostructures were formed by a dot-dose of 0.00372 pAs. An SEM image of the Cr hard-mask associated with this dot-dose is shown inset as subfigure (**c**).

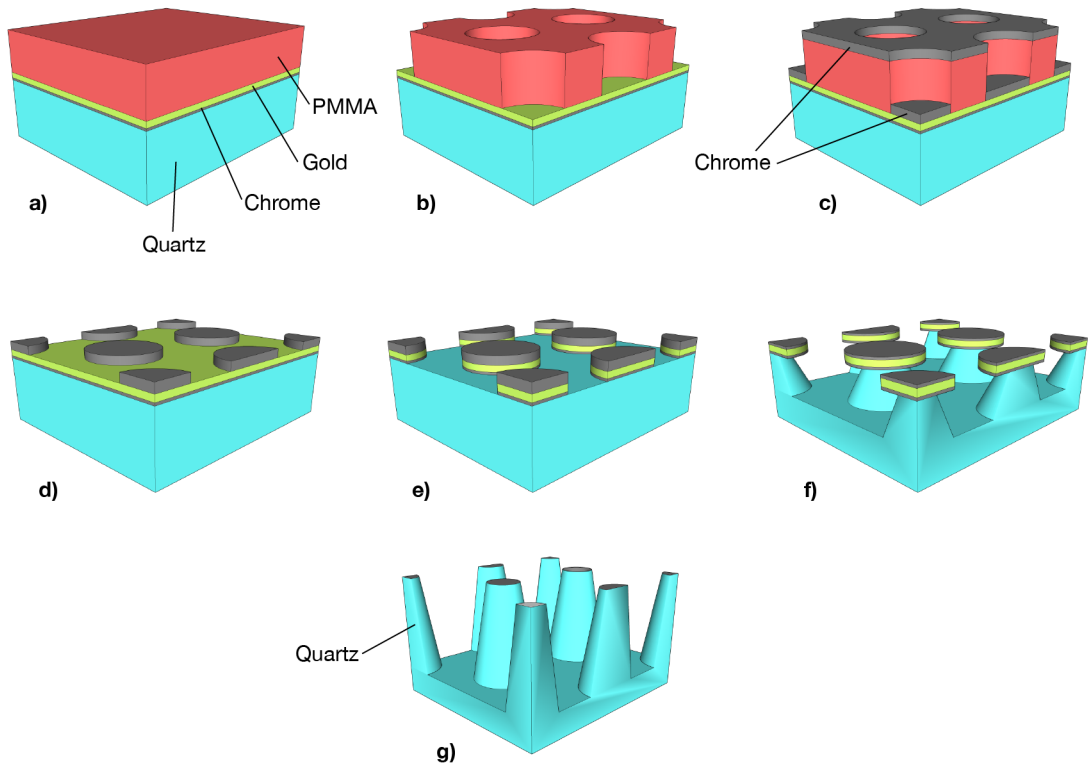

Figure 8.7: The fabrication sequence developed for the production of motheye nanostructures in glass via 'top-down' electron beam lithography: (**a**) Evaporation of thin Cr/Au layer for charge-dissipation before spinning the PMMA resist; (**b**) exposure of a dot-array and its development to form a hexagonal array of holes; (**c**) evaporation of Cr hard-mask; (**d**) solvent lift-off of patterned resist; (**e**) initial stage of RIE removes the thin Cr/Au layer leaving behind islands of tri-layer (Cr/Au/Cr) hard-mask; (**f**) undercutting during the reactive ion etching process; (**g**) the remaining motheye nanostructure left behind after the hard-mask material has been fully etched-away.

We had established a 'top-down' sequence by which motheye nanostructures could be fabricated in quartz using electron beam lithography, see fig. 8.7. However, the challenge was for us to repeat this process on a larger scale. Methods to replicate the nanostructures from a 'master' using techniques such as nanoimprint lithography were not available to us at this time.

Our principal bottle-neck was the 'serial' nature of pattern writing using an electron beam. Therefore at this point, our attention turned toward 'parallel' techniques for creating large-area nanostructured masks that could be used in a reactive ion etching process similar to the one described above.

8.2 Bottom-up via Colloidal Nanosphere Lithography: motheye nanostructures over large areas

We began working with colloidal nanosphere solutions following the example of researchers who had shown that nanosphere-monolayers can form highly-versatile lithographic masks [232]. Aqueous solutions of monodisperse polystyrene/latex nanospheres are commercially available and offer an adequate lithographic material-contrast to glass.

8.2.1 Evaporative assembly

Our first approach toward depositing nanosphere-monolayers on glass was simple: to pipette a droplet of colloidal solution onto the substrate and allow it to evaporate. The key challenge to this technique is the 'coffee-stain' effect whereby Marangoni flow causes sedimentation of the nanospheres at the droplet's outer ring [233]. In order to overcome this, we attempted to evaporate the host solution at: different temperatures (4–20 °C); in the presence of a solvent (ethanol) atmosphere; with surfactants (Triton X-100); and solvents (ethanol) added to the host solution. Some of these techniques were successful in mitigating the macroscopic effects of 'coffee-staining', see subfigure (**c**) in fig. 8.8. However, on a microscopic scale, the patterns formed by the nanospheres upon drying were similar, examples of which can be seen in fig. 8.8. Instead of forming a close-packed monolayer, the nanospheres formed a 'delta' pattern; leaving micron-sized areas on the substrate empty.

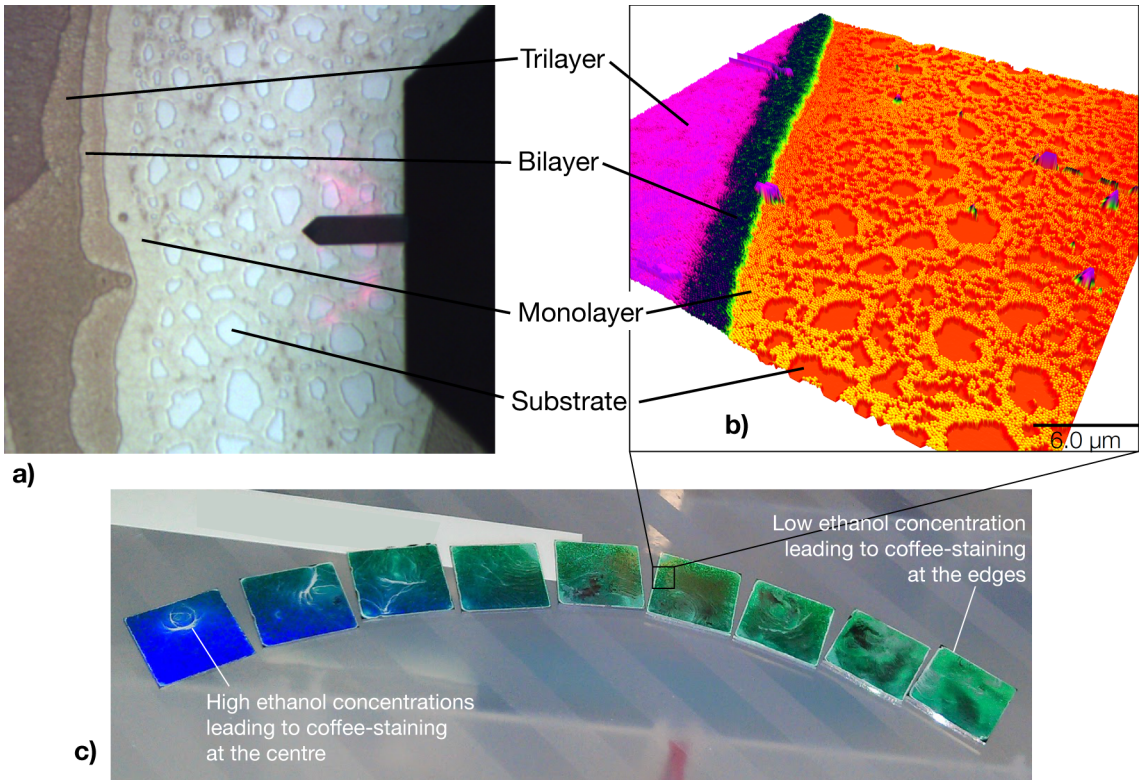

Figure 8.8: Evaporative assembly of polystyrene colloidal nanospheres. The 'coffee-stain' effect can be seen on the left-side, and the 'delta' monolayer formation on the right-side of each image. Subfigure (**a**), an image taken using an optical microscope mounted on an AFM head. subfigure (**b**), an atomic force scan of the same sample revealing the height of monolayers, bi-layers and tri-layers. Subfigure (**c**), diffraction from 400 nm-diameter polystyrene nanospheres monolayers — their microscopic non-closepacked 'delta' formation is not evident at this scale.

8.2.2 Trapping monolayers

In order to achieve monolayers of close-packed nanospheres we turned toward the Langmuir methods, discussed previously in section 1.4.2 on page 42. To recap, these techniques exploit the high surface-tension of water which confines the nanospheres to a two-dimensional plane in which they are able to undergo van der Waals-mediated self-assembly.

Initially, we used a manual Langmuir-Schaefer technique to deposit the nanosphere monolayers. This involves raising the horizontal glass substrate vertically through the surface. For these depositions we used a Petri-dish filled with deionized water (the subphase), see subfigure (**a**) in fig. 8.9. The floating monolayer was formed on the surface of the water by adding droplets of colloidal solution mixed with ethanol in order to induce a surface-tension gradient. After allowing the monolayer to nucleate into a close-packed film, tweezers were used to pull each substrate through the surface. Disturbances to the surface often caused the monolayer to fragment, see subfigure (**b**) in fig. 8.9.

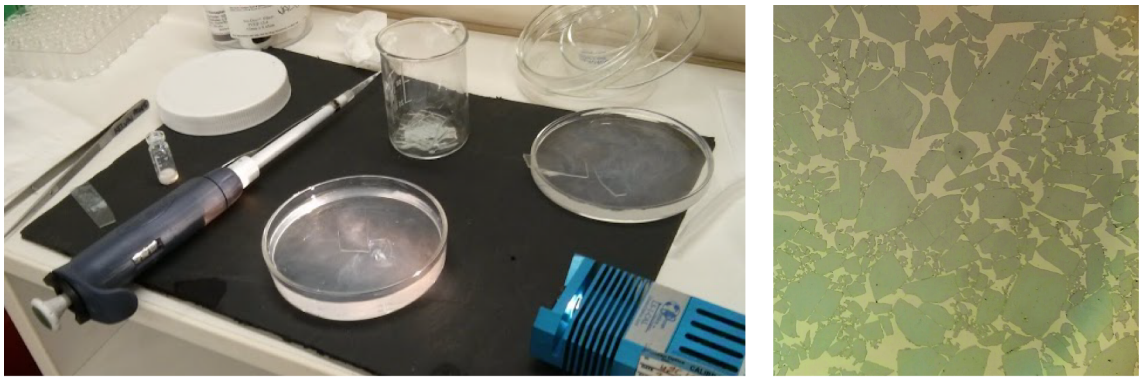

a) **b)**

Figure 8.9: The manual Langmuir-Schaefer technique. Subfigure (**a**), a Petri dish filled with deionized water; substrates sit beneath the surface and are raised through it using tweezers in order to deposit the monolayers floating on the surface. Subfigure (**b**), fragmentation of a monolayer deposited using this technique due to deformation of the water's surface and vibrations caused during the manual deposition.

In order to transfer the floating monolayers without fragmentation occurring we switched to a Langmuir-Blodgett deposition method, shown in fig. 8.10 on the next page. This variation of the technique affords two key benefits. Firstly, the floating monolayer is compressed by two barriers in order to form a highly-dense state of packing. Secondly, the vertical withdrawal of the substrate causes minimal distortion of the surface and can be fully automated.

An example of a close-packed nanosphere monolayer created using the automated Langmuir-Blodgett deposition method is shown in fig. 8.11 on the following page.A colloidal solution of 200 nm-diameter nanospheres in water (2% weight concentration) was mixed with ethanol in a ratio of 1:2 (colloidal-solution:ethanol). This was added dropwise to a glass slide that entered the Langmuir trough at a shallow angle in order to minimise vertical momentum that could cause sedimentation of the nanospheres into the subphase. The monolayer was allowed to stabilise for 10 minutes before being compressed at a rate of 2 cm min^{-1}. At full-compression, withdrawal of the substrate began and continued at a speed of 1 mm min^{-1} thereby taking one hour to cover the glass slide (the top 12 mm of the sample could not be coated as the trough's well had insufficient vertical depth).

8.2.3 Self-assembled lithographic masks

We explored two different approaches toward using self-assembled nanosphere monolayers to define an etching mask. The first approach inverted the nanosphere monolayer into a chrome hard-mask in order to exploit the strong glass-to-chrome selectivity of the reactive

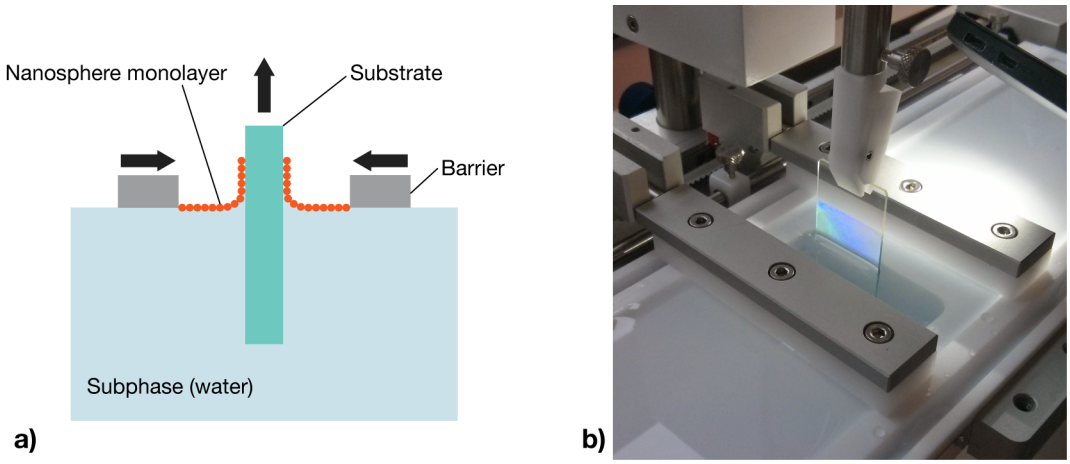

Figure 8.10: The Langmuir-Blodgett technique for depositing floating monolayers onto a solid substrate. Subfigure (**a**), a schematic of the process: barriers compress the nanospheres into a close-packed configuration and following this the substrate is withdrawn vertically. Subfigure (**b**), a photograph of our one of our depositions in which a monolayer of 400 nm-diameter nanospheres can be seen to cause a coloured diffraction effect on the substrate after withdrawal.

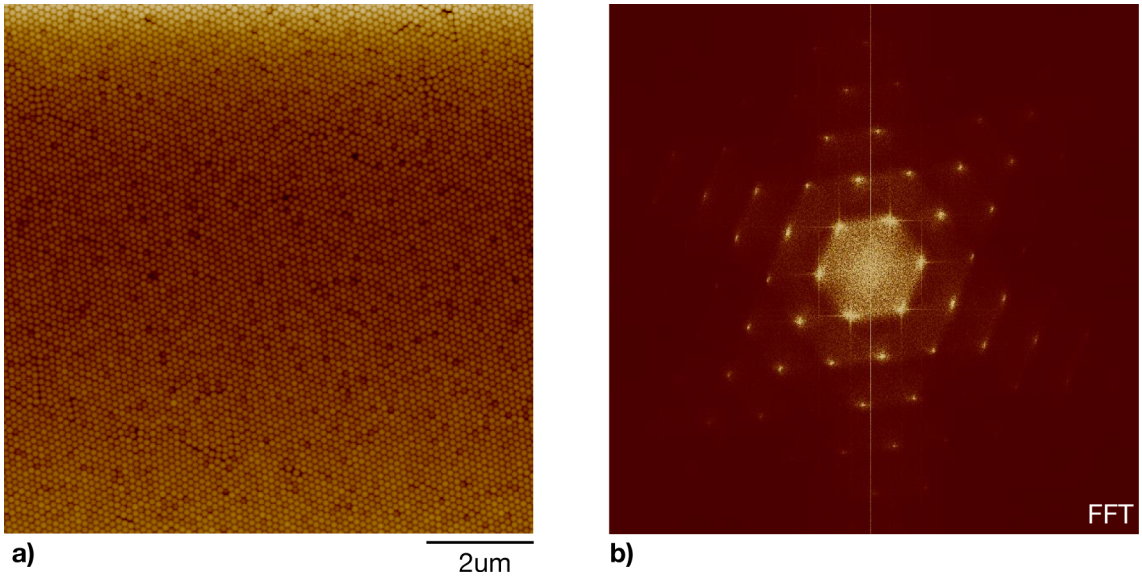

Figure 8.11: A monolayer of 200 nm-diameter polystyrene nanospheres deposited on a quartz substrate using the automated Langmuir-Blodgett technique. Subfigure (**a**), a tapping-mode atomic force microscopy image of the monolayer. Subfigure (**b**), a Fourier transform of the same image exhibiting the exceptional crystallinity achievable with this technique.

ion etching process, see fig. 8.12. The second used the nanosphere monolayers as a direct etch mask, see fig. 8.15 on page 110.

8.2.4 Metallic inversion

The metallic inversion method is attractive as it results in an exceptionally robust etch-mask that is capable of producing high aspect ratio nanostructures. The step-up to a high-contrast mask is made by possible through the exploitation of: the polymer-oxide contrast (step (**a**)–(**b**)), then the polymer-metal contrast (step (**b**)–(**c**)), and finally a metal-oxide contrast (step (**c**)–(**d**)) — see fig. 8.12.

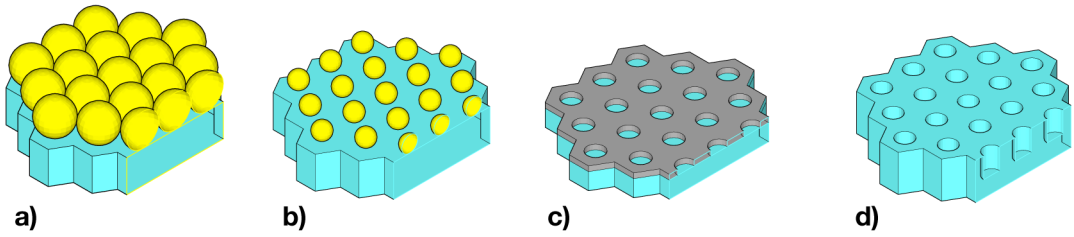

Figure 8.12: Metallic inversion of a self-assembled nanosphere monolayer in order to form a motheye etch mask. Subfigure (**a**), the nanospheres are deposited directly upon the quartz substrate forming a close-packed honeycomb pattern. Subfigure (**b**), the polystyrene nanospheres are shrunk in an isotropic plasma process. Subfigure (**c**), a line-of-sight chrome evaporation is followed by a solvent lift-off in order to yield a metallic hard-mask 'mesh'. Subfigure (**d**), anisotropic reactive ion etching forms a nanostructured (inverted) motheye interface.

A key step in the process, that enables an additional mode of control over the final nanostructures, is the isotropic plasma shrinking process (step (**a**)–(**b**)). The self-assembled polystyrene nanosphere monolayer is exposed to a low-power (50 W) oxygen plasma struck at a pressure of 40 mTorr. In order to verify that the etch process was indeed isotropic we analysed a series of samples (at different exposure-times) using both scanning electron microscopy (SEM) and atomic force microscopy (AFM), see fig. 8.13 on the following page. The SEM images were analysed using ImageJ in order to assess the decrease in diameter as a function of time. Whereas our AFM scans were used to obtain the vertical decrease in diameter by extracting the step height from a two-dimensional map at the edge of an array of nanospheres.

Both vertical and horizontal diameters of the nanospheres decreased linearly with time. This information is useful to us in two ways. Firstly, since the diameter of the nanospheres prior to evaporation of the hard-mask is the same as the width of the holes it defines, a long isotropic O_2 etch will leave less of the substrate exposed and be more tolerant to under-cutting effects during the final reactive ion etch. Secondly, the height decrease of the nanospheres places a limit on the thickness of the Cr hard-mask that can be used. The solvent lift-off process requires that the deposition of a Cr layer be less than half of the nanosphere's height. As an example, in order to use a 30 nm Cr hard-mask (as per the electron beam method, above) the O_2 shrinking process must be performed for *less* than 120 seconds.

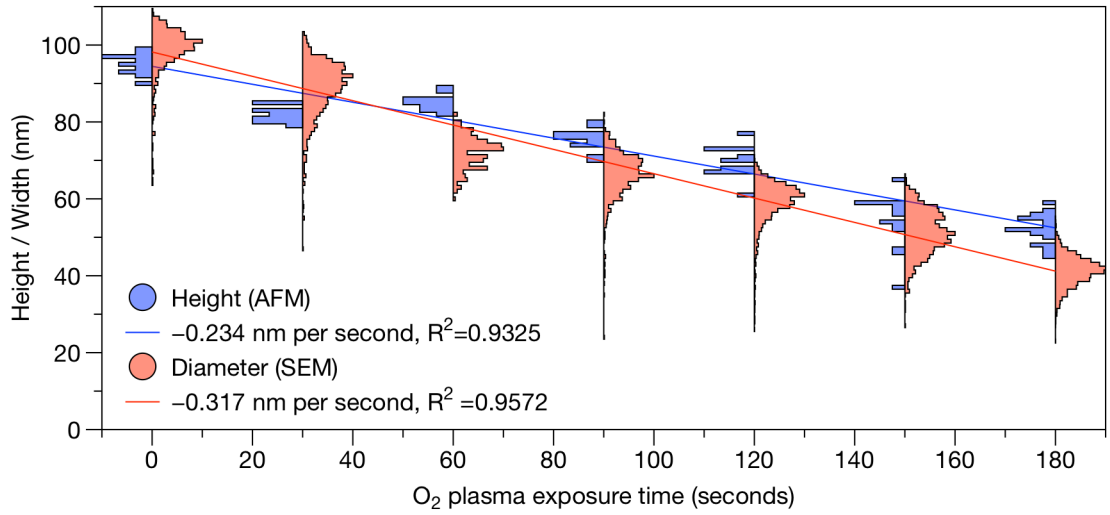

Figure 8.13: The horizontal and vertical reduction in diameter of polystyrene nanospheres under the action of isotropic O_2 plasma etching. Images taken with a scanning electron microscope were analysed using software (ImageJ) in order to determine the distribution of diameters (horizontal) after the shrinking process (shown in red). This correlates with a vertical decrease in diameter measured by extracting the maximum step-height of a two-dimensional tapping-mode atomic force microscopy scan at the edge of nanosphere array (shown in blue).

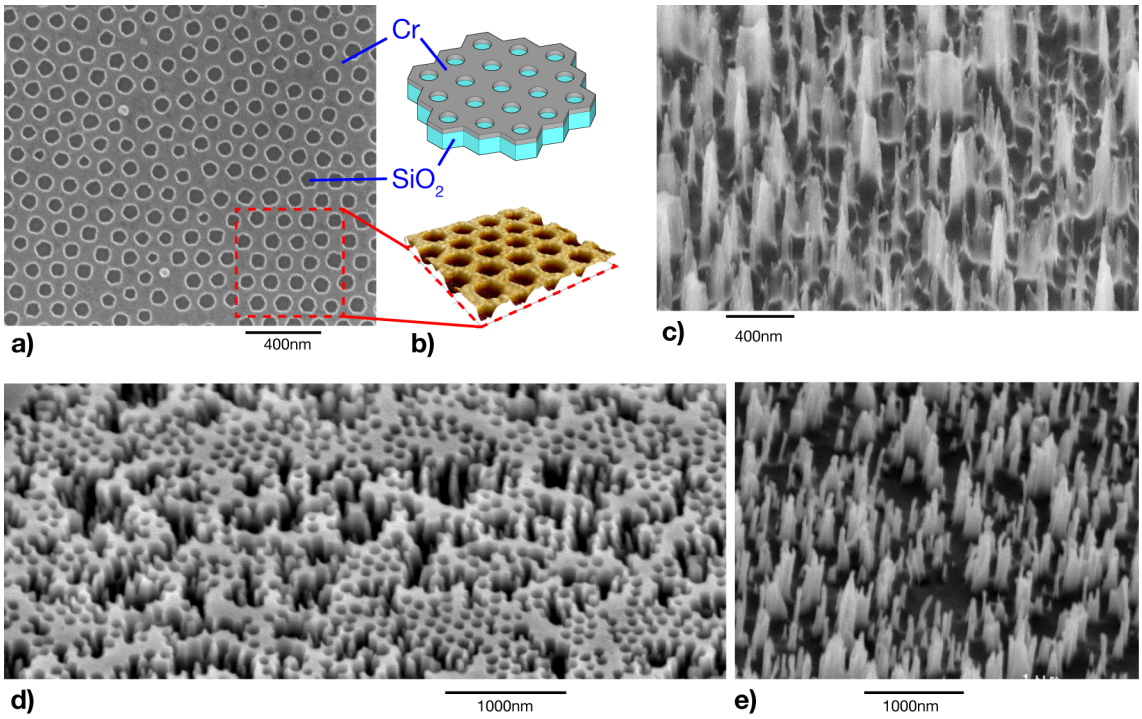

Figure 8.14: Nanostructures produced through reactive ion etching of glass through a self-assembled Cr hard-mask. Subfigures (**a**) and (**b**), the chrome hard-mask following the solvent lift-off of the polystyrene nanosphere template. Subfigures (**c**)–(**e**), a variety of glass nanostructures produced through the use of different nanosphere O_2 etch-times leading to smaller/larger hard-mask fill-factors.

A variety of nanostructure characteristics can be achieved using an inverted metallic mask. When the O_2 etch time is too high the resulting structure takes the form of a porous

'honeycomb', see subfigure (**d**) in fig. 8.14 on page 109. Whereas, little or no shrinking results in a sparse, low fill-factor chrome hard-mask that leads to columnar nanopillars, see subfigure (**e**) in fig. 8.14 on page 109. Optimal shrinking (which leaves approximately 50% of the glass surface exposed) can lead to high aspect ratio motheye-like nanospikes, see subfigure (**c**).

Unfortunately, the nanostructures we were able to produce using this method did not resemble the motheye structures we set out to fabricate. We abandoned this technique as the design rules established in our previous chapter were unable to provide guidance and we recognised that a direct-etch (described below) would bear much closer relation to naturally occurring motheyes.

8.2.5 Direct etching

Using the nanosphere monolayer as an etch mask (rather than inverting it to chrome) has the singular disadvantage that the reactive ion etching selectivity of polystyrene-to-glass is lower than chrome-to-glass. However, it introduces several advantages. First and foremost, the process is much simpler; it involves the deposition of the nanosphere monolayer and then reactive ion etching, see fig. 8.15. There is no requirement to optimise or undertake intermediary steps. Secondly, the etch-mask (polystyrene nanospheres) shrink continuously during the reactive ion etching process. This leads directly to tapered structures and exhibits better mimicry's of naturally occurring motheyes than the inverted metallic-mask discussed previously.

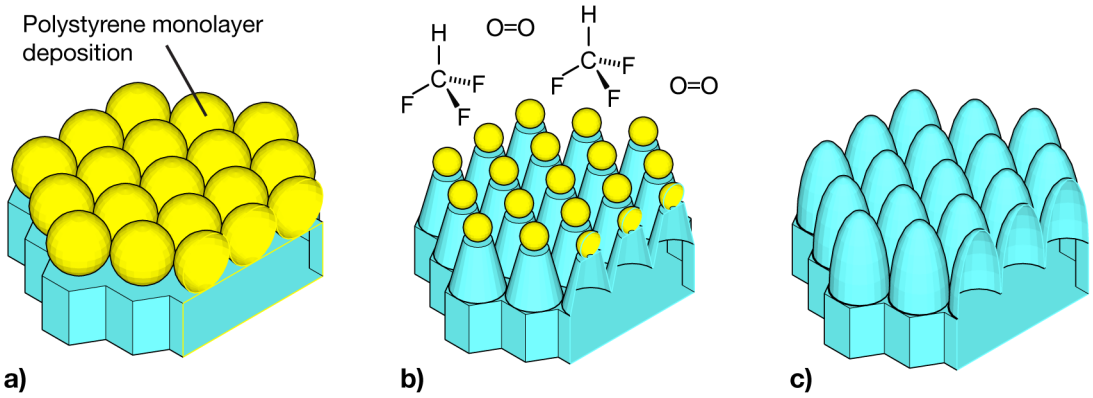

Figure 8.15: Direct etching of polystyrene nanospheres on glass in order to produce tapered motheye nanostructures. Subfigure (**a**), a close-packed monolayer of nanospheres is deposited directly upon the substrate. Subfigure (**b**), reactive ion etching with CHF_3 and O_2 simultaneously etches the glass and shrinks the masking nanospheres. Subfigure (**c**), after complete etching of the mask a tapered nanostructure closely resembling those found on the eyeballs of moths remains.

Reactive ion etching was performed using the same CHF_3 and O_2 etch chemistry as reported in section 8.1.4 on page 102. The by-product of the reaction between CHF_3 ions and SiO_2 (the substrate) is a fluoropolymer that is deposited locally, passivating vertical surfaces and thereby enhancing the anisotropy of the etch. The presence of O_2 is important as it counteracts the build-up of fluoropolymer. However, it serves an additional function in our process as it allows us to control the rate of etching of the masking polymer nanospheres.

We maintained a constant flow-rate of CHF_3 (40 sccm) but investigated the effect of different oxygen flow-rates, see fig. 8.16. Low-flow rates of O_2 (5 sccm) led to the formation of columnar pillars, see subfigure (**a**). Whereas, high-flow rates of O_2 (20 sccm) rapidly removed the mask and prevented high-aspect ratio nanostructures from forming, see subfigure (**b**). The chamber pressure remained unchanged throughout this study (40 mTorr), likewise with the power which was held at 200 W.

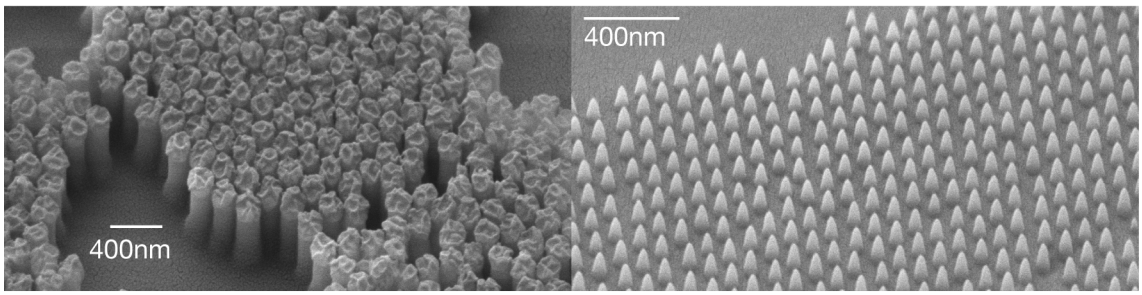

Figure 8.16: The affect of different oxygen flow-rates in the reactive ion etching of polystyrene nanospheres on glass using CHF_3. Subfigure (**a**), low oxygen flow rate 5 sccm leading to columnar SiO_2 pillars. Subfigure (**b**), high oxygen flow rate 20 sccm preventing the formation of high aspect-ratio nanostructures.

Etching past the point at which the nanosphere mask has been removed serves to degrade the aspect ratio of the nanostructures. In order to identify the point at which the optimum point at which the nanosphere mask is completely removed, we performed a series of etches over different periods of time. The two-dimensional height profile of the nanostructures on each sample were subsequently scanned using an atomic force microscope. The step height (from nanostructure tip to the substrate) as a function of etch-time is shown in fig. 8.17 on the following page. Up to 15 minutes of etching the step height continues to grow as the polystyrene nanosphere mask is still present and providing etch-selectivity. However, above this point, the height of the nanostructures decreases which we interpret as the removal of the mask. Therefore, we found that we could fabricate 600 nm-tall motheye nanostructures using 200 nm-diameter nanospheres and an etch time of 15 minutes, see fig. 8.18 on the next page. This was an encouraging result as our design rules showed that 600 nm-tall motheye nanostructures provided access to most regions of the motheye performance boundary, see fig. 7.11 on page 93.

8.2.6 Anti-reflection

We performed UV-VIS transmittance measurements in order to verify the anti-reflective properties of the motheye nanostructures shown in fig. 8.18 on the next page. Our measurements were made using a Elmer-Perkin Lambda-950 spectrophotometer and compared to transmittance measurements of flat quartz using the same system. see fig. 8.19 on page 113. Transmittance through the flat glass was measured to be 91.86% at $\lambda = 500\,\text{nm}$ and 95.42% through the nanostructured sample.

We calculated that reflectance at a flat quartz *interface* was 4.07% and only 0.51% when

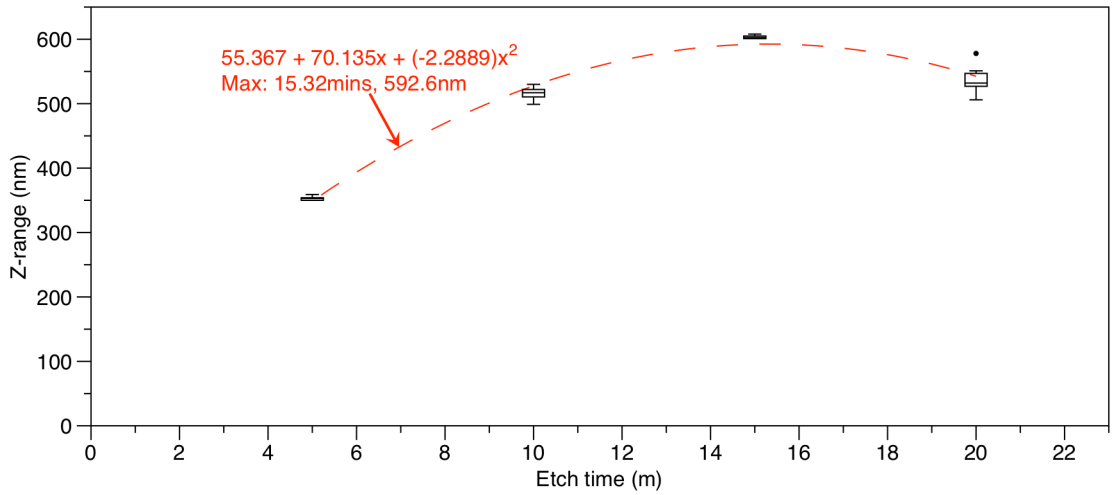

Figure 8.17: Determination of the optimum reactive ion etching time for polymer nanosphere masks. The height of the nanostructures increases with time for etch times up to 15 minutes in duration, after which, height decreases showing that the mask-to-substrate selectivity has been lost. These measurements were taken from two-dimensional tapping-mode atomic force microscopy scans.

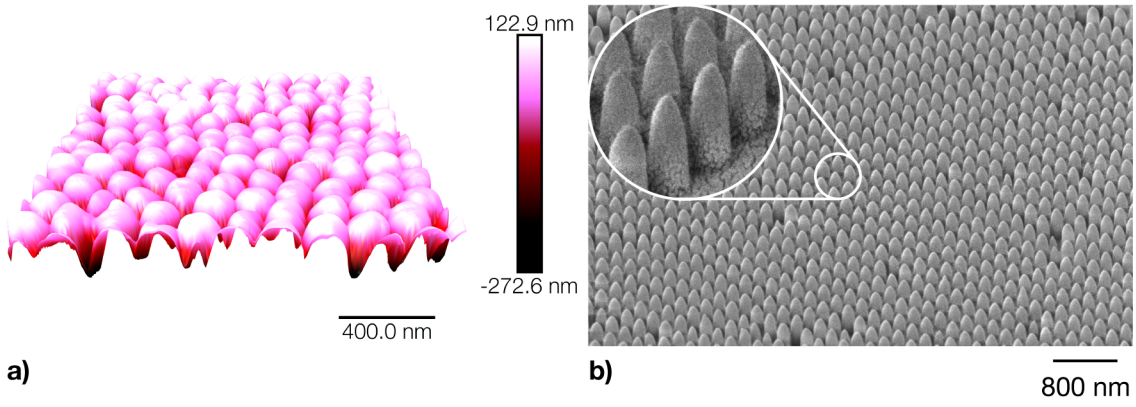

Figure 8.18: Optimised motheye nanostructures ($\approx 500\,\text{nm}$ in height) formed through direct etching of a polymer nanosphere monolayer (diameter $\phi = 200\,\text{nm} = \Lambda$ periodicity). Subfigure (**a**), a three-dimensional AFM projection of the motheye surface. Subfigure (**b**), an SEM image of the same motheye surface.

nanostructured with our motheye features $\lambda = 500\,\text{nm}$ — an impressive 8-fold suppression of reflectance. The reflectance suppression-ratio reduces to 3.5 for $\lambda = 1000\,\text{nm}$ and further still to 1.5 for $\lambda = 2000\,\text{nm}$, as expected from fig. 1.5 on page 30.

Visual inspection of our sample indicated some scattering may occur. Our calculations in fig. 1.3 on page 28 would suggest that this would not be the case for 200 nm periodic glass nanostructures. However, it is likely that defects in the masking nanosphere monolayer may have contributed to visual haze, as at dislocations in the monolayer, the effective motheye periodicity could approximately double. Further work is needed to verify this effect by characterising the angular transmittance of light through our samples.

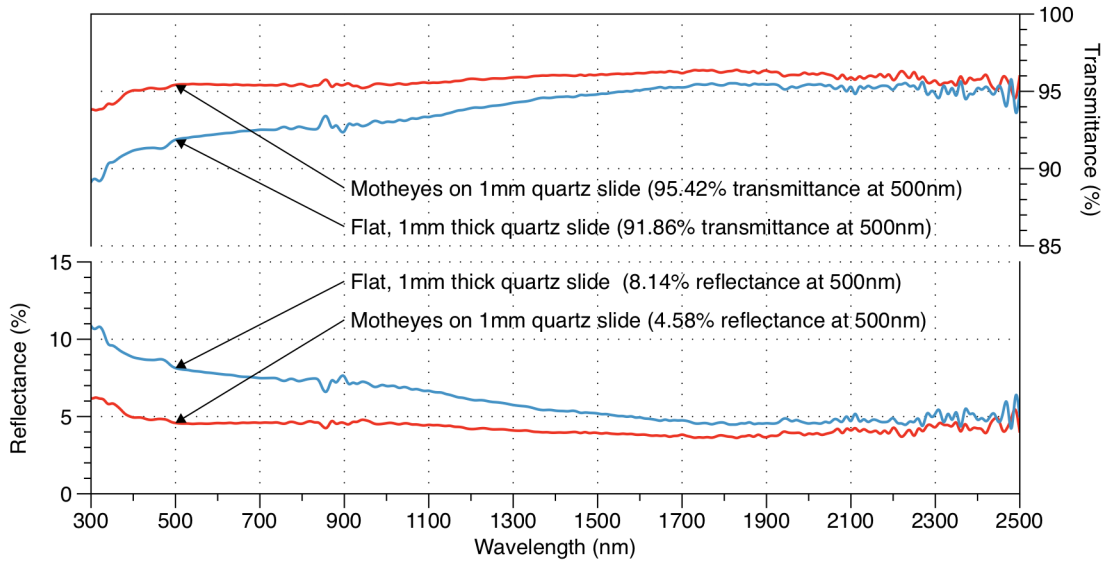

Figure 8.19: UV-Vis transmittance characterisation of our motheye sample.

8.2.7 Surface functionalisation

We performed an investigation into the combined affect of our motheye nanostructures and surface chemistry modification, see fig. 8.20 on the next page. Our wettability measurements were made by measuring the contact angle, θ_c, of a 5 μl water droplet using an FTA-100 system.

Immediately prior to functionalisation, our samples were baked on a hot plat at 200 °C for 10 minuets and then exposed to a 50 W O_2 plasma for 8 minuets in order to fully hydroxylate the surface. The first of our chemical modifications was made using Capstone ST-110, an aqueous fluorinated acrylic copolymer. Our sample was dipcoated into the solution and post-baked at 110 °C for 20 minutes. Our second functionalisation was performed using hexamethyldisilazane (HMDS) which was mixed with toluene at a volume concentration of 10%. The samples were placed into a beaker of this solution and stirred at 40 °C for 24 hours before being baked on a hotplate at 110 °C for 20 minutes. Our final method of functionalisation was performed as a vapour-phase deposition of Sigmacote (a commercially available chlorinated organopolysiloxane in heptane). The samples were placed in one chamber of a divided Petri dish whilst 5 ml of Sigmacote was deposited in its neighbouring division. A cover was placed over the dish and the volatile chemical allowed to evaporate and coat its surroundings over a period of 24 hours.

Without functionalisation, both the flat and nanostructured glass samples exhibited hydrophilic contact angles ($\theta_c = 44.1°$ and $\theta_c = 10.5°$ respectively), see subfigure (**a**) and (**e**) in fig. 8.20. The most potent functionalisation was found to be Sigmacote which increased the contact angles to $\theta_c = 99.2°$ for plain glass and $\theta_c = 132.8°$ for the nanostructured motheye surface. If one compares the top-row (flat samples) with the bottom-row (motheye nanostructures) in fig. 8.20 the extent to which nanostructure enhances surface's wettability is clearly visible. The un-functionalised SiO_2 motheye surface strongly imbibes the water droplet whereas, when functionalised, the droplet is prevented from entering the nanostructure and instead sits almost spherically on the surface.

Unfortunately, the contact angles we managed to achieve were below the super-hydrophobic threshold ($\theta_C \geq 140°$) established in section 1.3 on page 33. Furthermore, our samples showed various degrees of pinning depending upon which region of the sample the droplet was deposited. There are two possible causes for this, either the surface fill-factor of the nanostructures was not high enough due to defects in the self-assembly process and therefore 'blunt' regions existed. Alternatively, some of our surface modifications were not homogeneous and some hydrophilic regions existed in which the liquid meniscus was strongly imbibed into the nanostructure. This second interpretation may be likely as the pinning effects for the sample (**h**) were surprisingly greater than for sample (**g**) ($\theta_{\text{roll-off}} \approx 34°$ vs $\theta_{\text{roll-off}} \approx 17°$).

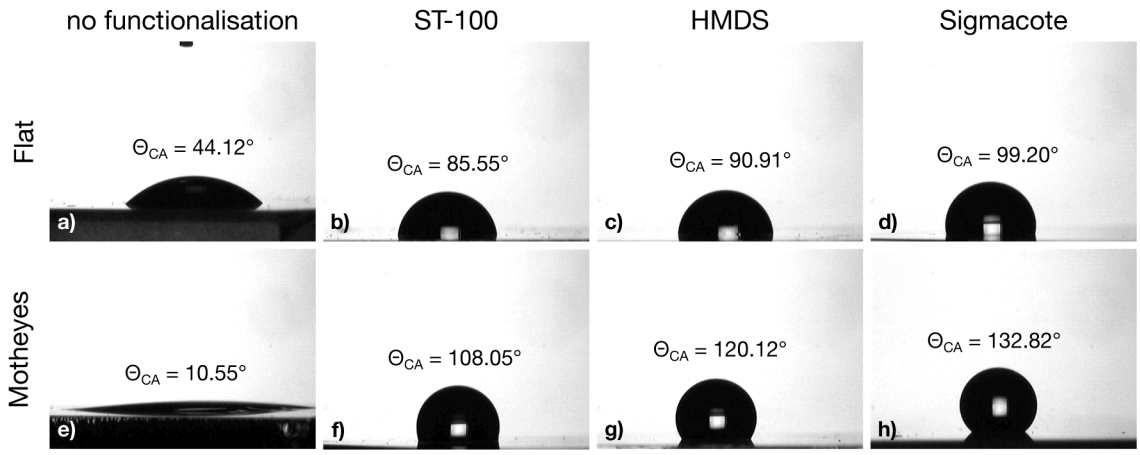

Figure 8.20: Demonstration of the combined effects of surface chemistry and nanostructure upon a surface's wettability. The top-row is comprised of flat quartz samples whereas the samples in the bottom-row have been nanostructured with motheye features (using the self-assembled direct-etching technique). These images, of 5 μl water droplets, were taken using an FTA-100 system. From left-to-right, the samples are: (**a**) & (**e**), un-functionalised (hydroxylated SiO_2); (**b**) & (**f**), functionalised with Capstone ST-100 fluoropolymer; (**c**) & (**g**) functionalised with hexamethyldisilazane; and (**d**) & (**h**), functionalised via a vapour deposition of Sigmacote.

Part IV

Summary

Chapter 9

Conclusions

This thesis combines novel energy mapping, modelling, experimental and fabrication work to advance the field of vanadium dioxide-based thermochromic smart windows.

The theory that underpins our unique approach toward improving the optical properties of vanadium dioxide smart windows was covered in detail. We identified the geometrical features that define the anti-reflection capabilities of nanostructured interfacial materials and explained how these same interfaces simultaneously induce enhanced wetting characteristics. Through a series of Finite Difference Time Domain simulations, the scale of which was unprecedented in the academic literature, we identified specific design rules for motheye smart windows. These were called upon directly during our investigations into their fabrication.

The project made a significant investment in the fabrication of motheye nanostructures. We had not anticipated the time required to develop the self-assembly techniques that enabled large area fabrication to take place. Unfortunately, this meant we had to relinquish our early goal to coat motheye nanostructures with vanadium dioxide and measure the thermochromic response. We believe that doing so will be possible in the near future and we hope that the work presented in this thesis (design rules, fabrication procedures etc.) will make a valuable contribution toward these efforts.

Our map-based investigation into the best environments for thermochromic windows revealed a sugnificant market potential. However, our lessons from above must be taken into account with respect to the commercialsation of this smart window technology: the challenges associated with fabricating motheye nanostructures over a large area should not be underestimated. The requirement for sub-wavelength periodicities renders many low-cost techniques obsolete. The two competing requirements are cost and quality.

The cost per m^2 *must* be kept to an absolute minimum as these nanostructures are intended for commercial applications. Our initial top–down fabrication techniques were resource-intensive and expensive, however, we managed to reduce these costs by switching to self-assembled lithographic methods. The nanosphere solutions we used to create monolayer masks cost approximately 10$ per m^2. However, it has been suggested that (in spite of the future-saving in energy costs) in order to compete in a commercial context production costs should be reduced to approximately 2$ per m^2 – a price that would need to include not only the mask formation, but also the coating of VO_2. This would clearly be a major challenge and the fabrication techniques we developed in this project may need

to be altered considerably or entirely new ones found.

Small defects in the surface distribution, or nanostructures without an adequate aspect-ratio/height, will degrade the optical performance of such an interface and should be avoided. Unfortunately, the nanostructured samples we produced using the self–assembly methods showed some artefacts of visual haze and also high contact angle hysteresis due to pinning. A follow-up investigation into the motheye surface's wettability, thorugh alternative methods of surface-chemistry modification, would be of benefit. If is was found that inhomogeneous functionalisation had been occuring, the cause of pinning could be eliminated thereby facilitating the desired self-cleaning effect.

The mechanisms behind the spectral-selectivity and phase-switching of vanadium dioxide were both presented in detail, along with the methods by which these characteristics could be altered. We performed extensive analysis of vanadium dioxide synthesised via the Atmospheric Pressure Chemical Vapour Deposition technique. This is a favourable method of coating glass as it can be performed 'online' as part of the float-glass production process. The identification of the refractive index of a thermochromic material produced using a surface-reaction is unusual as target-based methods (such as sputtering and pulsed laser depositon) are more commonly employed to create reference films in the literature. We used this result within our simulations and hope it will support future efforts to design optimal vanadium dioxide window films. Results garnered from our simulations of planar VO_2 thin films on glass could be invaluable in this respect.

We can see two ways in which our work on the synthesis of vanadium dioxide synthesis could be extended. Firstly, more detailed analysis of the spatial variation of topography in the APCVD film would provide valuable insight into the growth kinetics of VO_2. For example, our sample featured temperature, growth-rate and turbulance gradients which could be exploited to reveal optimal growth conditions. Secondly, optical characterisation of the sample (UV-vis spectrophotometry) could be compared against simulations of transmittance through the surface in order to verify our methods of transmittance calculation are indeed compatible with films that contain characteristic APCVD morphologies.

Research into vanadium dioxided-based thermochromic smart window films has recieved a boost in recent years as nanostructured films have been shown to outperform planar structures in numerous studies. We hope that the graphical methods of comparison between competing designs and our identification of 'performance boundaries' will help to inform future research.

Part V

Appendix

Appendix A

Finite Difference Time Domain (FDTD) simulations

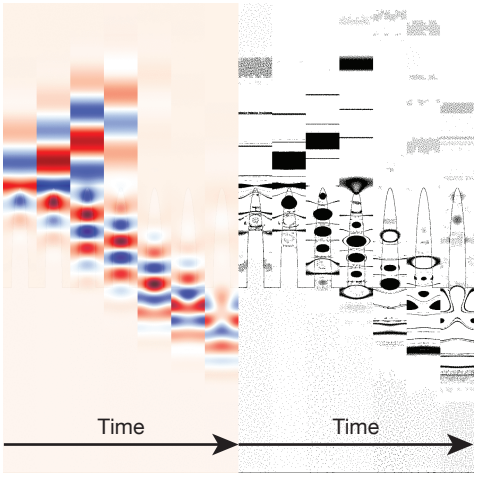

Figure A.1: Finite Difference Time Domain simulation snapshots of the electric field intensity.

Our FDTD method was implemented through proprietary software (Lumerical). For our motheye smart-window simulations the surface was decomposed into rectangular simulation cells of area Λ by $\sqrt{3}\Lambda$ with translational symmetry in the x and y dimensions (see Figure fig:HexagonalUnits).

Bloch boundary conditions were applied in both the x and y directions (see fig. A.2 on the next page). A broadband, planewave source was propagated normal to the surface by generating a short pulse with a controlled bandwidth. Linearly-independent wavelengths between 300 and 2500 nm were simulated in order to calculate our primary metrics over the full solar-range (T_{vis} and ΔT_{sol}). Two flux planes were placed one behind the source (in air) and the other below the interface (within the substrate). Data from these flux planes were used to calculate broadband reflectance, absorptance and transmittance coefficients as defined previously.

The spatial resolution of the Yee grid used to store the electromagnetic field information and the permeability of the materials represented within the simulations was typically close to 1.5 nm. Its actual value was a function of the thinnest layer in the simulation; set such that a minimum of three Yee cells would be included in each layer thereby satisfying

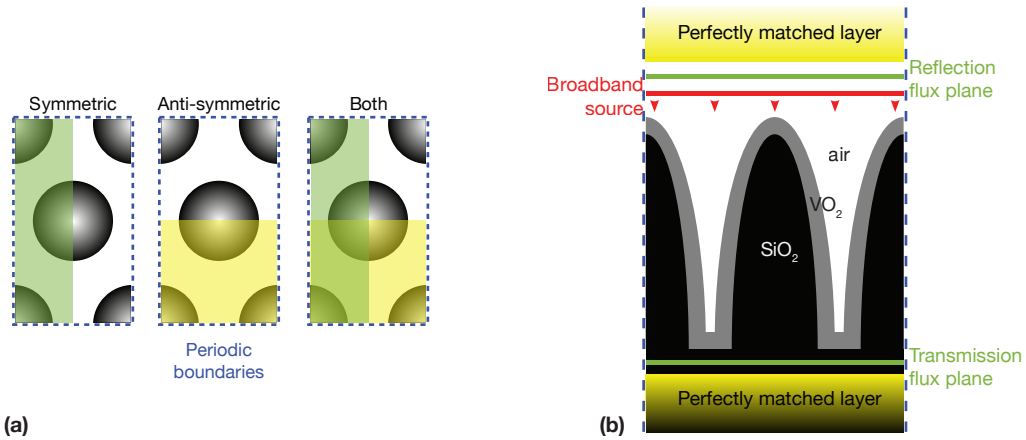

Figure A.2: Construction of our Finite Difference Time Domain geometry for simulating the interaction of electromagnetic waves with motheye nanostructures: periodic boundary conditions, flux planes, perfectly-matched-layers and plane-wave sources.

the Nyquist sampling condition. Convergence testing was a prerequisite for all simulations.

Appendix B

Mathematics for colloidal solutions

The close-packed periodicity, Λ, of circles on flat surface (or a monolayer of spheres) is equal to their diameter ϕ, therefore the two terms are interchangeable in all of the following equations. This is true for both 'hexagonal' and 'square' close-packed surface-distributions. However, the following derived relationships refer to *hexagonal surface-distributions only* (the highest-possible packing-density) as this is the natural formation of nanosphere monolayers.

The area of a triangle which contains three $\frac{1}{6}$ circular-segments ($\frac{1}{2}$ of a complete circle), A_{tri}, is equal to,

$$A_{\text{tri}} = \frac{\phi}{2} \times \frac{\sqrt{3} \cdot \phi}{2} \tag{B.1}$$

$$= \phi^2 \cdot \frac{\sqrt{3}}{4} \tag{B.2}$$

Therefore, the hexagonal unit-area enclosing a single sphere, $A_{\text{hex-unit-area}}$, is equal to,

$$A_{\text{hex-unit-area}} = 2 \times A_{\text{tri}} \tag{B.3}$$

$$= \phi^2 \times \frac{\sqrt{3}}{2} \tag{B.4}$$

In order to fill a target surface-area, $A_{\text{hex-mono}}$, with a hexagonally-arranged monolayer the number of spheres required, N, is given by,

$$N = \frac{A_{\text{hex-mono}}}{A_{\text{hex-unit-area}}} \tag{B.5}$$

$$= A_{\text{hex-mono}} \times \frac{2}{\sqrt{3} \cdot \phi^2} \tag{B.6}$$

The total volume of sphere-material ('colloids'), V_{colloids}, in a hexagonal-surface distri-

bution covering an area, $A_{\text{hex-mono}}$, is therefore,

$$V_{\text{colloids}} = N \times \frac{4\pi}{3} \cdot \left(\frac{\phi}{2}\right)^3 \tag{B.7}$$

$$= N \times \frac{\pi \cdot \phi^3}{6} \tag{B.8}$$

$$= \left\{ A_{\text{hex-mono}} \times \frac{2}{\sqrt{3} \cdot \phi^2} \right\} \times \frac{\pi \cdot \phi^3}{6} \tag{B.9}$$

$$V_{\text{colloids}} = \frac{\pi \cdot A_{\text{hex-mono}} \cdot \phi}{3\sqrt{3}} \tag{B.10}$$

Therefore, the mass of spheres, M_{colloids}, with a density ρ_{colloids} forming a monolayer covering an area $A_{\text{hex-mono}}$ is given by,

$$M_{\text{colloids}} = \rho_{\text{colloids}} \times V_{\text{colloids}} \tag{B.11}$$

$$= \rho_{\text{colloids}} \times \frac{\pi \cdot A_{\text{hex-mono}} \cdot \phi}{3\sqrt{3}} \tag{B.12}$$

Some colloidal solutions are supplied in specified colloidal-mass per volume concentrations (e.g. ρ). If the spheres form a mass-fraction in the solution of $f_{\text{col-m}}$ then the required mass of solution, M_{solution}, is given by,

$$M_{\text{solution}} = \frac{M_{\text{colloids}}}{f_{\text{col-m}}} \tag{B.13}$$

$$= \frac{\rho_{\text{colloids}} \cdot \pi \cdot A_{\text{hex-mono}} \cdot \phi}{3\sqrt{3} \cdot f_{\text{col-m}}} \tag{B.14}$$

However, since the solution is formed from both sphere-material *and* a host liquid with a density ρ_{host}, the combined solution density ρ_{solution} is expressed as,

$$\rho_{\text{solution}} = (\rho_{\text{colloids}} \times f_{\text{col-m}}) + \rho_{\text{host}}(1 - f_{\text{col-m}}) \tag{B.15}$$

Therefore the volume of solution required, V_{solution}, is given by,

$$V_{\text{solution}} = \frac{M_{\text{solution}}}{\rho_{\text{solution}}} \tag{B.16}$$

$$= \left\{ \frac{\rho_{\text{colloids}} \cdot \pi \cdot A_{\text{hex-mono}} \cdot \phi}{3\sqrt{3} \cdot f_{\text{col-m}}} \right\} \times \frac{1}{\rho_{\text{solution}}} \tag{B.17}$$

$$= \left\{ \frac{\rho_{\text{colloids}} \cdot \pi \cdot A_{\text{hex-mono}} \cdot \phi}{3\sqrt{3} \cdot f_{\text{col-m}}} \right\} \times \frac{1}{f_{\text{col-m}} \cdot \rho_{\text{colloids}} + \rho_{\text{host}}(1 - f_{\text{col-m}})} \tag{B.18}$$

$$V_{\text{solution}} = \frac{\rho_{\text{colloids}} \cdot \pi \cdot A_{\text{hex-mono}} \cdot \phi}{3\sqrt{3} f_{\text{col-m}} \cdot \left[f_{\text{col-m}} \cdot \rho_{\text{colloids}} + \rho_{\text{host}}(1 - f_{\text{col-m}}) \right]} \tag{B.19}$$

To put this into context, $80\,\mu$l of solution is required to cover a $10 \times 10\,$cm area with polystyrene spheres ($\phi = 125\,$nm). This assumes a $\rho_{\text{colloids}} = 1.05\,\frac{\text{g}}{\text{cm}}$ density of polystyrene at 1% mass-fraction in suspended in a host-liquid with a density of $\rho_{\text{colloids}} = 1.05\,\frac{\text{g}}{\text{cm}}$.

Appendix C

Review of dynamic window systems

C.0.1 Active implementations

Mechanical systems

The simplest form of mechanically-actuated smart-window system could arguably be the automatic open/closing mechanism found on the windows of horticultural greenhouses. However, we have selected two modern alternatives for discursive purposes. Both systems are 'active' and neither is 'consistently transparent'.

ClimaWin ClimaWin is an example of a commercialised active smart-window system which has a controlled switching cycle [234]. Communication between windows within the building is actuated over a wireless network. Each window is battery- and solar-powered; blinds and venting are automated and remote-controlled, allowing a user to programme the desired internal environment. Although transmission through the window pane is not controlled directly, this is a good example of an integrated active system for window control.

Elastomeric The mode of operation for elastomeric smart-windows is to either tension or release a patterned, flexible Polydimethylsiloxane (PDMS) film across the window's surface [235]. These systems exhibit two periodicities of roughness and are mechanically tunable. The system employs micron-scale wrinkles to scatter light whilst relaxed. In its tensioned state these wrinkles disappear, leaving a transmissive film. This system is unusual as its surface structure serves two roles: firstly, to increase-transmission (in the tensioned state); and secondly, to induce super-hydrophobicity. However, PDMS is known to lose its flexibility over time. This would limit the lifetime of such a system, particularly under prolonged UV exposure.

Electrochromic systems

This is the first of several 'chromogenic' systems that are characterised by a change of optical-properties in response to an external stimulus. The optical properties of *electrochromic* materials change in response to an applied voltage. This effect was first explained in

1969 and has since found applications in smart-windows and vehicles (dimming sunroofs). Typically, electrochromic systems are bi-stable; only requiring electrical energy to switch between states . In order to facilitate the implementation of such systems a number of self-powered electrochromic window devices have be been developed that incorporate photovoltaic cells [236–238].

Electrochromic systems are typically composed from multiple layers deposited directly onto either fluorine-, or indium-doped tin oxide coated glass substrates. There are three principle layers: the electrochromic film, the ion-conductor and the ion-storage layers [239, 240]. The electrochromic film darkens in response to electrons entering the material's lattice from the external circuit which interact with positive ions provided by the ion storage layer [8]. The ion-conducting electrolyte is adjacent to the ion storage layer which itself darkens as it releases positive ions.

An environmental and cost challenge for electrochromic windows has been to increase their lifetime from 15 years up to a maximum expected lifetime of 25 years [241]. These systems typically only survive a few thousand switching cycles. Implementing an electrochromic switching interface over large surface areas such as floor-to-ceiling windows can pose a challenge. In addition, the cost of manufacturing a five-layer film stack with associated contacts and control hardware can be high.

In spite of the challenges above, electrochromic systems are one of the most popular classes of smart-window. Their transmission-modulation can be very large and fast. However, their impressive switching-magnitude is a function of reduced visible transmission in the hot state [242]. In other words electrochromic systems are not 'consistently transparent'. In certain circumstances electrochromic window systems are most efficiently employed to reduce energy expenditure on lighting within a building [243].

Gasochromic systems

Gasochromic windows also employ electrochromism as their switching mechanism. In contrast to the electrochromic system described above, these windows respond to the presence of hydrogen gas (H_2) as opposed to an applied DC voltage [16]. In order to reduce transmission, hydrogen gas is pumped into the evacuated region of a double glazed unit where it provides the ions required to dim the electrochromic film. Therefore, additional ion-conductor and storage-layers are not required [8], thus reducing the fabrication cost and complexity of the glass pane. However, only a limited number of electrochromic materials respond to the presence of hydrogen and the gas exchange process must be strictly controlled [244].

Gasochromic systems have an advantage over their electrochromic siblings in that producing a full-height window panel is possible without a network of electrical contacts or large-area, transparent conducting-layers. However, they suffer from two of the electrochromic system's drawbacks: a limited number of switching cycles and *in*consistent transparency. In addition, the gasochromic system has some unique challenges. Firstly, switching speed is limited by the diffusion speed of H_2 gas within the glass unit. Secondly, the requirement for two layers prevents their use in automotive applications. Thirdly, condensation between the glass layers can cause damage to the chromogenic material. Fourthly, the use of potentially explosive H_2 gas in domestic environments is a safety

concern.

Liquid crystal systems

Polymer-dispersed liquid crystal technology has been developed extensively for a wide variety of applications. When exposed to UV, as an external window layer, their short lifetime is a major drawback. However, this has not prevented their use in a number of premium internal environments where privacy is required.

The principle of operation of a liquid crystal system is to confine a thin liquid crystal layer between conductive substrates. Light is scattered by the randomly aligned crystals but under the presence of an electric field the orientation of the crystals can be set to allow visible light transmission [245]. The electrical power required to maintain the transmissive state is significant. In order to offset this, work has been done towards incorporating photovoltaic energy-harvesting within the liquid smart-window system. An example of one of these approaches has been to dye-dope the liquid crystal solution in order to redirect the light within the glass pane configured as a luminescent solar concentrator [246].

Suspended particle systems

Suspended particle systems are closely related to liquid crystal systems; whereby an active layer is confined between two conducting electrodes. Unlike liquid crystal systems, light is absorbed by randomly aligned dipole particles within the active layer, not scattered. Transmission is achieved under the application of an electric field which orientates the particles. These systems are able to switch state at high speed but consume significant amounts of electrical energy in order to function.

C.0.2 Passive implementations

Passive systems switch their transmissive state automatically, activated by environmental conditions such as light intensity or ambient temperature.

Photochromic systems

Photochromic technology is often employed within high quality sunglasses. These systems dim the entire spectrum (visible and infrared) in response to high levels of solar UV radiation. They are therefore not 'consistently transparent'. It has been shown that windows which are able to switch their transmission when solar activity is high offer good potential for energy-saving with respect to *electrical indoor lighting*. However, the energy demands to heat a building usually far exceed those to light it. Furthermore, this technology will always counteract a greenhouse effect irrespective of the ambient temperature; even during the cold winter months when mid-day greenhouse heat gain could be beneficial.

Thermochromic systems

The optical properties of thermochromic materials are altered in response to temperature. Many inorganic materials, the majority of which are tinted, display temperature-dependent transmission switching between their monoclinic (cold) and tetragonal (hot) states [8].

Metal-to-semiconducting transition within these materials occurs at a critical temperature, τ_c. For a general thermochromic smart-window system, τ_c should be as close as possible to the desired ambient temperature. One of the most promising thermochromic materials for smart-window applications is vanadium dioxide (VO_2) as deep switching occurs within the infrared region leaving the visible region relatively unchanged. A detailed discussion of the material properties of vanadium dioxide is given in chapter 3 on page 48.

With respect to VO_2-based systems it must be acknowledged that as a 'consistently transparent' system the potential for solar modulation is limited. However, thermochromic systems hold several advantages. Window structures are typically simple [247] with no operational energy consumption and therefore have the potential to be low-cost [124]. This type of smart-window system can directly replace conventional windows, maintaining a visual link between the internal and external environments [248], and does not require compensatory lighting when in the hot state. In principle, thermochromic systems can cycle between hot and cold states indefinitely.

Thermotropic systems

Thermotropic systems utilise water-soluble polymers (hydrogels) confined between two planes of glass that aggregates at high temperatures [249]. A commercial example of this type of smart-window was developed by Suntek and is known as 'Cloud Gel'. The commercial system's name alludes to its optical characteristics. At low temperatures the isotropic aqueous solution is transparent as the polymer is homogeneously dissolved. As the window transitions to its hot state amphipathic molecules within the solution bind with the polymer causing hydrophobic aggregation and a phase change within the hydrogel. A microscopically homogeneous network is formed of polymer clumps, each large enough to scatter light. This increases the windows haze and its appearance becomes diffuse 'paper white'. Transmittance and solar-thermal modulation are both a function the hydrogel layer's thickness.

Thermotropic systems are passive, simple, cheap to fabricate, and significantly modulate solar-thermal transmission into a building. However, these types of systems are not 'consistently transparent' and would be best suited as roof panels.

Appendix D

Supporting mathematics

D.1 Hexagonal circle-packing

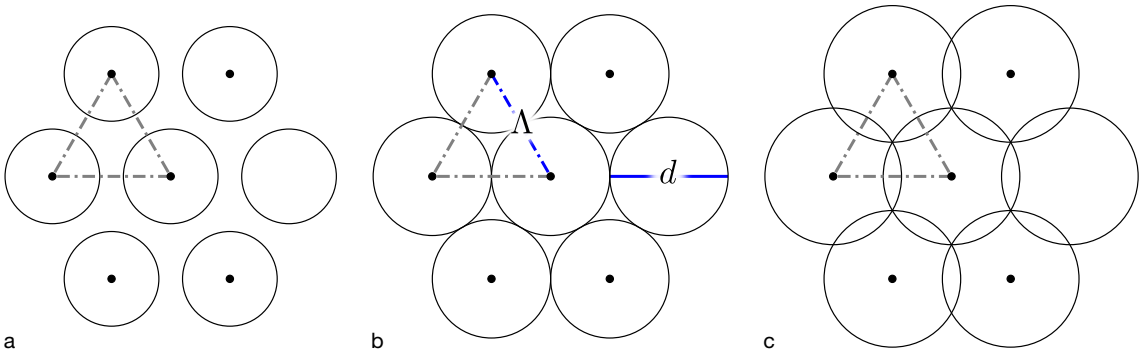

Figure D.1: Circular packing conditions: (a) $\phi < \Lambda$; (b) $\phi = \Lambda$; (c) $\Lambda > \phi \leq \Lambda\sqrt{\frac{4}{3}}$.

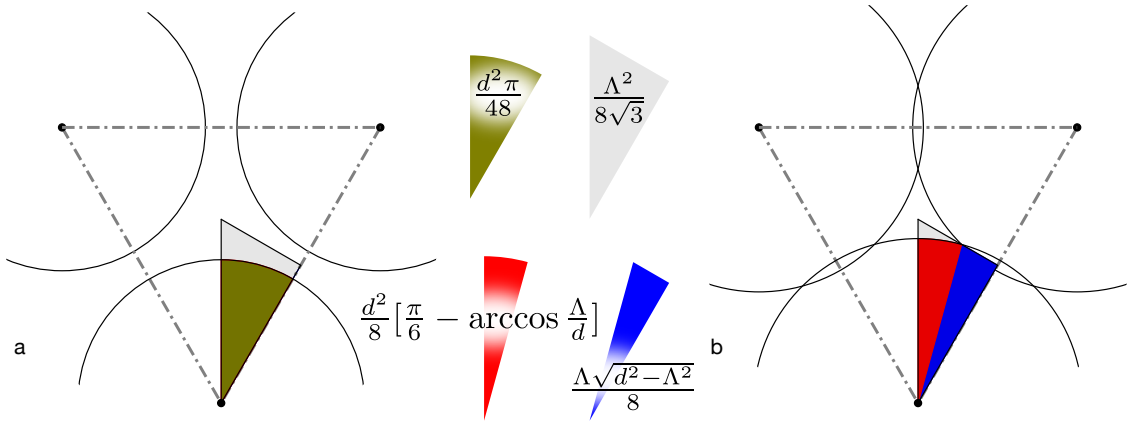

Figure D.2: Analytical expressions for circle-filling of a unit-area, right-angle triangle. The right-angled triangle represents the smallest division of a hexagonal surface.

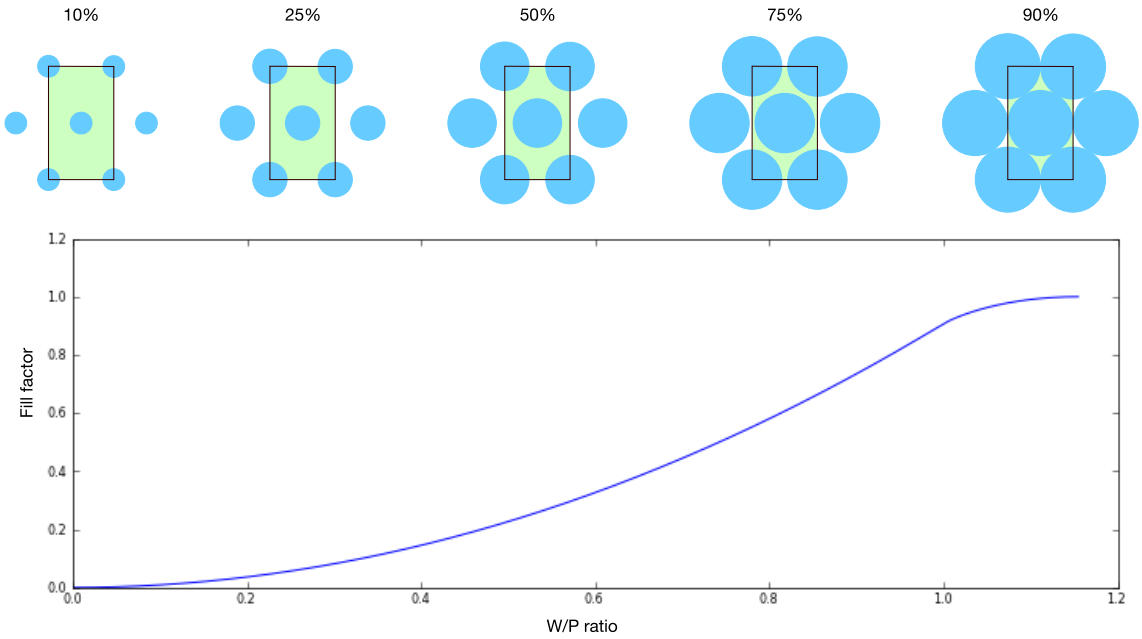

Figure D.3: The surface filling-factors for hexagonally packed circles.

D.2 Subdivisions of hexagonal surfaces

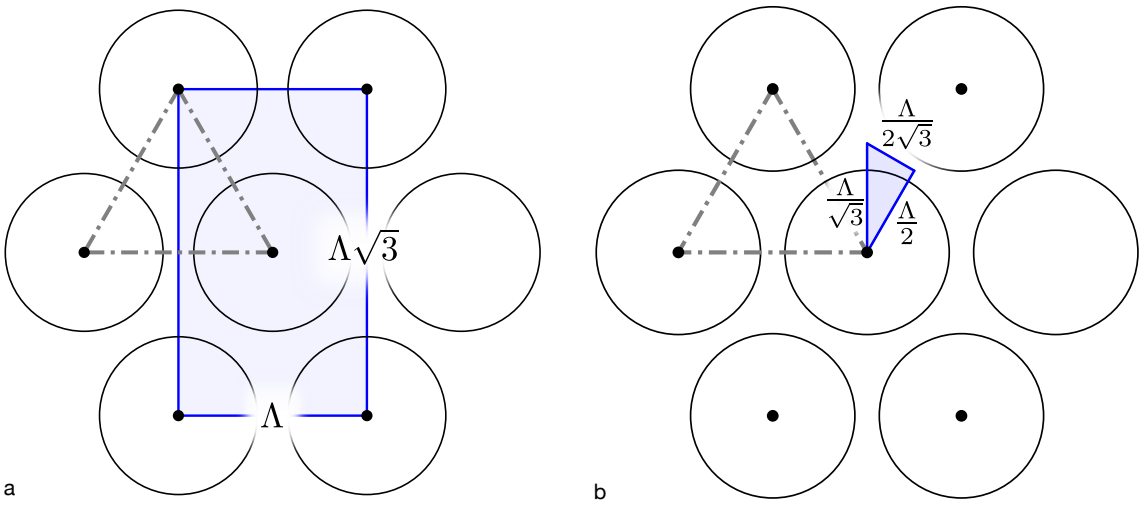

Figure D.4: Subdivisions of a hexagonal surface. (a) the unit-square of a hexagonal surface with translational symmetry, (b) the unit-triangle.

D.3 Tapered motheye profiles

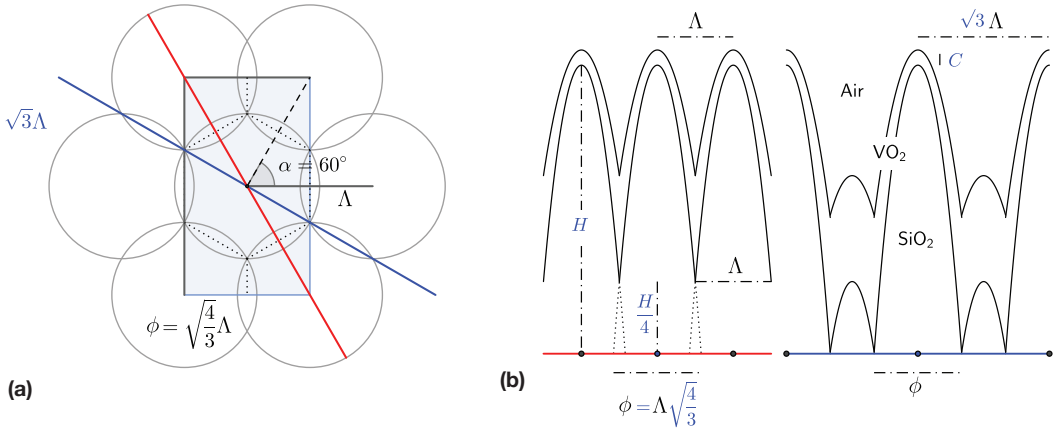

Figure D.5: Cross-sections of parabolic motheyes nanostructures, $\phi = \Lambda\sqrt{\frac{4}{3}}$.

Bibliography

[1] International Energy Agency. *Transition to Sustainable Buildings*. Tech. rep. Paris: International Energy Agency, 2013. DOI: 10.1787/9789264202955-en.

[2] International Energy Agency. *Technology Roadmap; Energy efficient building envelopes*. Tech. rep. Paris: International Energy Agency, 2013, p. 68.

[3] International Energy Agency. *Energy Technology Perspectives (Executive Summary)*. Tech. rep. Paris: International Energy Agency, 2014, p. 14. DOI: 10.1787/energy_tech-2014-en.

[4] International Energy Agency. *Technology Roadmap; Energy-efficient Buildings: Heating and Cooling Equipment*. Tech. rep. International Energy Agency, 2011.

[5] UN. *World Population Prospects: The 2015 Revision*. Tech. rep. United Nations, 2015.

[6] Marina Fischer-Kowalski and Anke Schaffartzik. 'Energy availability and energy sources as determinants of societal development in a long-term perspective'. In: *MRS Energy & Sustainability* 2 (2015), E1. ISSN: 2329-2229. DOI: 10.1557/mre.2015.2.

[7] UNEP SBCI. *Buildings and climate change: a summary for decision-makers*. Tech. rep. Paris: United Nations Environment Programme, 2007, pp. 1–62. DOI: ISBN: 987-92-807-3064-7DTI/1240/PA.

[8] M. Kamalisarvestani et al. 'Performance, materials and coating technologies of thermochromic thin films on smart windows'. In: *Renewable and Sustainable Energy Reviews* 26 (2013), pp. 353–364. ISSN: 13640321. DOI: 10.1016/j.rser.2013.05.038.

[9] D&R International Ltd. *2011 Buildings Energy Data Book*. Tech. rep. Pacific Northwest National Laboratory, 2012.

[10] International Energy Agency. *Key World Energy Statistics*. Tech. rep. Paris: International Energy Agency, 2014.

[11] George Crabtree et al. *How America can look within to achieve energy security and reduce glodal warming*. Tech. rep. American Physical Society, 2010, pp. 1–109.

[12] Piet Eichholtz, Nils Kok, and John M. Quigley. 'The Economics of Green Building'. In: *Institute of Business and Economic Research: Housing and Urban Policy* (2011).

[13] Judith A Leech et al. 'It's about time: A comparison of Canadian and American time-activity patterns'. In: *Journal of Exposure Analysis and Environmental Epidemiology* 12.6 (2002), pp. 427–432. ISSN: 10534245. DOI: 10.1038/sj.jea.7500244.

[14] C.G. Granqvist et al. 'Nanomaterials for benign indoor environments: Electrochromics for "smart windows", sensors for air quality, and photo-catalysts for air cleaning'. In: *Solar Energy Materials and Solar Cells* 91.4 (2007), pp. 355–365. ISSN: 09270248. DOI: 10.1016/j.solmat.2006.10.011.

[15] Gordon M Heisler and Anthony J Brazel. 'The urban physical environment: temperature and urban heat islands'. In: *Agronomy Mongraph 55. Urban Ecosystem Ecology.* 13210 (2010), pp. 29–56. DOI: 10.2134/agronmonogr55.c2.

[16] Ruben Baetens, Bjorn Petter Jelle, and Arild Gustavsen. 'Properties, requirements and possibilities of smart windows for dynamic daylight and solar energy control in buildings: A state-of-the-art review'. In: *Solar Energy Materials and Solar Cells* 94.2 (2010), pp. 87–105. ISSN: 09270248. DOI: 10.1016/j.solmat.2009.08.021.

[17] Andrew Verity. 'Who, what, why: How does a skyscraper melt a car?' In: *BBC News* (2013).

[18] Q. Chen et al. 'Broadband moth-eye antireflection coatings fabricated by low-cost nanoimprinting'. In: *Applied Physics Letters* 94.26 (2009), p. 263118. ISSN: 00036951. DOI: 10.1063/1.3171930.

[19] Alaric Taylor et al. 'A bioinspired solution for spectrally selective thermochromic VO_2 coated intelligent glazing'. In: *Optics express* 21.105 (2013), A750–A764. ISSN: 1094-4087. DOI: 10.1364/OE.21.00A750.

[20] Kyoo-Chul Park et al. 'Nanotextured Silica Surfaces with Robust Superhydrophobicity and Omnidirectional Broadband Supertransmissivity'. In: *ACS Nano* 6.5 (2012), pp. 3789–3799. ISSN: 1936-0851. DOI: 10.1021/nn301112t.

[21] A R Parker and C R Lawrence. 'Water capture by a desert beetle.' en. In: *Nature* 414.6859 (2001), pp. 33–4. ISSN: 0028-0836. DOI: 10.1038/35102108.

[22] Taolei Sun et al. 'Bioinspired surfaces with special wettability.' en. In: *Accounts of chemical research* 38.8 (2005), pp. 644–52. ISSN: 0001-4842. DOI: 10.1021/ar040224c.

[23] L. Feng et al. 'Super-Hydrophobic Surfaces: From Natural to Artificial'. In: *Advanced Materials* 14.24 (2002), pp. 1857–1860. ISSN: 09359648. DOI: 10.1002/adma.200290020.

[24] Jan Genzer and Kirill Efimenko. 'Recent developments in superhydrophobic surfaces and their relevance to marine fouling: a review.' In: *Biofouling* 22.5-6 (2006), pp. 339–60. ISSN: 0892-7014. DOI: 10.1080/08927010600980223.

[25] C G Bernhard and W H Miller. 'A corneal nipple pattern in insect compound eyes.' In: *Acta physiologica Scandinavica* 56.3-4 (1962), pp. 385–6. ISSN: 0001-6772. DOI: 10.1111/j.1748-1716.1962.tb02515.x.

[26] Carl Gustaf Bernhard, Gösta Gemne, and J. Sällström. 'Comparative ultrastructure of corneal surface topography in insects with aspects on phylogenesis and function'. In: *Zeitschrift für vergleichende Physiologie* 67.1 (1970), pp. 1–25. ISSN: 0340-7594. DOI: 10.1007/BF00298117.

[27] S J Wilson and M C Hutley. 'The optical properties of 'moth eye' antireflection surfaces'. In: *Optica Acta* 29.7 (1982), pp. 993–1009.

[28] Andrew R Parker and Helen E Townley. 'Biomimetics of photonic nanostructures.' en. In: *Nature nanotechnology* 2.6 (2007), pp. 347–53. ISSN: 1748-3395. DOI: 10.1038/nnano.2007.152.

[29] Colin R. Crick and Ivan P. Parkin. 'Aerosol assisted deposition of melamine-formaldehyde resin: Hydrophobic thin films from a hydrophilic material'. In: *Thin Solid Films* 519.7 (2011), pp. 2181–2186. ISSN: 00406090. DOI: 10.1016/j.tsf.2010.10.062.

[30] Doo-Hyun Ko et al. 'Biomimetic microlens array with antireflective "moth-eye" surface'. In: *Soft Matter* 7.14 (2011), p. 6404. ISSN: 1744-683X. DOI: 10.1039/c1sm05302g.

[31] Andreas Gombert et al. 'Antireflective submicrometer surface-relief gratings for solar applications'. In: *Solar Energy Materials and Solar Cells* 54.1-4 (1998), pp. 333–342. ISSN: 09270248. DOI: 10.1016/S0927-0248(98)00084-1.

[32] S.A. Boden and D.M. Bagnall. 'Bio-Mimetic Subwavelength Surfaces for Near-Zero Reflection Sunrise to Sunset'. In: *2006 IEEE 4th World Conference on Photovoltaic Energy Conference*. Vol. 2. IEEE. IEEE, 2006, pp. 1358–1361. ISBN: 1-4244-0016-3. DOI: 10.1109/WCPEC.2006.279683.

[33] Hitoshi Sai et al. 'Numerical Analysis and Demonstration of Submicron Antireflective Textures for Crystalline Silicon Solar Cells'. In: *2006 IEEE 4th World Conference on Photovoltaic Energy Conference*. Vol. 1. IEEE. IEEE, 2006, pp. 1191–1194. ISBN: 1-4244-0016-3. DOI: 10.1109/WCPEC.2006.279394.

[34] Noboru Yamada et al. 'Characterization of antireflection moth-eye film on crystalline silicon photovoltaic module'. In: *Optics Express* 19.March (2011), pp. 118–125. DOI: 10.1016/j.solmat.2010.04.024.V..

[35] Kwanyong Seo et al. 'Si Microwire Solar Cells: Improved Efficiency with a Conformal SiO_2 Layer.' In: *ACS nano* 7.6 (2013), pp. 5539–45. ISSN: 1936-086X. DOI: 10.1021/nn401776x.

[36] Jean-baptiste Brückner et al. 'Flat-top and patterned-topped cone gratings for visible and mid-infrared antireflective properties'. In: *Optics Express* 21.13 (2013), pp. 333–339. DOI: 10.1364/OE.21.016043.

[37] L Escoubas et al. 'An antireflective silicon grating working in the resonance domain for the near infrared spectral region'. In: *Optics Communications* 226.1-6 (2003), pp. 81–88. ISSN: 00304018. DOI: 10.1016/j.optcom.2003.08.034.

[38] Petros I Stavroulakis et al. 'Suppression of backscattered diffraction from sub-wavelength 'moth-eye' arrays.' In: *Optics express* 21.1 (2013), pp. 1–11. ISSN: 1094-4087.

[39] Volkmar Boerner et al. 'P-20: Antireflection Systems for Flat Panel Displays - an overview'. In: *SID Symposium Digest of Technical Papers* 35.1 (2004), p. 306. ISSN: 0097966X. DOI: 10.1889/1.1830975.

[40] D G Stavenga et al. 'Light on the moth-eye corneal nipple array of butterflies.' In: *Proceedings. Biological sciences / The Royal Society* 273.1587 (2006), pp. 661–7. ISSN: 0962-8452. DOI: 10.1098/rspb.2005.3369.

[41] Klaus Vogt. 'Optische Untersuchungen an der Cornea der Mehlmotte *Ephestia kühniella*'. In: *Journal of Comparative Physiology* 88.2 (1974), pp. 201–216. ISSN: 0340-7594. DOI: 10.1007/BF00695407.

[42] Daniel H Raguin and G Michael Morris. 'Antireflection structured surfaces for the infrared spectral region.' In: *Applied optics* 32.7 (1993), pp. 1154–67. ISSN: 0003-6935.

[43] Atikur Rahman et al. 'Sub-50-nm self-assembled nanotextures for enhanced broadband antireflection in silicon solar cells'. In: *Nature Communications* 6 (2015), pp. 1–6. DOI: 10.1038/ncomms6963.

[44] William H Southwell. 'Coating design using very thin high- and low-index layers.' In: *Applied optics* 24.4 (1985), pp. 457–460. ISSN: 0003-6935.

[45] William H Southwell. 'Pyramid-array surface-relief structures producing antireflection index matching on optical surfaces'. In: *JOSA A* 8.3 (1991), pp. 549–553.

[46] Wei-lun Min, Peng Jiang, and Bin Jiang. 'Large-scale assembly of colloidal nanoparticles and fabrication of periodic subwavelength structures'. In: *Nanotechnology* 19.47 (2008), p. 475604. ISSN: 0957-4484. DOI: 10.1088/0957-4484/19/47/475604.

[47] S. Bruynooghe et al. 'Antireflection coatings combining interference multilayers and a nanoporous MgF_2 top layer prepared by glancing angle deposition'. In: *Surface and Coatings Technology* (2014). ISSN: 02578972. DOI: 10.1016/j.surfcoat.2014.09.063.

[48] Lanying Yang et al. 'Hybrid moth-eye structures for enhanced broadband antireflection characteristics'. In: *Applied Physics Express* 3.10 (2010), p. 102602. ISSN: 1882-0778. DOI: 10.1143/APEX.3.102602.

[49] Olivier Deparis et al. 'Assessment of the antireflection property of moth wings by three-dimensional transfer-matrix optical simulations'. In: *Physical Review E* 79.4 (2009), pp. 1–7. ISSN: 1539-3755. DOI: 10.1103/PhysRevE.79.041910.

[50] Chih-hung Sun, Peng Jiang, and Bin Jiang. 'Broadband moth-eye antireflection coatings on silicon'. In: *Applied Physics Letters* 92.6 (2008), p. 061112. ISSN: 00036951. DOI: 10.1063/1.2870080.

[51] Radwanul Hasan Siddique, Guillaume Gomard, and Hendrik Hölscher. 'The role of random nanostructures for the omnidirectional anti-reflection properties of the glasswing butterfly'. In: *Nature Communications* 6 (2015), p. 6909. ISSN: 2041-1723. DOI: 10.1038/ncomms7909.

[52] Scott R Kennedy and Michael J Brett. 'Porous broadband antireflection coating by glancing angle deposition.' In: *Applied optics* 42.22 (2003), pp. 4573–9. ISSN: 0003-6935.

[53] Harland G. Tompkins. *Handbook of Ellipsometry*. Ed. by Harland G. Tompkins and Eugene A. Irene. Vol. 30. 7. Springer Berlin Heidelberg, 2005, pp. 92–4. ISBN: 978-3-540-22293-4. DOI: 10.1007/3-540-27488-X.

[54] Hisao Kikuta et al. 'Effective medium theory of two-dimensional subwavelength gratings in the non-quasi-static limit'. In: *Journal of the Optical Society of America A* 15.6 (1998), p. 1577. ISSN: 1084-7529. DOI: 10.1364/JOSAA.15.001577.

[55] Philippe Lalanne and Mike Hutley. 'The optical properties of artificial media structured at a subwavelength scale'. In: *Encyclopedia of Optical Engineering* (2003), pp. 62–71.

[56] Seungmuk Ji, Joonsik Park, and Hyuneui Lim. 'Improved antireflection properties of moth eye mimicking nanopillars on transparent glass: flat antireflection and color tuning.' In: *Nanoscale* 4.15 (2012), pp. 4603–10. ISSN: 2040-3372. DOI: 10.1039/c2nr30787a.

[57] Qiaoyin Yang et al. 'Antireflection effects at nanostructured material interfaces and the suppression of thin-film interference.' In: *Nanotechnology* 24.23 (2013), p. 235202. ISSN: 1361-6528. DOI: 10.1088/0957-4484/24/23/235202.

[58] Bruce D Macleod and Douglas S Hobbs. 'Low-cost anti-reflection technology for automobile displays'. In: *Journal of the Society for Information Display, Automotive Display Conference* (2004), pp. 1–6.

[59] Yeong Hwan Ko and Jae Su Yu. 'Design of hemi-urchin shaped ZnO nanostructures for broadband and wide-angle antireflection coatings.' In: *Optics express* 19.1 (2011), pp. 297–305. ISSN: 1094-4087.

[60] Chong Geng et al. 'Fabrication of volcano-shaped nano-patterned sapphire substrates using colloidal self-assembly and wet chemical etching.' In: *Nanotechnology* 24.33 (2013), p. 335301. ISSN: 1361-6528. DOI: 10.1088/0957-4484/24/33/335301.

[61] Chan Il Yeo et al. 'Optimal design of nano-scale surface light trapping structures for enhancing light absorption in thin film photovoltaics'. In: *Journal of Applied Physics* 114.2 (2013), p. 024305. ISSN: 00218979. DOI: 10.1063/1.4813096.

[62] Haesung Park et al. 'Broadband optical antireflection enhancement by integrating antireflective nanoislands with silicon nanoconical-frustum arrays.' In: *Advanced materials (Deerfield Beach, Fla.)* 23.48 (2011), pp. 5796–800. ISSN: 1521-4095. DOI: 10.1002/adma.201103399.

[63] Sohee Kim et al. 'Nanostructured Multifunctional Surface with Antireflective and Antimicrobial Characteristics'. In: *ACS Applied Materials & Interfaces* 7.1 (2015), pp. 326–331. ISSN: 1944-8244. DOI: 10.1021/am506254r.

[64] Jan Genzer and Kirill Efimenko. 'Creating long-lived superhydrophobic polymer surfaces through mechanically assembled monolayers.' In: *Science (New York, N.Y.)* 290.5499 (2000), pp. 2130–2133. ISSN: 00368075. DOI: 10.1126/science.290.5499.2130.

[65] K. V. Beard. 'Terminal Velocity and Shape of Cloud and Precipitation Drops'. In: *Journal of the Atmospheric Sciences* (1976), pp. 851–864.

[66] Vassilia Zorba et al. 'Biomimetic artificial surfaces quantitatively reproduce the water repellency of a lotus leaf'. In: *Advanced Materials* 20.21 (2008), pp. 4049–4054. ISSN: 09359648. DOI: 10.1002/adma.200800651.

[67] Antonio Checco, Atikur Rahman, and Charles T Black. 'Robust Superhydrophobicity in Large-Area Nanostructured Surfaces Defined by Block-Copolymer Self Assembly'. In: *Advanced Materials* 26.6 (2014), pp. 886–891. ISSN: 09359648. DOI: 10.1002/adma.201304006.

[68] E. J. Lobaton and T. R. Salamon. 'Computation of constant mean curvature surfaces: Application to the gas-liquid interface of a pressurized fluid on a superhydrophobic surface'. In: *Journal of Colloid and Interface Science* 314.1 (2007), pp. 184–198. ISSN: 00219797. DOI: 10.1016/j.jcis.2007.05.059.

[69] Wei Chen et al. 'Ultrahydrophobic and Ultralyophobic Surfaces: Some Comments and Examples'. In: *Langmuir* 15.10 (1999), pp. 3395–3399. ISSN: 0743-7463. DOI: 10.1021/la990074s.

[70] Colin R. Crick and Ivan P. Parkin. 'Superhydrophobic silica films on glass formed by hydrolysis of an acidic aerosol of tetraethylorthosilicate'. In: *Journal of Materials Chemistry* 21.25 (2011), p. 9362. ISSN: 0959-9428. DOI: 10.1039/c1jm10825e.

[71] Colin R. Crick and Ivan P. Parkin. 'Preparation and Characterisation of Super-Hydrophobic Surfaces'. In: *Chemistry - A European Journal* 16.12 (2010), pp. 3568–3588. ISSN: 09476539. DOI: 10.1002/chem.200903335.

[72] P. B. Clapham and M. C. Hutley. 'Reduction of Lens Reflexion by the "Moth Eye" Principle'. In: *Nature* 244.5414 (1973), pp. 281–282. ISSN: 0028-0836. DOI: 10.1038/244281a0.

[73] Vinod E. Sandana et al. 'Growth of "moth-eye" ZnO nanostructures on Si(111), c-Al_2O_3, ZnO and steel substrates by pulsed laser deposition'. In: *Physica Status Solidi (C)* 5 (2013), n/a–n/a. ISSN: 18626351. DOI: 10.1002/pssc.201200975.

[74] Khalid Askar et al. 'Self-assembled nanoparticle antiglare coatings'. In: *Optics Letters* 37.21 (2012), p. 4380. ISSN: 0146-9592. DOI: 10.1364/OL.37.004380.

[75] Yeeu-Chang Lee, Che-Chun Chang, and Yen-Yu Chou. 'Experimental and simulation studies of anti-reflection sub-micron conical structures on a GaAs substrate.' In: *Optics express* 21 Suppl 1.January (2013), A36–41. ISSN: 1094-4087.

[76] Fei Tao et al. 'Tuning the peak position of subwavelength silica nanosphere broadband antireflection coatings.' In: *Nanoscale research letters* 9.1 (2014), p. 361. ISSN: 1931-7573. DOI: 10.1186/1556-276X-9-361.

[77] Jane Bertone et al. 'Thickness Dependence of the Optical Properties of Ordered Silica-Air and Air-Polymer Photonic Crystals'. In: *Physical Review Letters* 83.2 (1999), pp. 300–303. ISSN: 0031-9007. DOI: 10.1103/PhysRevLett.83.300.

[78] Rajesh Rengarajan et al. 'Optical properties of a photonic crystal of hollow spherical shells'. In: *Applied Physics Letters* 77.22 (2000), p. 3517. ISSN: 00036951. DOI: 10.1063/1.1320863.

[79] Mariko Yamaki, Junichi Higo, and Kuniaki Nagayama. 'Size-Dependent Separation of Colloidal Particles In Two-Dimensional Convective Self-Assembly'. In: *Langmuir* 11.8 (1995), pp. 2975–2978. ISSN: 0743-7463. DOI: 10.1021/la00008a021.

[80] Antony S. Dimitrov and Kuniaki Nagayama. 'Continuous Convective Assembling of Fine Particles into Two-Dimensional Arrays on Solid Surfaces'. In: *Langmuir* 12.5 (1996), pp. 1303–1311. ISSN: 0743-7463. DOI: 10.1021/la9502251.

[81] Stefan Guldin et al. 'Self-Cleaning Antireflective Optical Coatings'. In: *Nano Letters* 13.11 (2013), pp. 5329–5335. ISSN: 1530-6984. DOI: 10.1021/nl402832u.

[82] Morgan Stefik et al. 'Block copolymer self-assembly for nanophotonics'. In: *Chem. Soc. Rev.* 44.15 (2015), pp. 5076–5091. ISSN: 0306-0012. DOI: 10.1039/C4CS00517A.

[83] S. Guldin and U. Steiner. 'Soft matter design principles for inorganic photonic nanoarchitectures in photovoltaics, colorimetric sensing, and self-cleaning antireflective coatings'. In: *Micro- and Nanotechnology Sensors, Systems, and Applications VI*. Ed. by Thomas George, M. Saif Islam, and Achyut K. Dutta. Vol. 9083. 2014, p. 908320. DOI: 10.1117/12.2050011.

[84] Matthew M. Hawkeye and Michael J. Brett. 'Glancing angle deposition: Fabrication, properties, and applications of micro- and nanostructured thin films'. In: *Journal of Vacuum Science & Technology A: Vacuum, Surfaces, and Films* 25.5 (2007), p. 1317. ISSN: 07342101. DOI: 10.1116/1.2764082.

[85] P Jiang et al. 'Single-Crystal Colloidal Multilayers of Controlled Thickness'. In: *Chemistry of Materials* 11.8 (1999), pp. 2132–2140. ISSN: 0897-4756. DOI: 10.1021/cm990080+.

[86] Khairudin Mohamed and Maan M. 'The Fabrication of High Aspect Ratio Nanostructures on Quartz Substrate'. In: *Updates in Advanced Lithography*. Intech, 2013. DOI: 10.5772/56315.

[87] Yunfeng Li et al. 'Biomimetic Surfaces for High-Performance Optics'. In: *Advanced Materials* 21.46 (2009), pp. 4731–4734. ISSN: 09359648. DOI: 10.1002/adma.200901335.

[88] Yunfeng Li et al. 'Bioinspired silica surfaces with near-infrared improved transmittance and superhydrophobicity by colloidal lithography.' In: *Langmuir : the ACS journal of surfaces and colloids* 26.12 (2010), pp. 9842–7. ISSN: 1520-5827. DOI: 10.1021/la100183y.

[89] Hyuneui Lim. 'Beyond a Nature-inspired Lotus Surface: Simple Fabrication Approach Part I. Superhydrophobic and Transparent Biomimetic Glass Part II. Superamphiphobic Web of Nanofibers'. In: *Advances in Biomimetics*. Ed. by Prof. Marko Cavrak. Rijeka: InTech, 2011, pp. 145–158. ISBN: 978-953-307-191-6.

[90] Hyuneui Lim et al. 'Simple nanofabrication of a superhydrophobic and transparent biomimetic surface'. In: *Chinese Science Bulletin* 54.19 (2009), pp. 3613–3616. ISSN: 1001-6538. DOI: 10.1007/s11434-009-0274-4.

[91] Xin Ye et al. 'Formation of broadband antireflective and superhydrophilic subwavelength structures on fused silica using one-step self-masking reactive ion etching'. In: *Scientific Reports* 5.April (2015), p. 13023. ISSN: 2045-2322. DOI: 10.1038/srep13023.

[92] Aikaterini Argyraki, Yiyu Ou, and Haiyan Ou. 'Broadband antireflective silicon carbide surface produced by cost-effective method'. In: *Optical Materials Express* 3.8 (2013), p. 1119. ISSN: 2159-3930. DOI: 10.1364/OME.3.001119.

[93] Tolga Aytug et al. 'Optically transparent, mechanically durable, nanostructured superhydrophobic surfaces enabled by spinodally phase-separated glass thin films.' In: *Nanotechnology* 24.31 (2013), p. 315602. ISSN: 1361-6528. DOI: 10.1088/0957-4484/24/31/315602.

[94] Yi Jia et al. 'Anti-fogging and anti-reflective silica nanofibrous film fabricated by seedless flame method'. In: *Materials Letters* 108 (2013), pp. 200–203. ISSN: 0167577X. DOI: 10.1016/j.matlet.2013.06.042.

[95] Hiroshi Toyota et al. 'Fabrication of Microcone Array for Antireflection Structured Surface Reflectivity Using Metal Dotted Pattern'. In: *The Japan Society of Applied Physics* 40.7 (2001), pp. 747–749.

[96] MicroChem Corp. *PMMA Electron-Beam resist*. Tech. rep. 2001, p. 8.

[97] Zeon Corporation. *ZEP 520A Technical Report*. Tech. rep. 2010, pp. 1–14.

[98] Dow Corning Corporation. *HSQ XR-1541 Electron-Beam resist product information*. Tech. rep. 2008, pp. 1–2.

[99] Xi Chen et al. 'Pseudo-Rhombus-Shaped Subwavelength Crossed Gratings of GaAs for Broadband Antireflection'. In: *Chinese Physics Letters* 27.12 (2010), p. 124210. ISSN: 0256-307X. DOI: 10.1088/0256-307X/27/12/124210.

[100] Yeeu-Chang Lee, Che-Chun Chang, and Yen-Yu Chou. 'Fabrication of broadband anti-reflective sub-micron structures using polystyrene sphere lithography on a Si substrate'. In: *Photonics and Nanostructures - Fundamentals and Applications* (2013). ISSN: 15694410. DOI: 10.1016/j.photonics.2013.07.007.

[101] Wei-Lun Min, Bin Jiang, and Peng Jiang. 'Bioinspired self-cleaning antireflection coatings'. In: *Advanced Materials* 20.20 (2008), pp. 3914–3918. ISSN: 09359648. DOI: 10.1002/adma.200800791.

[102] Juanyuan Hao et al. 'Langmuir-Blodgett monolayer masked chemical etching: An approach to broadband antireflective surfaces'. In: *Chemistry of Materials* 21.9 (2009), pp. 1802–1805. DOI: 10.1021/cm802758e.

[103] Andrew Shortland, Nick Rogers, and Katherine Eremin. 'Trace element discriminants between Egyptian and Mesopotamian Late Bronze Age glasses'. In: *Journal of Archaeological Science* 34.5 (2007), pp. 781–789. ISSN: 03054403. DOI: 10.1016/j.jas.2006.08.004.

[104] M.S. Walton et al. 'Evidence for the trade of Mesopotamian and Egyptian glass to Mycenaean Greece'. In: *Journal of Archaeological Science* 36.7 (2009), pp. 1496–1503. ISSN: 03054403. DOI: 10.1016/j.jas.2009.02.012.

[105] Jeanette Varberg, Bernard Gratuze, and Flemming Kaul. 'Between Egypt, Mesopotamia and Scandinavia: Late Bronze Age glass beads found in Denmark'. In: *Journal of Archaeological Science* 54 (2015), pp. 168–181. ISSN: 03054403. DOI: 10.1016/j.jas.2014.11.036.

[106] M.S. Tite, P. Manti, and A.J. Shortland. 'A technological study of ancient faience from Egypt'. In: *Journal of Archaeological Science* 34.10 (2007), pp. 1568–1583. ISSN: 03054403. DOI: 10.1016/j.jas.2006.11.010.

[107] J. P. Toner. *Popular culture in ancient Rome*. Polity Press, 2009, p. 19. ISBN: 978-0745643106.

[108] J. Bayley and J. Price. 'Glass-working in Early Medieval England'. In: *Glass in Britain and Ireland AD 350–1100*. London: British Museum Occasional, 2000, pp. 137–142. ISBN: 0861591275.

[109] M.S. Tite et al. 'The composition of the soda-rich and mixed alkali plant ashes used in the production of glass'. In: *Journal of Archaeological Science* 33.9 (2006), pp. 1284–1292. ISSN: 03054403. DOI: 10.1016/j.jas.2006.01.004.

[110] Raymond E Wetton and Harry G Moneypenny. 'Fundamental Properties of Densified Polymeric Glasses'. In: *British Polymer Journal* 7 (1975), pp. 51–68.

[111] PPG. *Gas Insulating Glass*. 2015.

[112] PPG. *TD-121: Center of Glass U-Values for Double and Triple Glazed Insulating Glass Units with Solarban 60 Low-e Glass with 100% Air, Argon, or Krypton, or Mixtures of These Gases*. 2002.

[113] PPG. *TD-101: Gas Space Convection Effects on U-values In Insulating Glass Units*. 2001.

[114] G Leftheriotis, P Yianoulis, and D Patrikios. 'Deposition and optical properties of optimised ZnS/Ag/ZnS thin films for energy saving applications'. In: *Thin Solid Films* 306.1 (1997), pp. 92–99. ISSN: 00406090. DOI: 10.1016/S0040-6090(97)00250-2.

[115] Claes G. Granqvist. 'Transparent conductors as solar energy materials: A panoramic review'. In: *Solar Energy Materials and Solar Cells* 91.17 (2007), pp. 1529–1598. ISSN: 09270248. DOI: 10.1016/j.solmat.2007.04.031.

[116] Suresh B. Sadineni, Srikanth Madala, and Robert F. Boehm. 'Passive building energy savings: A review of building envelope components'. In: *Renewable and Sustainable Energy Reviews* 15.8 (2011), pp. 3617–3631. ISSN: 13640321. DOI: 10.1016/j.rser.2011.07.014.

[117] S.M.A Durrani et al. 'Dielectric/Ag/dielectric coated energy-efficient glass windows for warm climates'. In: *Energy and Buildings* 36.9 (2004), pp. 891–898. ISSN: 03787788. DOI: 10.1016/j.enbuild.2004.02.003.

[118] F J Morin. 'Oxides Which Show a Metal-to-Insulator Transition at the Neel Temperature'. In: *Physical Review Letters* 3.1 (1959), pp. 34–36. ISSN: 0031-9007. DOI: 10.1103/PhysRevLett.3.34.

[119] Carl M. Lampert et al. 'Electrochromic materials and devices for energy efficient windows'. In: *Solar Energy Materials* 11.1-2 (1984), pp. 1–27. ISSN: 01651633. DOI: 10.1016/0165-1633(84)90024-8.

[120] K A Khan and C G Granqvist. 'Thermochromic sputter-deposited vanadium oxyfluoride coatings with low luminous absorptance'. In: *Applied Physics Letters* 55.1 (1989), p. 4. ISSN: 00036951. DOI: 10.1063/1.102388.

[121] Zheng Yang, Changhyun Ko, and Shriram Ramanathan. 'Oxide Electronics Utilizing Ultrafast Metal-Insulator Transitions'. In: *Annual Review of Materials Research* 41.1 (2011), pp. 337–367. ISSN: 1531-7331. DOI: 10.1146/annurev-matsci-062910-100347.

[122] J. B. MacChesney, J. F. Potter, and H. J. Guggenheim. 'Preparation and Properties of Vanadium Dioxide Films'. In: *Journal of The Electrochemical Society* 115.1 (1968), p. 52. ISSN: 00134651. DOI: 10.1149/1.2411002.

[123] L. A. Ryabova, I. A. Serbinov, and A. S. Darevsky. 'Preparation and Properties of Pyrolysis of Vanadium Oxide Films'. In: *Journal of The Electrochemical Society* 119.4 (1972), p. 427. ISSN: 00134651. DOI: 10.1149/1.2411002.

[124] N.R. Mlyuka, G.A. Niklasson, and C.G. Granqvist. 'Thermochromic multilayer films of VO_2 and TiO_2 with enhanced transmittance'. In: *Solar Energy Materials and Solar Cells* 93.9 (2009), pp. 1685–1687. ISSN: 09270248. DOI: 10.1016/j.solmat.2009.03.021.

[125] Volker Eyert. 'The metal-insulator transitions of VO_2: A band theoretical approach'. In: *Annalen der Physik (Leipzig)* 11.9 (2002), pp. 650–702. ISSN: 00033804. DOI: 10.1002/1521-3889(200210)11:9<650::AID-ANDP650>3.0.CO;2-K. arXiv: 0210558 [cond-mat].

[126] Yamei Li et al. 'Core-shell VO_2@TiO_2 nanorods that combine thermochromic and photocatalytic properties for application as energy-saving smart coatings'. In: *Scientific Reports* 3 (2013), p. 1370. ISSN: 2045-2322. DOI: 10.1038/srep01370.

[127] Peter Baum, Ding-Shyue Yang, and Ahmed H Zewail. '4D Visualization of Transitional Structures in Phase Transformations by Electron Diffraction'. In: *Science* 318.5851 (2007), pp. 788–792. ISSN: 1095-9203. DOI: 10.1126/science.1147724.

[128] H. Katzke, P. Tolédano, and W. Depmeier. 'Theory of morphotropic transformations in vanadium oxides'. In: *Physical Review B* 68.2 (2003), pp. 1–7. ISSN: 0163-1829. DOI: 10.1103/PhysRevB.68.024109.

[129] John B. Goodenough. 'The two components of the crystallographic transition in VO_2'. In: *Journal of Solid State Chemistry* 3.4 (1971), pp. 490–500. ISSN: 00224596. DOI: 10.1016/0022-4596(71)90091-0.

[130] M. Nazari et al. 'Temperature dependence of the optical properties of VO_2 deposited on sapphire with different orientations'. In: *Physical Review B - Condensed Matter and Materials Physics* 87.3 (2013), pp. 1–7. ISSN: 10980121. DOI: 10.1103/PhysRevB.87.035142.

[131] Alexander L. Pergament et al. 'On the Problem of Metal-Insulator Transitions in Vanadium Oxides'. In: *ISRN Condensed Matter Physics* 2013 (2013), p. 960627. ISSN: 2090-7400. DOI: 10.1155/2013/960627.

[132] A. Zylbersztejn and N.F. Mott. 'Metal-insulator transition in vanadium dioxide'. In: *Physical Review B* 11.11 (1975), pp. 4383–4395. ISSN: 0556-2805. DOI: 10.1103/PhysRevB.11.4383.

[133] Renata M. Wentzcovitch, Werner W. Schulz, and Philip B. Allen. 'VO_2: Peierls or Mott-Hubbard? A view from band theory'. In: *Physical Review Letters* 72.21 (1994), pp. 3389–3392. ISSN: 00319007. DOI: 10.1103/PhysRevLett.72.3389. arXiv: 0000135489.

[134] A. Cavalleri et al. 'Evidence for a structurally-driven insulator-to-metal transition in VO_2: A view from the ultrafast timescale'. In: *Physical Review B - Condensed Matter and Materials Physics* 70.16 (2004), pp. 1–4. ISSN: 01631829. DOI: 10.1103/PhysRevB.70.161102. arXiv: 0403214 [cond-mat].

[135] Hyun Tak Kim et al. 'Monoclinic and correlated metal phase in VO_2 as evidence of the mott transition: Coherent phonon analysis'. In: *Physical Review Letters* 97.26 (2006). ISSN: 00319007. DOI: 10.1103/PhysRevLett.97.266401. arXiv: 0608085 [cond-mat].

[136] V. Eyert. 'VO_2: A novel view from band theory'. In: *Physical Review Letters* 107.1 (2011), pp. 2–5. ISSN: 00319007. DOI: 10.1103/PhysRevLett.107.016401. arXiv: 1104.2214.

[137] F. Béteille et al. 'Switching properties of $V_{1-x}Ti_xO_2$ thin films deposited from alkoxides'. In: *Materials Research Bulletin* 32.8 (1997), pp. 1109–1117.

[138] T.E. Phillips, R.A. Murphy, and T.O. Poehler. 'Electrical studies of reactively sputtered Fe–doped VO_2 thin films'. In: *Materials Research Bulletin* 22.8 (1987), pp. 1113–1123.

[139] Troy D. Manning et al. 'APCVD of thermochromic vanadium dioxide thin films-solid solutions $V_{2-x}M_xO_2$ (M = Mo, Nb) or composites VO_2:SnO_2'. In: *Journal of Materials Chemistry* 15.42 (2005), p. 4560. ISSN: 0959-9428. DOI: 10.1039/b510552h.

[140] Chao Sun et al. 'The modulation of metal-insulator transition temperature of vanadium dioxide: a density functional theory study'. In: *J. Mater. Chem. C* 2.43 (2014), pp. 9283–9293. ISSN: 2050-7526. DOI: 10.1039/C4TC00778F.

[141] Masato Tazawa, Ping Jin, and Sakae Tanemura. 'Optical constants of $V_{1-x}W_xO_2$ films'. In: *Applied Optics* 37.10 (1998), pp. 1858–1861.

[142] Christopher S. Blackman et al. 'Atmospheric pressure chemical vapour deposition of thermochromic tungsten doped vanadium dioxide thin films for use in architectural glazing'. In: *Thin Solid Films* 517.16 (2009), pp. 4565–4570. ISSN: 00406090. DOI: 10.1016/j.tsf.2008.12.050.

[143] Manfredi Saeli et al. 'Templated growth of smart coatings: Hybrid chemical vapour deposition of vanadyl acetylacetonate with tetraoctyl ammonium bromide'. In: *Applied Surface Science* 255.16 (2009), pp. 7291–7295. ISSN: 01694332. DOI: 10.1016/j.apsusc.2009.03.083.

[144] Michael E. A. Warwick, Ian Ridley, and Russell Binions. 'The Effect of Transition Hysteresis Width in Thermochromic Glazing Systems'. In: *Open Journal of Energy Efficiency* 02.02 (2013), pp. 75–88. ISSN: 2169-2637. DOI: 10.4236/ojee.2013.22011.

[145] Ikuya Takahashi, Mitsuhiro Hibino, and Tetsuichi Kudo. 'Thermochromic Properties of Double-Doped VO_2 Thin Films Prepared by a Wet Coating Method Using Polyvanadate-Based Sols Containing W and Mo or W and Ti'. In: *Japanese Journal of Applied Physics* 40.Part 1, No. 3A (2001), pp. 1391–1395. ISSN: 0021-4922. DOI: 10.1143/JJAP.40.1391.

[146] Shi Chen et al. 'Unraveling Mechanism on Reducing Thermal Hysteresis Width of VO_2 by Ti Doping: A Joint Experimental and Theoretical Study'. In: *The Journal of Physical Chemistry C* 118.33 (2014), pp. 18938–18944. ISSN: 1932-7447. DOI: 10.1021/jp5056842.

[147] S.-Y. Li, G.A. Niklasson, and C.G. Granqvist. 'Thermochromic fenestration with VO_2-based materials: Three challenges and how they can be met'. In: *Thin Solid Films* 520.10 (2012), pp. 3823–3828. ISSN: 00406090. DOI: 10.1016/j.tsf.2011.10.053.

[148] Nuru R. Mlyuka, Gunnar A. Niklasson, and Claes G. Granqvist. 'Thermochromic VO_2–based multilayer films with enhanced luminous transmittance and solar modulation'. In: *Physica Status Solidi (a)* 206.9 (2009), pp. 2155–2160. ISSN: 18626300. DOI: 10.1002/pssa.200881798.

[149] W Burkhardt et al. 'W- and F-doped VO_2 films studied by photoelectron spectrometry'. In: *Thin Solid Films* 345.2 (1999), pp. 229–235. ISSN: 00406090. DOI: 10.1016/S0040-6090(98)01406-0.

[150] S. C. Barron et al. 'An apparatus for spatially resolved, temperature dependent reflectance measurements for identifying thermochromism in combinatorial thin film libraries'. In: *Review of Scientific Instruments* 86.11 (2015), p. 113903. ISSN: 0034-6748. DOI: 10.1063/1.4935477.

[151] Naoufal Bahlawane and Damien Lenoble. 'Vanadium oxide compounds: Structure, properties, and growth from the gas phase'. In: *Chemical Vapor Deposition* (2014), pp. 299–311. ISSN: 09481907. DOI: 10.1002/cvde.201400057.

[152] S. S. Kanu and R. Binions. 'Thin films for solar control applications'. In: *Proceedings of the Royal Society A: Mathematical, Physical and Engineering Sciences* 466.2113 (2009), pp. 19–44. ISSN: 1364-5021. DOI: 10.1098/rspa.2009.0259.

[153] Shu-Yi Li, Gunnar A. Niklasson, and Claes G. Granqvist. 'Thermochromic undoped and Mg-doped VO_2 thin films and nanoparticles: Optical properties and performance limits for energy efficient windows'. In: *Journal of Applied Physics* 115.5 (2014), p. 053513. ISSN: 0021-8979. DOI: 10.1063/1.4862930.

[154] Keisuke Shibuya and Akihito Sawa. 'Optimization of conditions for growth of vanadium dioxide thin films on silicon by pulsed-laser deposition Optimization of conditions for growth of vanadium dioxide thin films on silicon by pulsed-laser deposition'. In: 107118 (2015), pp. 0–10. ISSN: 2158-3226. DOI: 10.1063/1.4934226.

[155] M. G. Hur, T. Masaki, and D. H. Yoon. 'Thermochromic Properties of Sn, W Co-Doped VO_2 Nanostructured Thin Film Deposited by Pulsed Laser Deposition'. In: *Journal of Nanoscience and Nanotechnology* 14.12 (2014), pp. 8941–8945. ISSN: 15334880. DOI: 10.1166/jnn.2014.10054.

[156] Clara Piccirillo, Russell Binions, and Ivan P. Parkin. 'Synthesis and characterisation of W-doped VO_2 by Aerosol Assisted Chemical Vapour Deposition'. In: *Thin Solid Films* 516.8 (2008), pp. 1992–1997. ISSN: 00406090. DOI: 10.1016/j.tsf.2007.06.009.

[157] Manfredi Saeli et al. 'Templated growth of smart nanocomposite thin films: Hybrid aerosol assisted and atmospheric pressure chemical vapour deposition of vanadyl acetylacetonate, auric acid and tetraoctyl ammonium bromide'. In: *Polyhedron* 28.11 (2009), pp. 2233–2239. ISSN: 02775387. DOI: 10.1016/j.poly.2009.03.025.

[158] C. Piccirillo, R. Binions, and I. P. Parkin. 'Synthesis and functional properties of vanadium oxides: V_2O_3, VO_2, and V_2O_5 deposited on glass by aerosol-assisted CVD'. In: *Chemical Vapor Deposition* 13.4 (2007), pp. 145–151. ISSN: 09481907. DOI: 10.1002/cvde.200606540.

[159] Michael E.A. Warwick et al. 'Hybrid chemical vapour and nanoceramic aerosol assisted deposition for multifunctional nanocomposite thin films'. In: *Thin Solid Films* 519.18 (2011), pp. 5942–5948. ISSN: 00406090. DOI: 10.1016/j.tsf.2011.03.028.

[160] Pragna Kiri et al. 'Fluorine doped vanadium dioxide thin films for smart windows'. In: *Thin Solid Films* 520.4 (2011), pp. 1363–1366. ISSN: 00406090. DOI: 10.1016/j.tsf.2011.01.401.

[161] Manfredi Saeli et al. 'Nano-composite thermochromic thin films and their application in energy-efficient glazing'. In: *Solar Energy Materials and Solar Cells* 94.2 (2010), pp. 141–151. ISSN: 09270248. DOI: 10.1016/j.solmat.2009.08.010.

[162] Russell Binions et al. 'Doped and un-doped vanadium dioxide thin films prepared by atmospheric pressure chemical vapour deposition from vanadyl acetylacetonate and tungsten hexachloride: the effects of thickness and crystallographic orientation on thermochromic properties'. en. In: *Journal of Materials Chemistry* 17.44 (2007), p. 4652. ISSN: 0959-9428. DOI: 10.1039/b708856f.

[163] Russell Binions, Clara Piccirillo, and Ivan P. Parkin. 'Tungsten doped vanadium dioxide thin films prepared by atmospheric pressure chemical vapour deposition from vanadyl acetylacetonate and tungsten hexachloride'. In: *Surface and Coatings Technology* 201.22-23 (2007), pp. 9369–9372. ISSN: 02578972. DOI: 10.1016/j.surfcoat.2007.03.026.

[164] Troy D. Manning and Ivan P. Parkin. 'Vanadium(IV) oxide thin films on glass and silicon from the atmospheric pressure chemical vapour deposition reaction of $VOCl_3$ and water'. In: *Polyhedron* 23.18 (2004), pp. 3087–3095. ISSN: 02775387. DOI: 10.1016/j.poly.2004.09.020.

[165] Troy D. Manning et al. 'Intelligent window coatings: atmospheric pressure chemical vapour deposition of vanadium oxides'. In: *Journal of Materials Chemistry* 12.10 (2002), pp. 2936–2939. ISSN: 09599428. DOI: 10.1039/b205427m.

[166] Michael J. Powell et al. 'Intelligent Multifunctional VO_2/SiO_2/TiO_2 Coatings for Self-Cleaning, Energy-Saving Window Panels'. In: *Chemistry of Materials* 28.5 (2016), pp. 1369–1376. ISSN: 0897-4756. DOI: 10.1021/acs.chemmater.5b04419.

[167] Kai Zhang et al. 'VO_2 Films Prepared by Atomic Layer Deposition and RF Magnetron Sputtering'. In: *224th Electrochemical Society Meeting*. Vol. 7041. 2013, p. 162902.

[168] Timothee Blanquart et al. 'Atomic layer deposition and characterization of vanadium oxide thin films'. In: *RSC Advances* 3.4 (2013), p. 1179. ISSN: 2046-2069. DOI: 10.1039/c2ra22820c.

[169] Geert Rampelberg et al. 'Semiconductor-metal transition in thin VO_2 films grown by ozone based atomic layer deposition'. In: *Applied Physics Letters* 98.16 (2011), pp. 38–41. ISSN: 00036951. DOI: 10.1063/1.3579195.

[170] Shu-Yi Li et al. 'Thermochromic VO_2 nanorods made by sputter deposition: Growth conditions and optical modeling'. In: *Journal of Applied Physics* 114.3 (2013), p. 033516. ISSN: 00218979. DOI: 10.1063/1.4813876.

[171] G. P. Nagabhushana and G.T. Chandrappa. 'Facile solution combustion synthesis of monoclinic VO_2: A unique and versatile approach'. In: *Journal of Materials Chemistry A* 1.207890 (2013). DOI: 10.1039/C3TA11692A.

[172] Shaotang Li et al. 'Preparation and Characterization of Self-Supporting Thermochromic Films Composed of VO_2(M)@SiO_2 Nanofibers'. In: *ACS Appl. Mater. Interfaces* 5 (2013), pp. 6453–6457. DOI: 10.1021/am401839d.

[173] Jared Crane et al. 'The Application of Electric Fields to Aerosol Assisted Chemical Vapor Deposition Reactions'. en. In: *Journal of The Electrochemical Society* 158.2 (2011), p. D62. ISSN: 00134651. DOI: 10.1149/1.3519870.

[174] Ru Chen et al. 'Shape-controlled synthesis and influence of W doping and oxygen nonstoichiometry on the phase transition of VO_2'. In: *Scientific Reports* 5.August (2015), p. 14087. ISSN: 2045-2322. DOI: 10.1038/srep14087.

[175] Michael E.a. Warwick, Ian Ridley, and Russell Binions. 'Thermochromic vanadium dioxide thin films from electric field assisted aerosol assisted chemical vapour deposition'. In: *Surface and Coatings Technology* 230 (2013), pp. 163–167. ISSN: 02578972. DOI: 10.1016/j.surfcoat.2013.06.077.

[176] B. Viswanath et al. 'Geometric confinement effects on the metal-insulator transition temperature and stress relaxation in VO_2 thin films grown on silicon'. In: *Journal of Applied Physics* 109.6 (2011), p. 063512. ISSN: 00218979. DOI: 10.1063/1.3556756.

[177] J. Narayan and V. M. Bhosle. 'Phase transition and critical issues in structure-property correlations of vanadium oxide'. In: *Journal of Applied Physics* 100.10 (2006), p. 103524. ISSN: 00218979. DOI: 10.1063/1.2384798.

[178] M. Nazari et al. 'Finite size effect on the phase transition of vanadium dioxide'. In: *Applied Physics Letters* 103.4 (2013), p. 043108. ISSN: 00036951. DOI: 10.1063/1.4816507.

[179] E. Radue et al. 'Effect of a substrate-induced microstructure on the optical properties of the insulator-metal transition temperature in VO_2 thin films'. In: *Journal of Applied Physics* 113.23 (2013), p. 233104. ISSN: 00218979. DOI: 10.1063/1.4811689.

[180] R. A. Aliev et al. 'Effect of grain sizes on the metal-semiconductor phase transition in vanadium dioxide polycrystalline thin films'. In: *Physics of the Solid State* 48.5 (2006), pp. 929–934. ISSN: 1063-7834. DOI: 10.1134/S1063783406050180.

[181] Eduardo a. Coronado and George C. Schatz. 'Surface plasmon broadening for arbitrary shape nanoparticles: A geometrical probability approach'. In: *The Journal of Chemical Physics* 119.7 (2003), p. 3926. ISSN: 00219606. DOI: 10.1063/1.1587686.

[182] S. M. Babulanam et al. 'Thermochromic VO_2 films for energy-efficient windows'. In: *Solar Energy Materials* 16 (1987), pp. 347–363.

[183] Philip B. Allen et al. 'Resistivity of the high-temperature metallic phase of VO_2'. In: *Physical Review B* 48.7 (1993), pp. 4359–4363. ISSN: 01631829. DOI: 10.1103/PhysRevB.48.4359.

[184] Jan Tomczak and Silke Biermann. 'Optical properties of correlated materials: Generalized Peierls approach and its application to VO_2'. In: *Physical Review B* 80.8 (2009), pp. 1–13. ISSN: 1098-0121. DOI: 10.1103/PhysRevB.80.085117.

[185] Jianwei Ma et al. 'Thickness-Dependent Structural and Optical Properties of VO_2 Thin Films'. In: *Japanese Journal of Applied Physics* 50.2 (2011), p. 020215. ISSN: 0021-4922. DOI: 10.1143/JJAP.50.020215.

[186] Gang Xu et al. 'Thickness dependence of optical properties of VO_2 thin films epitaxially grown on sapphire (0001)'. In: *Applied Surface Science* 244.1-4 (2005), pp. 449–452. ISSN: 01694332. DOI: 10.1016/j.apsusc.2004.09.157.

[187] ISO. 'ISO 9050âĂŤdetermination of light transmittance, solar direct transmittance, total solar energy transmittance, ultraviolet transmittance and related glazing factors'. In: *International Standard Organization* (2005).

[188] European Standards in English. *EN410 - Glass in building. Determination of luminous and solar characteristics of glazing.* 1998.

[189] Ivan P. Parkin et al. 'Thermochromic coatings for intelligent architectural glazing'. In: *Journal of Nano Research* 2 (2008), pp. 1–20. ISSN: 1662-5250.

[190] M. Tazawa et al. 'Design, formation and characterization of a novel multifunctional window with VO_2 and TiO_2 coatings'. In: *Applied Physics A: Materials Science & Processing* 77.3-4 (2003), pp. 455–459. ISSN: 0947-8396. DOI: 10.1007/s00339-002-1460-2.

[191] Gang Xu et al. 'Optimization of antireflection coating for VO_2-based energy efficient window'. In: *Solar Energy Materials and Solar Cells* 83.1 (2004), pp. 29–37. ISSN: 09270248. DOI: 10.1016/j.solmat.2004.02.014.

[192] Zongtao Zhang et al. 'Solution-based fabrication of vanadium dioxide on F:SnO_2 substrates with largely enhanced thermochromism and low-emissivity for energy-saving applications'. In: *Energy & Environmental Science* 4.10 (2011), p. 4290. ISSN: 1754-5692. DOI: 10.1039/c1ee02092g.

[193] T Smith and J Guild. 'The C.I.E. colorimetric standards and their use'. In: *Transactions of the Optical Society* 22.3 (1931), p. 73.

[194] PPG. *TD-122: Surface Orientation of Low Light Transmittance Glasses*. 2011.

[195] Jan M. Tomczak and Silke Biermann. 'Optical properties of correlated materials - Or why intelligent windows may look dirty'. In: *Physica Status Solidi (B)* 246.9 (2009), pp. 1996–2005. ISSN: 03701972. DOI: 10.1002/pssb.200945231.

[196] Noboru Ohta and Alan R. Robertson. *CIE standard colorimetric system in colorimetry: fundamentals and applications*. Chichester, UK: John Wiley & Sons, Ltd, 2006, pp. 92–96. ISBN: 9780470094747. DOI: 10.1002/0470094745.ch3.

[197] American Society for Testing and Materials. 'ASTM G173-03 reference spectra'. In: *Annual Book of ASTM Standards* (2013). DOI: 10.1520/G0173-03R12.

[198] Manfredi Saeli et al. 'Energy modelling studies of thermochromic glazing'. In: *Energy and Buildings* 42.10 (2010), pp. 1666–1673. ISSN: 03787788. DOI: 10.1016/j.enbuild.2010.04.010.

[199] Michael Warwick, Ian Ridley, and Russell Binions. 'Variation of Thermochromic Glazing Systems Transition Temperature, Hysteresis Gradient and Width Effect on Energy Efficiency'. In: *Buildings* 6.2 (2016), p. 22. ISSN: 2075-5309. DOI: 10.3390/buildings6020022.

[200] PPG. *PPG Monolithic Glass Comparisons*. 2015.

[201] European Comittiee for Standardisation. *Glass in buildings: determination of thermaltransmittance (U-value, calculation method)*. Tech. rep. European Comittiee for Standardisation, 1997.

[202] NSG Group. *Technical Bulletin: Glass and Energy*. Tech. rep. Nippon Sheet Glass Inc., 2013, pp. 1–4.

[203] PPG. *TD-148: Reducing Fading and Material Degradation of Interior Furnishings Caused by Solar Radiation Exposure*. 2009.

[204] A F McKinlay and B L Diffey. 'A reference spectrum for ultraviolet-induced erythema in human skin.' In: *Human Exposure to Ultraviolet Radiation: Risks and Regulations*. 1987, pp. 83–87.

[205] R B Setlow. 'The wavelengths in sunlight effective in producing skin cancer: a theoretical analysis.' In: *Proceedings of the National Academy of Sciences of the United States of America* 71.9 (1974), pp. 3363–3366. ISSN: 0027-8424. DOI: 10.1073/pnas.71.9.3363.

[206] R B Setlow. 'The wavelengths in sunlight effective in producing skin cancer: a theoretical analysis.' In: *Proceedings of the National Academy of Sciences of the United States of America* 71.9 (1974), pp. 3363–6. ISSN: 0027-8424.

[207] UK government. *Tinted vehicle windows: the law*. 2016.

[208] David L. C. Chan, Marin Soljačić, and J. D. Joannopoulos. 'Thermal emission and design in 2D-periodic metallic photonic crystal slabs'. In: *Optics Express* 14.19 (2006), p. 8785. ISSN: 1094-4087. DOI: 10.1364/OE.14.008785.

[209] Hans W. Verleur, A. S. Barker Jr., and C. N. Berglund. 'Optical Properties of VO_2 between 0.25 and 5eV'. In: *Physical Review* 58.3 (1968), p. 1356. ISSN: 0030-3941. DOI: 10.1364/JOSA.58.001356.

[210] Aaswath P. Raman et al. 'Passive radiative cooling below ambient air temperature under direct sunlight'. In: *Nature* 515.7528 (2014), pp. 540–544. ISSN: 0028-0836. DOI: 10.1038/nature13883.

[211] Michael E.a. Warwick, Ian Ridley, and Russell Binions. 'The effect of transition gradient in thermochromic glazing systems'. In: *Energy and Buildings* 77 (2014), pp. 80–90. ISSN: 03787788. DOI: 10.1016/j.enbuild.2014.03.044.

[212] Sabine Hoffmann, Eleanor S. Lee, and César Clavero. 'Examination of the technical potential of near-infrared switching thermochromic windows for commercial building applications'. In: *Solar Energy Materials and Solar Cells* 123 (2014), pp. 65–80. ISSN: 09270248. DOI: 10.1016/j.solmat.2013.12.017.

[213] Luís L Fernandes et al. 'Angular selective window systems : Assessment of technical potential for energy savings'. In: *Energy and Buildings* 90.October (2015), pp. 188–206.

[214] E S Lee et al. 'Assessment of the potential to achieve very low energy use in public buildings in China with advanced window and shading systems'. In: *Buildings* 5.2 (2015), pp. 668–699.

[215] Hong Ye, Xianchun Meng, and Bin Xu. 'Theoretical discussions of perfect window, ideal near infrared solar spectrum regulating window and current thermochromic window'. In: *Energy and Buildings* 49 (2012), pp. 164–172. DOI: 10.1016/j.enbuild.2012.02.011.

[216] Hong Ye et al. 'The energy saving index and the performance evaluation of thermochromic windows in passive buildings'. In: *Renewable Energy* 66 (2014), pp. 215–221. ISSN: 09601481. DOI: 10.1016/j.renene.2013.12.008.

[217] Manfredi Saeli et al. 'Optimisation of Thermochromic Thin Films on Glass; Design of Intelligent Windows'. In: *Advances in Science and Technology* 75 (2010), pp. 79–90. ISSN: 1662-0356. DOI: 10.4028/www.scientific.net/AST.75.79.

[218] M Saeli et al. 'Thermochromic Thin Films: Synthesis, Properties and Energy Consumption Modelling'. In: *Materials and processes for energy: communicating current research and technological developments*. Ed. by A. Méndez-Vilas. Formatex, 2013, pp. 736–746.

[219] Hong Ye et al. 'The demonstration and simulation of the application performance of the vanadium dioxide single glazing'. In: *Solar Energy Materials and Solar Cells* 117 (2013), pp. 168–173. ISSN: 09270248. DOI: 10.1016/j.solmat.2013.05.061.

[220] X.J Wang et al. 'XRD and Raman study of vanadium oxide thin films deposited on fused silica substrates by RF magnetron sputtering'. In: *Applied Surface Science* 177.1-2 (2001), pp. 8–14. ISSN: 01694332. DOI: 10.1016/S0169-4332(00)00918-1.

[221] Troy D Manning et al. 'Intelligent Window Coatings : Atmospheric Pressure Chemical Vapor Deposition of Tungsten-Doped Vanadium Dioxide'. In: *Chem. Mater* 16.4 (2004), pp. 744–749.

[222] Davide Barreca. 'Vanadyl Precursors Used to Modify the Properties of Vanadium Oxide Thin Films Obtained by Chemical Vapor Deposition'. In: *Journal of The Electrochemical Society* 146.2 (1999), p. 551. ISSN: 00134651. DOI: 10.1149/1.1391642.

[223] P. Schilbe and D. Maurer. 'Lattice dynamics in VO_2 near the metal-insulator transition'. In: *Materials Science and Engineering: A* 370.1-2 (2004), pp. 449–452. ISSN: 09215093. DOI: 10.1016/j.msea.2003.08.114.

[224] Peter Schilbe. 'Raman scattering in VO_2'. In: *Physica B: Condensed Matter* 316-317 (2002), pp. 600–602. ISSN: 09214526. DOI: 10.1016/S0921-4526(02)00584-7.

[225] Mei Pan et al. 'Raman study of the phase transition in VO_2 thin films'. In: *Journal of Crystal Growth* 268.1-2 (2004), pp. 178–183. ISSN: 00220248. DOI: 10.1016/j.jcrysgro.2004.05.005.

[226] H Kakiuchida et al. 'Optical properties of vanadium dioxide film during semiconductive-metallic phase transition'. In: *Japanese Journal of Applied Physics Part 2-Letters & Express Letters* 46.4-7 (2007), pp. L113–L116. ISSN: 0021-4922. DOI: 10.1143/jjap.46.l113.

[227] Chang Liu et al. 'Vanadium dioxide nanogrid films for high transparency smart architectural window applications'. In: *Optics Express* 23.3 (2015), A124. ISSN: 1094-4087. DOI: 10.1364/OE.23.00A124.

[228] Cheikhou O.F. Ba et al. 'VO_2 thin films based active and passive thermochromic devices for energy management applications'. In: *Current Applied Physics* 14.11 (2014), pp. 1531–1537. ISSN: 15671739. DOI: 10.1016/j.cap.2014.09.005.

[229] Axel Donges. 'The coherence length of black-body radiation'. In: *European Journal of Physics* 19.3 (1999), pp. 245–249. ISSN: 0143-0807. DOI: 10.1088/0143-0807/19/3/006.

[230] Edward D. Palik. *Handbook of Optical Constants of Solids*. Academic Press, 1997. ISBN: 978-0-12-544415-6.

[231] D. R. S. Cumming et al. 'Fabrication of 3 nm wires using 100 keV electron beam lithography and poly(methyl methacrylate) resist'. In: *Applied Physics Letters* 68.3 (1996), p. 322. ISSN: 00036951. DOI: 10.1063/1.116073.

[232] Seung-Man Yang et al. 'Nanomachining by colloidal lithography.' In: *Small (Weinheim an der Bergstrasse, Germany)* 2.4 (2006), pp. 458–75. ISSN: 1613-6829. DOI: 10.1002/smll.200500390.

[233] Giuseppe Boniello et al. 'Brownian diffusion of a partially wetted colloid'. In: *Nature Materials* 14.September (2015). ISSN: 1476-1122. DOI: 10.1038/nmat4348.

[234] S. Pinto et al. 'ClimaWin: An intelligent window for optimal ventilation and minimum thermal loss'. In: *2013 IEEE International Symposium on Industrial Electronics* (2013), pp. 1–6. DOI: 10.1109/ISIE.2013.6563790.

[235] Seung Goo Lee et al. 'Switchable transparency and wetting of elastomeric smart windows.' In: *Advanced materials (Deerfield Beach, Fla.)* 22.44 (2010), pp. 5013–7. ISSN: 1521-4095. DOI: 10.1002/adma.201002320.

[236] C. Bechinger and B.A. Gregg. 'Development of a new self-powered electrochromic device for light modulation without external power supply'. In: *Solar Energy Materials and Solar Cells* 54.1-4 (1998), pp. 405–410. ISSN: 09270248. DOI: 10.1016/S0927-0248(98)00092-0.

[237] K. Satyen et al. 'Stand-alone photovoltaic-powered electrochromic smart window'. In: *Electrochimica Acta* 46.13-14 (2001), pp. 2125–2130.

[238] Fraçois Pichot et al. 'Flexible Solid-State Photoelectrochromic Windows'. In: *Journal of The Electrochemical Society* 146.11 (1999), pp. 4324–4326.

[239] C.G. Granqvist. *Handbook of inorganic electorchromic materials*. Elsevier Science Ltd, 1995.

[240] S Papaefthimiou, G Leftheriotis, and P Yianoulis. 'Advanced electrochromic devices based on WO_3 thin films'. In: *Electrochimica Acta* 46.13-14 (2001), pp. 2145–2150. ISSN: 00134686. DOI: 10.1016/S0013-4686(01)00393-0.

[241] E Syrrakou, S Papaefthimiou, and P Yianoulis. 'Eco-efficiency evaluation of a smart window prototype.' In: *The Science of the total environment* 359.1-3 (2006), pp. 267–82. ISSN: 0048-9697. DOI: 10.1016/j.scitotenv.2005.10.023.

[242] E.S. Lee and D.L. DiBartolomeo. 'Application issues for large-area electrochromic windows in commercial buildings'. In: *Solar Energy Materials and Solar Cells* 71.4 (2002), pp. 465–491.

[243] Gunnar A. Niklasson and Claes G. Granqvist. 'Electrochromics for smart windows: thin films of tungsten oxide and nickel oxide, and devices based on these'. en. In: *Journal of Materials Chemistry* 17.2 (2007), p. 127. ISSN: 0959-9428. DOI: 10.1039/b612174h.

[244] Andreas Georg et al. 'Switchable glazing with a large dynamic range in total solar energy transmittance (TSET)'. In: *Solar Energy* 62.3 (1998), pp. 215–228. ISSN: 0038092X. DOI: 10.1016/S0038-092X(98)00014-0.

[245] J W Doane, G Chidichimo, and N A P Vaz. *Light modulating material comprising a liquid crystal dispersion in a plastic matrix*. 1992.

[246] Michael G. Debije. 'Solar Energy Collectors with Tunable Transmission'. In: *Advanced Functional Materials* 20.9 (2010), pp. 1498–1502. ISSN: 1616301X. DOI: 10.1002/adfm.200902403.

[247] C.G. Granqvist et al. 'Progress in chromogenics: New results for electrochromic and thermochromic materials and devices'. In: *Solar Energy Materials and Solar Cells* 93.12 (2009), pp. 2032–2039. ISSN: 09270248. DOI: 10.1016/j.solmat.2009.02.026.

[248] S. S. Kanu and R. Binions. 'Thin films for solar control applications'. In: *Proceedings of the Royal Society A: Mathematical, Physical and Engineering Sciences* 466.2113 (2009), pp. 19–44. ISSN: 1364-5021. DOI: 10.1098/rspa.2009.0259.

[249] Haruo Watanabe. 'Intelligent window using a hydrogel layer for energy efficiency'. In: *Solar Energy Materials and Solar Cells* 54.1-4 (1998), pp. 203–211. ISSN: 09270248. DOI: 10.1016/S0927-0248(98)00072-5.